Hybrid Perovskites :
Colloidal Precursors to Thin Films

Hybrid Perowskite :
Von Kolloidalen Precursoren zu dünnen Schichten

Dissertation

Shambhavi Pratap

2021

Technische Universität München
Physik-Department
Lehrstuhl für Funktionelle Materialien

TECHNISCHE UNIVERSITÄT MÜNCHEN

Physik-Department
Lehrstuhl für Funktionelle Materialien

Hybrid Perovskites : Colloidal Precursors to Thin Films

Shambhavi Pratap, M. Sc.

Vollständiger Abdruck der von der Fakultät für Physik der Technischen Universität München zur Erlangung des akademischen Grades eines

Doktors der Naturwissenschaften (Dr. rer. nat.)

genehmigten Dissertation.

Vorsitzender: Prof. Dr. David Egger
Prüfer der Dissertation: 1. Prof. Dr. Peter Müller-Buschbaum
2. Prof. Dr. Aliaksandr Bandarenka

Die Dissertation wurde am 28.06.2021 bei der Technischen Universität München eingereicht und durch die Fakultät für Physik am 21.07.2021 angenommen.

Abstract

The structural and optoelectronic properties of mixed halide perovskite colloidal precursor dispersions are investigated. The concentration behavior of the precursor presents different regimes of growing structures, which affect the thin film morphology. Originating from stochastic nanocrystalline colloidal precursors with differential chemical compositions, crystalline thin films exhibit hierarchical structures originating at the crystallographic level and scaling up to mesoscale structures. These structures are manifested scaling within their nanocrystalline morphology and mesoscale topology. Morphogenetic signatures within thin films are interlinked to differential precursor chemistry to explain the cooperative impact of structure-defining inorganic and organic counterparts on perovskite hybrids. The processing of perovskite thin films from colloidal precursors includes complex phenomena, which affect their processing-structure-function relationships. Thin films of methylammonium lead iodide are processed by spin coating, antisolvent drop, and annealing of colloidal precursors. The structure and properties of transient and stable phases formed during the process are reported, and the mechanistic insights of the underlying transitions are revealed by combining in situ data from grazing-incidence wide-angle X-ray scattering and photoluminescence spectroscopy. Multimodal data signatures of key processes of nucleation and dissolution-recrystallization are investigated. Understanding the effect of chemical species on the structural characteristics of thin films and leveraging complex assembly processes present facile routes to tuning multiscale morphologies in thin films, pertinent for engineering functional performance metrics within thin film perovskite photovoltaics.

Zusammenfassung

Die strukturellen und optoelektronischen Eigenschaften von gemischten Halogenidperowskit-Kolloid-Precursor-Dispersionen werden untersucht. Das konzentrationsabhängige Verhalten des Precursors weist unterschiedliche Wachstumsregime auf, die die Filmmorphologie beeinflussen. Ausgehend von stochastischen nanokristallinen kolloidalen Vorläufern mit unterschiedlichen chemischen Zusammensetzungen weisen kristalline dünne Filme hierarchische Strukturen auf, die auf der kristallographischen Ebene entstehen und bis zu mesoskaligen Strukturen skalieren, die sich in ihrer nanokristallinen Morphologie und mesoskaligen Topologie manifestieren. Die morphogenetische Signaturen in dünnen Filmen werden mit unterschiedlicher Vorstufenchemie verknüpft und erklären den kooperativen Einfluss struktur definierender anorganischer und deren organischer Gegenstücke auf Perowskit-Hybride. Die Verarbeitung von Perowskit-Filmen aus kolloidalen Vorläufern umfasst komplexe Phänomene, die Auswirkungen auf die jeweiligen Verarbeitungs-Struktur-Funktions-Beziehungen haben. Dünne Filme aus Methylammonium-Bleijodid werden durch Schleuderbeschichtung, Anti-Lösungsmittel-Tropfen und Tempern von kolloidalen Vorläufern verarbeitet. Die Struktur und Eigenschaften der während des Prozesses gebildeten transienten und stabilen Phasen werden beschrieben, und die mechanistischen Erkenntnisse der zugrunde liegenden Übergänge werden durch die Kombination von In-situ-Daten aus Weitwinkel-Röntgenstreuung unter streifendem Einfall und Photolumineszenzspektroskopie gewonnen. Multimodale Datensignaturen von Schlüsselprozessen der Nukleation und Auflösungs-Rekristallisation werden untersucht. Das Verständnis der Wirkung chemischer Spezies auf die strukturellen Eigenschaften von dünnen Filmen und die Nutzung komplexer Montageprozesse bieten einfache Wege zur Abstimmung von Multiskalenmorphologien in dünnen Filmen, die für die Entwicklung funktionaler Leistungsmetriken in der Film-Perowskit-Photovoltaik relevant sind.

Contents

List of abbreviations

δ	optical pathway
ϵ	extinction coefficient
ν	wavenumber
CB	chlorobenzene
DLS	dynamic light scattering
DMF	N,N-dimethylformamide
DMSO	dimethyl sulfoxide
DWBA	distorted wave born approximation
FF	form factor
GFS	gasflow system
GIWAXS	grazing-incidence wide angle x-ray scattering
IUPAC	International Union of Pure and Applied Chemistry
$MAPbBr_3$	methylammonium lead bromide
$MAPbI_3$ / MAPI	methylammounium lead iodide
PL	photoluminescence
RH	relative humidity
rpm	revolutions per minute
SC	spin-coating

SDD	sample detector distance
SEM	scanning electron microscopy
SF	structure factor
UV	ultra-violet light
UV-vis	ultraviolet and visible light
vis	visible
XRD	x-ray diffraction

List of Figures

1 Introduction

As the world's population increases alongside the per-capita consumption [1], the need for smarter and versatile energy materials is on the rise. In 2016, Earth permanently crossed the CO_2 threshold of 400 ppm. This alone speaks volumes about the global pollution trends since the Industrial revolution that have caused an increase in the global temperatures by 1.8°C. Not the falling rations of coal, oil and natural gas but such alarming benchmarks reached by mankind reaffirm the necessity of the world to shift their ever growing energy demands to cleaner technologies. For rapidly developing economies like India, which serves as a home to 18% of the world's population, energy needs have almost doubled since the past decade. The obviously growing trend of energy demands require the world to shift to cleaner sources of energy. Solar energy is widely acknowledged as the most abundant source of energy available to mankind. Harnessing the energy from the sun is an attractive challenge, which was made a reality by the discovery of the photovoltaic effect in 1839, even though back then, perhaps only few grasped the significance of the astounding discovery. The first practical solar cell was fabricated out of silicon in 1954, which had a nascent efficiency of 4%. Since then, solar cells have expressed a steep growth curve [2].

Hybrid lead halide perovskite materials have been known to the scientific community for a long time [3, 4] and have since been extensively studied for several properties, [5–9]. However they were first utilized for photovoltaic applications in 2009 [10]. The first reported photoconversion efficiency for perovskite sensitized solar cells were 3.8% in 2009. Ever since the discovery of the possibility of using perovskites as active layer components in solar cells, efficiencies have crossed the 20% [11] benchmark, competitive with existing single-crystal silicon photovoltaic technologies, which needed decades to reach its efficiencies. A comparison of the progress of various photovoltaic technologies is given in Figure 1.1 [2]. Perovskite based materials technology utilizes cheap precursors and employs low temperature processing for production of solar cells. It capitalizes on the process-

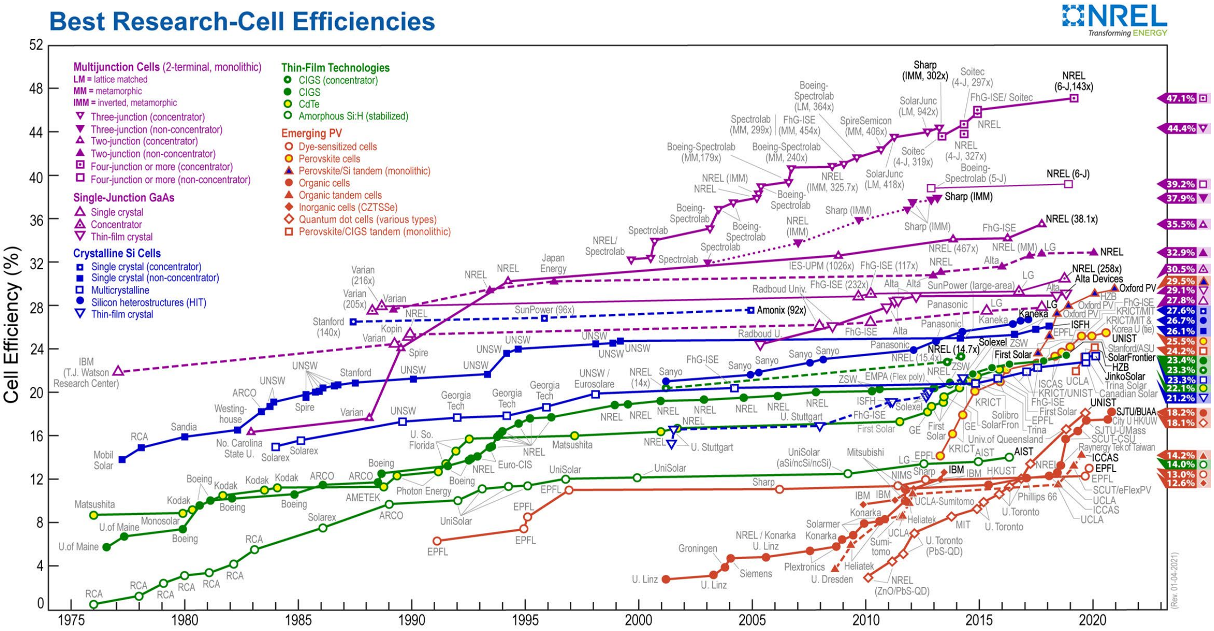

Figure 1.1: Progress of photovoltaic technologies over time. Perovskite materials fall under "Emerging PV" and showcase a steep technological growth curve. Image taken from reference [2].

ing benefits of dye sensitized solar cells while combining the efficiencies of silicon based technologies. Deviating from the high energetic needs of silicon that requires clean-room environments and high temperatures for fabrication and purification, perovskites fall under the category of thin film solar cells, which can be scaled for large scale production by inexpensive techniques such as roll-to-roll processing and printing [12]. These materials still represent a nascent technology which have achieved significant performance, in spite of being underexplored. The ease of tuning their optoelectronic properties through facile materials engineering has further led to an explosion in the research activity in material management [13–16]. Proper investigation of the material characteristics would help to exploit the properties in a better manner to produce more reliable sources of energy.

Halide perovskites are formed out of colloidal precursors with myriad interactions between them. They lead to the manifestation of multiscale morphologies when fabricated into thin films [17]. This leads to the well known issue of lack of reproducibility within formed thin films and necessitates the investigation of the materials in all their forms of existence, starting from complex fluid precursors, and ranging to thin films. The emergence of microstructure has important implications for applications of thin films in photovoltaic and optoelectronics and an investigation into the intrinsic tendencies of microstructural evolution is needed.

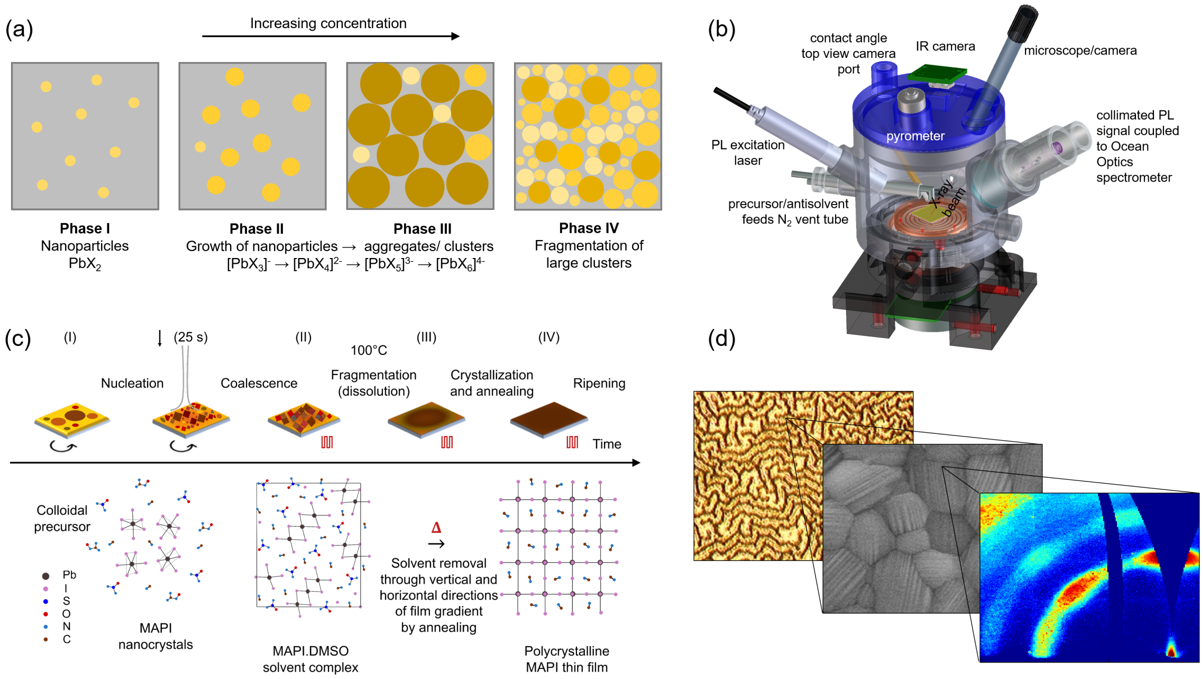

Figure 1.2: Overview of research topics covered in the present thesis. (a) Evolution of entities in hybrid perovskite precursors with changing concentration that impact resultant thin film morphologies. Reproduced from [18] with permission from The Royal Society of Chemistry. (b) Multimodal analytical cell utilized for the in situ processing of precursors into thin films by spin coating and annealing with simultaneous diffraction, photoluminescence and IR pyrometry measurements at a synchrotron source. Reproduced from [19] with permission. Copyright 2019, IUCr Journals. (c) Molecular insights into nucleation and growth processes occuring during the fabrication of perovskite thin films evidenced by in situ measurements. (d) Hierarchical microstructures in spin coated thin films and the implications for photovoltaics. Reproduced from [20] with permission from American Chemical Society.

In this thesis, we explore the interactions present between fluid precursors, and thin films formulated from them. The aim is to understand the morphological, structural and optical characteristics of the material in fluid precursor form and when formed into thin films. This will help improve the quality of thin films and devices formed from them and help increase photovoltaic efficiencies and reduce cost of production. The focus lies on establishing an understanding of the complex nature of the material properties, which are dynamic and strongly affected by changes in chemical concentration, composition, in addition to changes in physical surroundings. To this effect, colloidal precursors are explored in their various structural phases and their evolution from fluids to thin films is investigated in situ as depicted in Figure 1.2.

The thesis is organized as follows. Subsequent to this introductory chapter, a necessary theoretical introduction to concepts key to this thesis is given in Chapter 2. Owing to the presence of polydisperse particles in precursors utilized for preparation of thin films, morphological heterogeneities are found emergent, in the form of topological microstructure and crystalline orientation, which are investigated with the aid of microscopy and x-ray scattering based techniques. Materials and methods of sample preparation and characterization are explained in Chapter 3. The instrument design of a multimodal analytical cell to study the in situ conversion of colloidal precursors to thin films is documented in Section 3.3. The aim of Chapter 4 is to introduce the optoelectronic properties of well known perovskites $CH_3NH_3PbI_3$, $CH_3NH_3PbBr_3$, and their mixture $CH_3NH_3PbI_{1.50}Br_{1.50}$ to decohere the range of forces acting between them at different concentrations. The investigation includes data from the publication ”Emergence of lead halide perovskite colloidal dispersions through aggregation and fragmentation: insights from the nanoscale to the mesoscale” [18]. Chapter 5 focuses on the exploration of solid solutions of mixed halide and mixed perovskite based systems in thin films and explores the physicochemical origins of hierarchical structures and their implications for photovoltaic applications. The chapter includes data from the publication ”Hierarchical Structures from Nanocrystalline Colloidal Precursors within Hybrid Perovskite Thin Films : Implications for Photovoltaics” [20] To understand the conversion of the complex colloidal precursors to thin films, in situ studies are employed with the aid of an analytical cell to understand the phenomenological origin of factors leading to irreproducibility in thin films. Chapter 6 explores the in situ processes occurring during spin coating and crystallization of hybrid perovskites. By combining data from complementary structural and optical methodologies, molecular insights of complex phenomenon such as nucleation and dissolution-recrystallization are presented. The chapter includes data from the publication ”Out-of-equilibrium processes in crystallization of organic-inorganic perovskites during spin coating”.

Chapter 7 summarizes the results from the chapters and gives an overarching perspective on the conclusions of this work.

2 Theoretical background

2.1 Hybrid Perovskites

Hybrid perovskites are a class of materials discovered in the Russian Ural Mountains by Gustav Rose, and are named after the mineralogist Lev A. Perovski. Hybrid perovskites referred to in this thesis are of the form ABX_3 where A is an organic cation like methylammonium $CH_3NH_3{}^+$ (MA^+) or formamidinium $CH(NH_2)_2{}^+$ (FA^+), B is a metal ion like Pb^{2+} and X is a halide ion like I^-, Br^-. These materials were first synthesized by Dieter Weber [3]. Their attractive and tunable optoelectronic properties stem from their crystalline nature and the ability to be formed out of solution based precursors, [21] instigating intensive research efforts on the material [22, 23]. In 2009, the applicability of the material in photovoltaic applications was discovered, replacing the unstable dyes utilized in dye-sensitized solar cells [10]. The initially low photovoltaic efficiencies of devices and poor stability of the materials were improved to long term stable and high efficiency devices in 2021 [11]. In this section, a theoretical background of hybrid perovskites is discussed, laying emphasis on the material structural, morphological and optoelectronic properties.

2.1.1 Structural characteristics

The ABX_3 crystal structure is found in many materials, whose structure was first described by Victor Goldschmidt. The structure combines cationic species A and B commonly bonded to an anionic species X, with all ions bearing different sizes. From a crystallographic stand point, an ideal cubic perovskite structure has the smaller cation B located at the centre of an octahedral framework of six X anions, leading to a three-dimensional array of corner sharing octahedra BX_6. The larger A cation lies in the centre of cubo-octahedral holes formed by the octahedra, co-

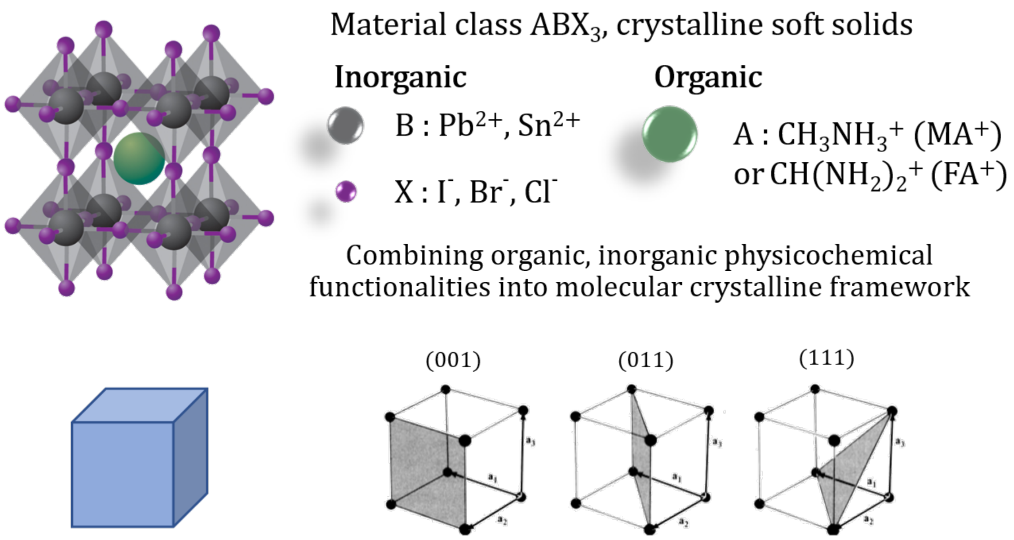

Figure 2.1: Structural design of hybrid perovskites formed by the combination of chemical entities within crystallographic frameworks. Notably, different inorganic and organic atoms and molecules can be combined within molecular crystalline forms to form solid solutions. Adapted from [24] with permission from Springer Nature, copyright 2014

ordinated by 12 X anions. The formability of perovskite structures is given by the Goldschmidt tolerance factor [25] relating the ionic radii to crystal structure:

$$t = \frac{r_A + r_X}{\sqrt{2}\,(r_B + r_X)}. \tag{2.1}$$

The Goldschmidt factor [25] gives an estimate of the kind of lattice symmetry formed by the ions, with a symmetric cubic phase expected when in the range of 0.9-1, wherein the unit cell axis is exemplified as:

$$a = \sqrt{2}\,(r_A + r_X) = 2\,(r_B + r_X) \tag{2.2}$$

where r_A, r_B and r_X are the ionic radii of corresponding ions A, B and X respectively.

When $0.9 < t < 1$, an ideal cubic structure is expected, for $t > 1$, a hexagonal structure is expected and for $t < 0.9$, orthorhombic structures are expected.

2.1.2 Optoelectronic properties

Semiconducting hybrid perovskites possess band gaps in the visible region of the solar spectrum. The band gaps for $MAPbI_3$ is 1.51 eV, for $MAPbBr_3$ is 2.23 eV

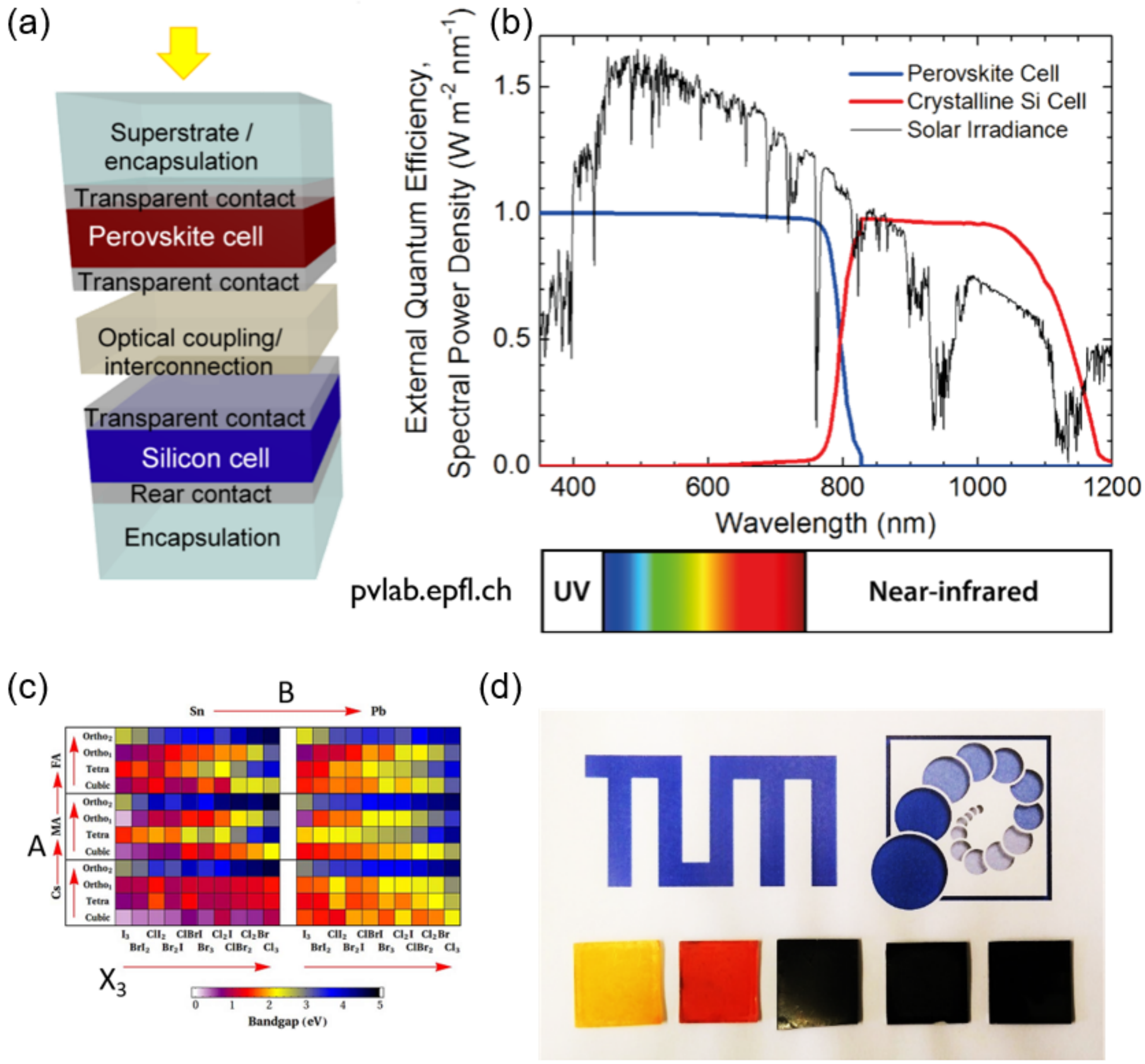

Figure 2.2: Applications of band gap tunability of hybrid perovskites solid solutions. (a) Schematic design of functional layers involved in a Silicon-Perovskite tandem solar cell. (Adapted from pvlab.epfl.ch) (b) External quantum efficiency characteristics of Silicon-Perovskite solar cell showcasing the absorption of radiation ranging from the UV to NIR regions of the electromagnetic spectrum. (Adapted from pvlab.epfl.ch) (c) Chemical management of bandgaps of perovskite based materials and phases by replacement within ABX_3 functional groups. Reprinted with permission from [26]. Copyright American Physical Society 2014. (d) Colorful, semitransparent thin films suitable for tandem photovoltaic applications.

and for $FAPbI_3$ is 1.45 eV. Distinct from the chiefly insulating electrical nature of lead halides, perovskites based on the same lead halides exhibit exotic electrical properties owing to their band structure. The band structure close to the band gap in perovskites is dominated by orbitals from lead and the halide entities, thus the electronic band structure of perovskites is majorly influenced by the inorganic species. The valence band is composed of hybridized Pb 6s and halide p orbitals, while the conduction band primarily bear nonbonding Pb 6p with minor contributions from the halide s orbitals. The organic molecule does not contribute to the band structure as its molecular orbitals are buried energetically deep in the valence band of the inorganic octahedra. It thus serves mostly to balance charge equality. The strong s-p antibonding coupling, results in advantageous optoelectronic properties. Foremost, since the s orbitals in Pb are occupied, there is a resultant p-p transition which is the major reason for strong optical absorption in perovskites through the visible region of the spectra, until the near infrared causing perovskites to boast a band gap in the region from 1.1 – 2.3 eV. However, not all p-p transitions result in high optical absorption. Si undergoes p-p transitions but has comparatively poor optical absorption owing to the fact that it is an indirect bandgap semiconductor. Thus the crystalline symmetry in perovskites has a critical role in establishing direct bandgap transitions. Other common thin-film solar cell materials such as CIGS, CdTe, etc, have no s-p coupling leading to higher effective hole masses and observe a s-p transition which is less intense. These materials rely on the formation of p-n junctions. In case of perovskites, the strong spin-orbit coupling [27] drastically reduces the effective masses of holes in these systems, which is beneficial for high carrier mobilities and small exciton binding energies, attributes which are favorable for solar cells. Since the optical onset of absorption in perovskites has a direct influence on the light harvesting capacity of the solar cell, the precise control of the bandgap presents promising opportunities for devices. Applications include color tuning perovskite-based LEDs and lasers, and for incorporating hybrid perovskites in finely tuned multijunction solar cells [28]. An attractive attribute of hybrid perovskites is the ability of solid solutions based perovskites to continuously tune the absorption onset by alloying different halides into the ABX_3 structure (Figure 2.2). By varying the halide ratios in hybrid perovskites, the bandgap can be tuned across the visible spectrum. The further favorable optoelectronic properties of hybrid perovskites include ambipolar charge transport [29], or the ability to transport positive and negative charge carriers, long diffusion length scales, high dielectric constants [30–32] and benign defects [31,33,34] in trap states and at grain boundaries. $MAPbI_3$ is well suited for applications within planar architectures [35], as the required thickness for absorption of incoming light is lesser than the diffusion length for the material [36, 37].

2.2 Crystalline solids

Within crystalline solids, a crystal is referred to a solid of repeating atoms or ions within a three-dimensional periodic pattern. Unit cells are arranged onto a periodic lattice known as Bravais lattice, characterized by primitive translation vectors $\mathbf{a}_1$, $\mathbf{a}_2$ and $\mathbf{a}_3$, marking the position of the unit cell n by the lattice vector $\vec{R_n}$:

$$\vec{R_n} = n_1\vec{a_1} + n_2\vec{a_2} + n_3\vec{a_3} \tag{2.3}$$

where n_1, n_2, $\mathrm{n}_3 \in \mathbb{Z}$. Further, a lattice vector $\vec{T}$ connects two unit cells:

$$T = R_n - R_m \tag{2.4}$$

and a vector $\vec{G}$ belonging to the reciprocal space:

$$\vec{G_n} = n_1\vec{b_1} + n_2\vec{b_2} + n_3\vec{b_3} \tag{2.5}$$

$$\vec{G_n} \cdot \vec{T} = 2\pi n \tag{2.6}$$

$$\vec{a_n}\vec{b_n} = 2\pi\delta_{nm} \tag{2.7}$$

$$\vec{b_1} = 2\pi\frac{\vec{a_2} \times \vec{a_3}}{\vec{a_1} \cdot (\vec{a_2} \times \vec{a_3})} \tag{2.8}$$

The factors $[\mathrm{n}_1\mathrm{n}_2\mathrm{n}_3]$ give the direction within a crystal. Miller indices $[hkl]$ denote crystallographic directions in the basis of direct lattice vectors. $\langle hkl\rangle$ represent all equivalent symmetry lattice directions, (hkl) represent orthogonal planes to $[hkl]$, whereas $\{hkl\}$ denote the set of equivalent planes. The distance d between (hkl) planes is related to the lattice constant of a cubic crystal a by:

$$\frac{1}{d^2} = \frac{h^2 + k^2 + l^2}{a^2} \tag{2.9}$$

with the angle ϕ between planes $(h_1k_1l_1)$ and $(h_2k_2l_2)$ is given by

$$cos\phi = \frac{h_1h_2 + k_1k_2 + l_1l_2}{\sqrt{(h_1^2 + k_1^2 + l_1^2)(h_2^2 + k_2^2 + l_2^2)}} \tag{2.10}$$

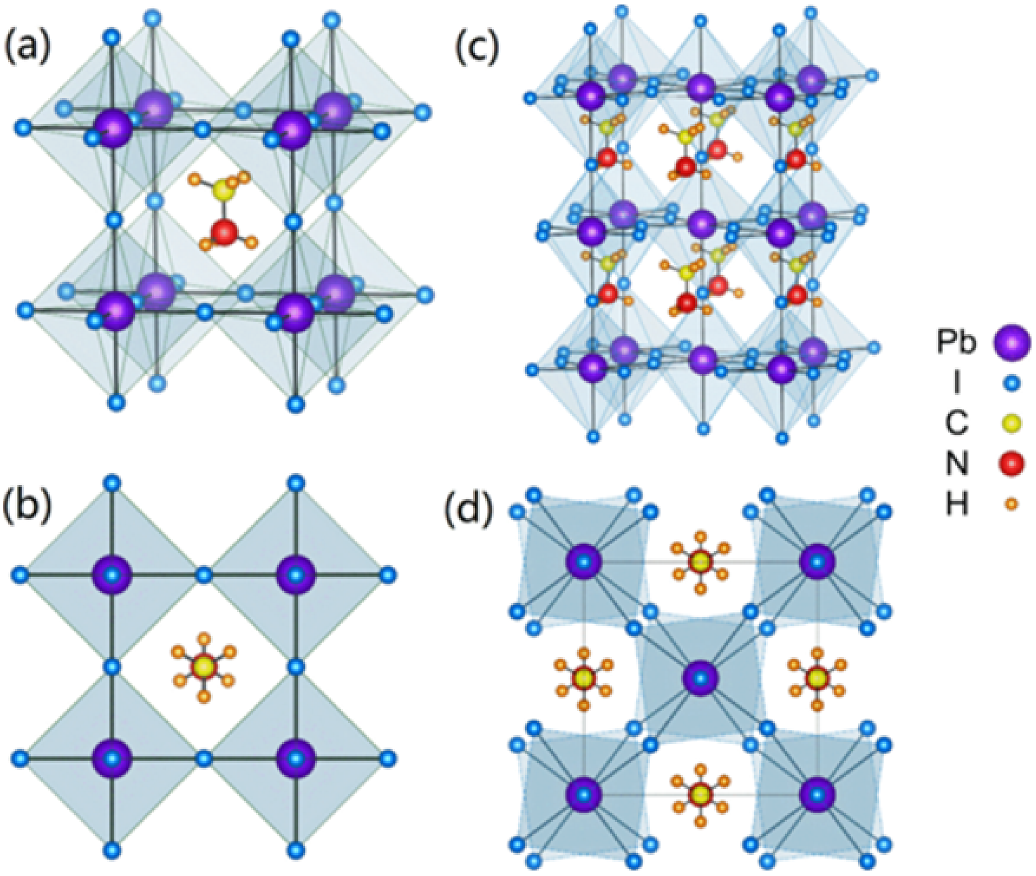

Figure 2.3: (a,b) Cubic and (c,d) tetragonal structures of MAPbI$_3$. The tetragonal structure displays out-of-phase tilting of the plumboiodide octahedra and an elongation about the c-axis. Adapted from [38] with permission from American Physical Society

whereas for a tetragonal crystal

$$\frac{1}{d^2} = \frac{h^2 + k^2}{a^2} + \frac{l^2}{c^2} \tag{2.11}$$

Symmetry point groups refer to a set of symmetry operations, which in combination with the periodicity of Bravais lattice translation vectors yield its space group. The need for compatibility of the point group and Bravais lattice leads to a restriction in the number of point groups. This gives rise to 14 possible Bravais lattices, 32 possible point groups and 230 possible space groups for crystals. The 230 space groups can be reduced to seven crystal systems as per their minimum symmetry. The Hermann-Maugin notation is a way to note the symmetry of a crystal, wherein the lattice type is denoted by an upper case letter, rotation axes are signified by their order of rotation, improper rotations are marked by a macron above the order of rotation, screw axes are marked by the order of rotation with the direction of the axis signified as a subindex, mirror planes are denoted with the letter m, and finally glide planes are marked by a lower case letter according to the axis of glide. $MAPbI_3$, at room temperature belongs to the tetragonal I4cm space group, representing a body-centered tetragonal structure with four rotation axes, a mirror plane and a glide plane along the c-axis.

Hybrid perovskites are known to exist in four phases: a high temperature, symmetric α-phase, an intermediate temperature slightly distorted β-phase, a low temperature, low symmetry γ-phase and a non-perovskite δ-phase. $MAPbBr_3$ bears a symmetric $Pm\bar{3}m$ cubic space group while $FAPbI_3$ crystallizes in a cubic P3m1 space group.

2.3 X-ray scattering

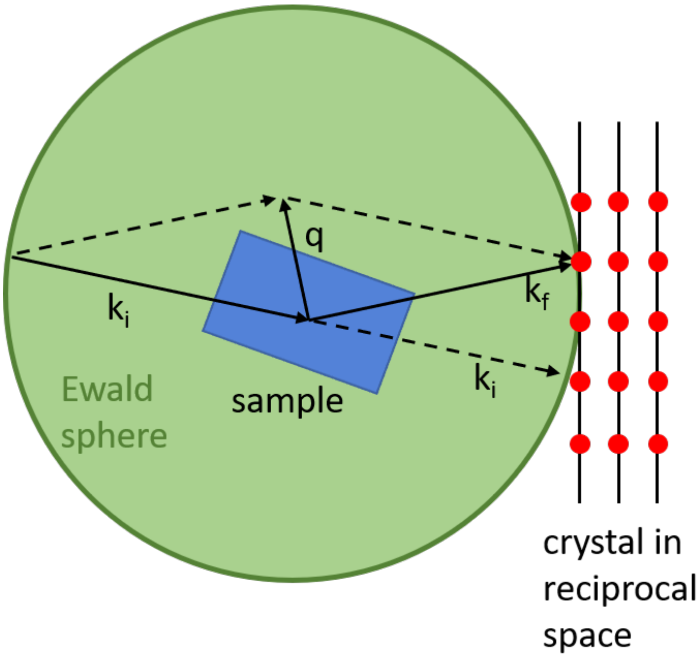

Figure 2.4: Schematic representation of a scattering experiment. A sample is incident with x-rays with a momentum k_i under an incident angle, and undergoes scattering with an outgoing momentum of k_f. Constructive interference is observed under Laue conditions, when material reciprocal space lattice points intersects with the surface of the Ewald sphere (green).

X-rays are utilized as energetic sources to probe the structure of materials as the wavelength of the radiation is of a similar order of magnitude. Materials have distances between constituent atoms in the order of Angströms, hard x-rays with wavelengths around 0.1 nm and energies around 10keV are suitable for investigating the crystal structure of materials. X-ray radiation originate from three kinds of sources including synchrotron sources, bremsstrahlung and characteristic radiation. Characteristic radiation and bremsstrahlung are produced by the acceleration of electrons onto an anode. Electrons are accelerated negatively on impinging an anode leading to the production of dipolar emission. The incoming electrons lead to collision and ejection of inner shell electrons from metals. Thereafter higher energy level electrons relax to lower energy shells, emanating characteristic radiation with energy corresponding to the transition. Lab based x-ray sources utilize such processes for scattering experiments, with the Cu K_α transition from the $2p_{3/2}$ ($K_{\alpha 1}$) or $2p_{1/2}$ ($K_{\alpha 2}$) to the 1s shell being the most commonly utilized transition. The wavelengths for the $K_{\alpha 1}$ radiation is 1.54056 Å and for $K_{\alpha 2}$ radiation is 1.54443 Å, and 1.5418 Å for the combined source.

Synchrotron sources utilize electrons stored and accelerated in a circular orbit within storage rings. Emission of relativistic radiation leads to the generation of horizontally polarized x-rays with high intensity. Metal anode sources undergo heating due to the low conversion efficiencies and their power is limited by cooling rates. Synchrotron sources owing to their high intensities shorten acquisition times and allow for in situ measurements.

A schematic of a basic scattering experiment is represented in Figure 2.4. Herein, within an elastic scattering experiment, the incident beam $\vec{k_i}$ incidents the sample surface at an angle α_i. The beam undergoes diffraction and exits the sample at $\vec{k_f}$. For specular geometries such as XRD, the observed scattering occurs in the xz-scattering plane, and the exit and incidence angles are equal ($\alpha_i = \alpha_f$). The scattering vector represents a mere change in the direction of the incident vector, whereas the modulus remains unchanged.

X-ray diffraction is a versatile tool to characterize the structural properties of materials. An x-ray beam with wavelength λ is incident upon a sample plane with distance between lattice planes d_{hkl}, leading to interference, and especially constructive interference conditions are fulfilled in accordance with Bragg's law:

$$n\lambda = 2d_{hkl}sin\theta \tag{2.12}$$

Within a measurement within the Bragg-Brentano geometry, the x-ray source and the detector are tilted at an angle θ from the sample reference plane, and maintain an angle of 2θ between each other, with the diffraction vector $\vec{q}$ pointing perpendicular to the sample surface. Diffraction peaks gather their intensities from the relative arrangement of atoms within the lattice, given by the structure factor F_{hkl}.

$$I_{hkl} \propto |F_{hkl}|^2 \tag{2.13}$$

The structure factor $\mathrm{F}_{hkl}(\vec{q}) = 0$ for all conditions except when the Laue condition is true.

$$\vec{G} = ha^* + kb^* + lc^* \equiv \vec{q} \tag{2.14}$$

Grazing-incidence wide-angle X-ray scattering (GIWAXS) describes a scattering experiment under a fixed incidence angle with access to crystalline nature of samples. Owing to the placement of the detector, which is close to the sample, large diffraction angles are accessible in comparison to XRD. The outgoing scattering signal bears Debye scattering cones corresponding to every Bragg angle 2θ recorded on an area detector. The recorded signal bears information regarding material phase and crystalline orientations with respect to the sample substrate. The orientations of the crystals is marked by the azimuthal angle χ. A mosaic sample leads to a diffraction pattern with Debye-Scherrer rings with an isotropic distribution of intensities along χ. Owing to the fixed incidence angle, the outgoing scattering signal $\vec{k_f}$ refers to the Ewald sphere and points in the reciprocal space which fulfill the Laue condition lie on its surface. The resultant detector data is corrected leading to a missing-wedge in the data.

2.4 Colloidal precursors

In the formation of perovskite thin films, the necessary solutes are to be dissolved within common solvent media, thereby leading to the formation of colloidal precursors [40, 41]. Several studies have shown that the nature of the precursors has a direct impact on the morphological properties and resultant efficiencies of thin films formed thereof. [29, 42–44] This makes the precursor a central component in the manufacturing of high efficiency photovoltaics. The chemical control over these precursors is imperative for tuning the structural properties of thin films and devices. It is found that the precursors are far from ideal solutions and possess struc-

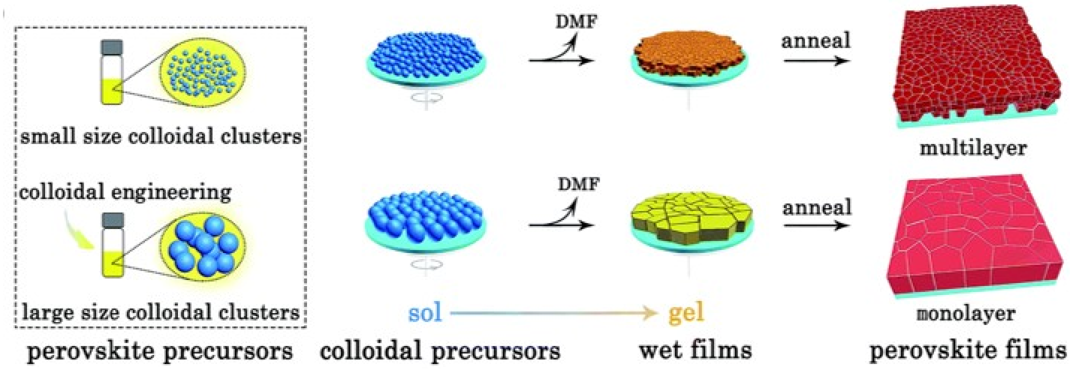

Figure 2.5: Schematic representation of colloidal precursors processed into thin films. Differences arise in thin films processed from precursors containing clusters with different sizes. A transition occurs in the spin coated precursor from a sol state to a gel state on removal of excess solvent during production of wet films. Annealing of the wet films leads to the formation of multilayer of perovskites when processing precursors with small sized colloidal clusters are utilized, whereas monolayer perovskite thin films are resultant on utilization of precursors containing large size colloidal clusters. Reprinted from [39] with permission from Royal Society of Chemistry

tural entitites with tunable physicochemical interactions between them [39, 41]. The colloids are formed of coordination complexes made of lead halide frameworks between the inorganic and organic components, whose coordination extent can be engineered by tuning the ratio of organic and inorganic solutes, [41] the concentration and viscosity of precursor. The nature of the precursors affects thin films formulated from them, and they can be tuned by the nature of the solvents utilized, ratio of organic and inorganic precursors utilized, the overall concentration of precursors employed, etc [18]. The size of the structural entities within the precursor needs to be controlled as it has an impact on the grain size and microstructure of the crystalline thin films. The focus of this thesis is halide perovskites and we utilize colloidal hybrid halide precursors as key materials for their preparation. Based on the results of aforementioned studies, the size and composition of the precursors is expected to have an impact on resultant materials formed thereof. These precursors need to be characterized for their evolving structural and optoelectronic properties to understand the forces of interaction between the chemical species. This is done by tuning the concentration of the precursors utilized and studying the thin films formed from them. The nature of the precursors gives rise to variation in the morphologies in thin films.

2.5 Thin film formation

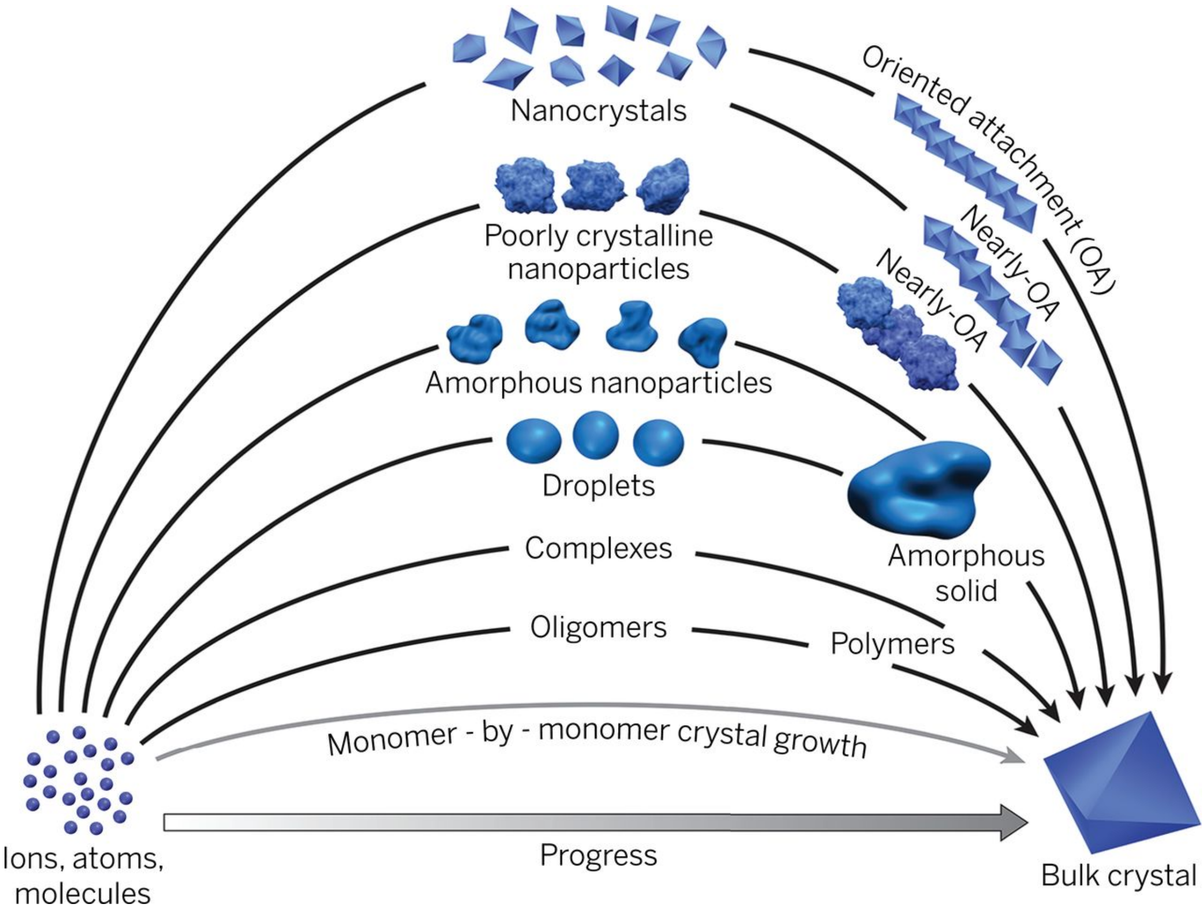

Figure 2.6: Schematic representation of multiple crystallization pathways from precursors. Reproduced from [45] with permission from American Association for the Advancement of Science

Hybrid perovskites are formed in the architecture of thin films. Controlling the film formation processes helps tune their crystalline characteristics. Intensive efforts have been invested for the optimization of thin film quality in terms of film roughness, coverage, heterogeneity, and microstructure in terms of grain size, preferred orientation and removal of undesirable aspects like voids, pinholes etc [46–49]. The complex nature of crystallization and thin film formation has led to numerous studies which combine the effects of the substrate characteristics, precursor chemical properties, nature of solvents and antisolvents and several other processing parameters.

The methods employed for film deposition in this thesis employ 1-step precursor deposition, wherein all precursors are dispersed within suitable common solvents and fabricated into thin films by spin coating. During the spin coating process, supersaturation is induced within the experiment by employing orthogonal solvents or antisolvents, which reduce the solubility of the precursor within common solvents. The material monomers undergo heterogenous nucleation by clustering and precipitating upon the interface [50] of substrate and colloidal precursors. It is also possible for precursors to undergo homogenous nucleation.

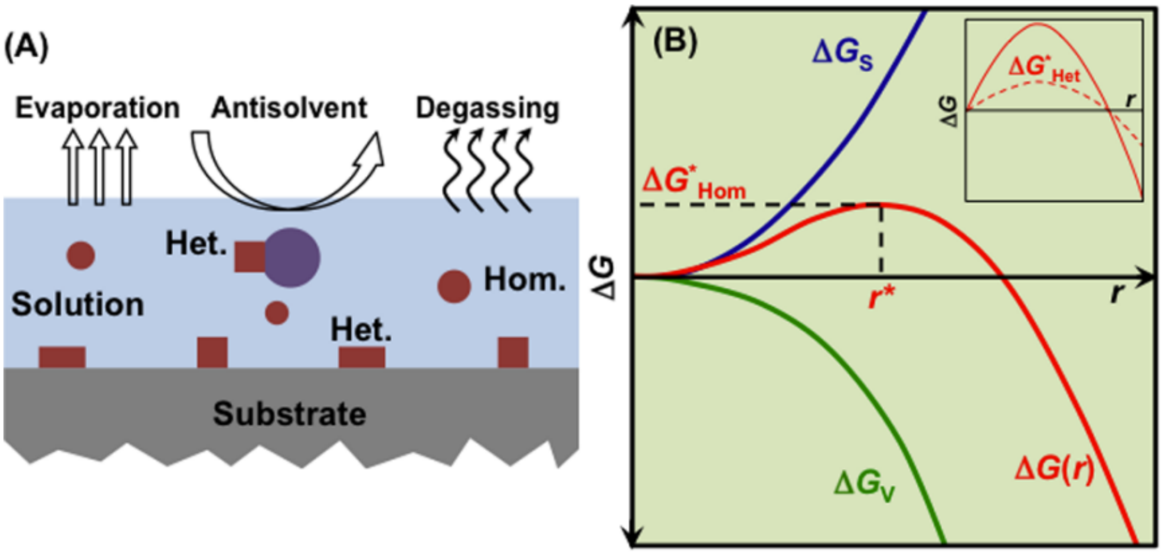

Figure 2.7: (A) Schematic representation of homogenous and heterogenous nucleation within materials loaded on a substrate during supersaturation induced by evaporation, application of antisolvent or degassing. (B) Change in free energy during homogenous nucleation with contributions from surface free energy change (ΔG_s) and volume free energy change (ΔG_v) as a function of particle radius. Inset represents change in free energy during heterogenous nucleation as a function of particle radius. Reprinted from [51] with permission from American Chemical Society

For homogenous nucleation, there is a dependence between the free energy ΔG^*_{hom} and the nuclei radius r, with nuclei above a critical radius being stable and able to grow further, whereas smaller particles undergo redissolution as depicted in Figure 2.7. The process of nucleation can occur at the surface in case of the presence of a substrate or in colloidal precursors, and this reduces the correlated interfacial energy significantly, which in turn makes $\Delta \mathrm{G}^{*}_{het} \ll \Delta \mathrm{G}^{*}_{hom}$ and dependant on the number of interfacial sites [51]. Controlling the density of nucleation sites is crucial for obtaining high quality films. The presence of colloidal particles in precursors, due to the presence of strong polar solvents inducing significant coordination with Pb salts leads to higher rates of nucleation and higher nuclei density. This is also the case when non-halide precursors are employed. [41, 52] It is more facile to control these processes at lower temperatures wherein the nucleation of species is lower. Here, antisolvents are found helpful for inducing supersaturation within precursor fluids, whereas any remaining solvents can be removed by thermal annealing [40]. Nuclei follow a Volmer-Weber type non-epitaxial growth process for reducing the free energy within the system [53]. This causes the growth processes to be limited by diffusion or through interfacial reaction kinetics. [54]

3 Materials and methods

The focus of this thesis is to investigate the structural, optical properties of colloidal perovskite precursors and their subsequent *in situ* transformation to thin films on application of an antisolvent, and further thermal annealing. Further the structural, optical and morphological properties of thin films are investigated. This chapter includes an introduction to materials utilized for sample preparation, methodologies for various sample preparation and basic material characterization methods for studying colloidal precursors, their *in situ* conversion to perovskite thin films and final thin films. Samples were prepared in the form of colloidal dispersions for precursor characterization and for application into thin films during *in situ* crystallization experiments held at the Advanced Light Source. By the utilization of a devoted analytical cell, the various phases of interest are captured during *in situ* crystallization studies.

Prior to the *in situ* studies, a first characterization of the colloidal precursor is done by UV-vis measurements (3.1.1) and Dynamic Light Scattering (3.1.2). Thereafter, thin films are characterized for their surface morphological properties by Optical microscopy, (3.1.3) and Scanning electron microscopy (3.1.4). These techniques provide efficient information about the surface structure of the thin films. This is important, since film topology is an important aspect for perovskite thin films, and crucial to achieve a reliable and comparable understanding of structural, morphological and crystallographic aspects probed during further measurements.

While real-space imaging techniques like SEM and OM scan only scan a small section of the sample, X-ray scattering techniques probe a larger area and yield information with a higher statistical relevance. X-ray diffraction (3.1.6) and grazing incidence wide-angle x-ray scattering (3.1.7) provide information about film composition, surface and inner structure, preferred orientation of various crystallographic phases present within the film. Notably, the data from XRD, and GIWAXS is obtained in reciprocal space and therefore has to be translated to real-space structures.

Carrying out *in situ* measurements is challenging especially when conducted at large scale research facilities with restricted space and time considerations. To realize reliable *in situ* studies, in particular during processing of thin films by spin coating, antisolvent drop and annealing and measuring sophisticated techniques, such as PL and GIWAXS, an analytical cell was designed and developed. The core of the sample environment is a spin coater, heater enclosed in a 3D printed cylindrical chamber. Equipped with functional ports for holding metrological equipment, the analytical cell provides a fast installation routine at multiple instruments. The design and working principle of the sample chamber is discussed (3.3).

3.1 Characterization techniques

The aim of this thesis is to investigate the optical, structural and morphological characteristics of perovskite precursors and resultant thin films. For this purpose, a combination of characterization techniques are employed which are described in this section.

3.1.1 UV-vis spectroscopy

UV-vis spectroscopy is a widely used method of characterization of absorption properties of materials. It includes probing materials with excitation probes ranging from wavelengths of 200 nm – 900 nm. Incidentally, this also corresponds to the energy range within which electronic transitions imparting color in the visible range of the electromagnetic spectrum take place. The technique thus characterizes the absorption properties of materials by probing optical transitions to their excited states, and utilizing this knowledge to analyze the material's electronic properties. Unlike other spectroscopic techniques, a UV-vis spectrum does not contain sharp peaks, but rather has broad features throughout the spectra. This is because UV-Vis spectroscopy characterizes electronic transitions occurring in materials. Electronic levels in materials are not distinct, but rather contain several vibrational and rotational levels of energy. Thus an electronic transition occurs in various vibrational and rotational energy levels, causing broad energetic peaks, as seen in Figure 3.1.

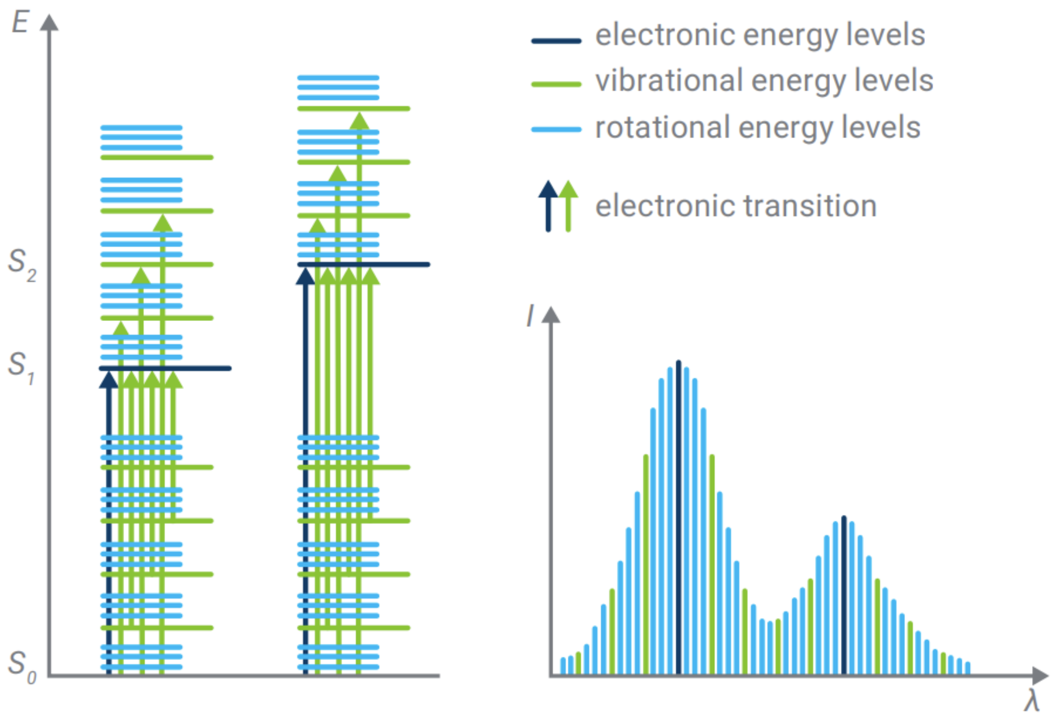

Figure 3.1: Continuous and broad UV-vis spectrum of materials arising out of characteristic electronic transitions with underlying vibrational and rotational sub-energy levels. Image taken from [55]

UV-Vis spectroscopy allows for optical transmission and reflection spectra to be measured through a spectrometer which consist of a light source, a monochromator, a sample holder and a detector. The sample may be placed in transmission or reflection geometry by positioning the sample in front of or at the end of an integrating sphere. In the transmission geometry, only the light transmitted through the sample reaches the detector. In the reflection geometry, the scattered and reflected light reach the detector. The measured data is treated and can be used qualitatively to study the absorption properties of samples in solid or liquid phase.

The intensity of light transmitted by the sample I is measured against the intensity of initial light I_0, which gives the transmittance $T(\lambda)$ of the material. The transmittance of a material is then defined by the Beer-Lambert's law:

$$T(\lambda) \;=\; \frac{I(\lambda)}{I_0(\lambda)} \;=\; exp(-\beta(\lambda)d) \tag{3.1}$$

with the sample thickness d and absorption coefficient β. To compensate for the transmittance of the substrate, a reference measurement is conducted for the correction of the signal from the sample, and the transmittance of the thin film is then given by:

$$T(\lambda) \;=\; \frac{T_{raw}(\lambda)}{T_{ref}(\lambda)} \tag{3.2}$$

where T_{raw} is the measured transmittance and T_{ref} is the contribution from the substrate. The absorbance $\mathrm{A}(\lambda)$ of a material can be calculated from the transmittance by:

$$A(\lambda) \;=\; \frac{\beta(\lambda)d}{ln\ 10} \;=\; -log_{10}T(\lambda) \tag{3.3}$$

The absorption coefficient β is a material specific parameter which is normalized to the sample thickness and allows for facile comparison between samples. For obtaining a complete picture of the absorption characteristics of the material, reflection measurements were made with the help of an integrating sphere. UV-Vis measurements were carried out on a spectrometer from a PerkinElmer Lambda 650S setup, with a 150 mm integrating sphere. It utilized dual light sources; a tungsten lamp for wavelengths from 900 nm to 319.3 nm, thereafter which there was a lamp switch to the deuterium lamp which provided wavelengths from 319 nm to 250 nm. For measurement of the colloidal precursors, a PerkinElmer Lambda 35 UV-Vis spectrometer was utilized. The spectrometer had a wavelength range from 1100 nm to 190 nm. It too utilizes a dual light source, with a tungsten halogen lamp utilized for wavelengths ranging from 1100 nm to 326 nm, and a deuterium lamp for wavelengths ranging from 326 nm to 190 nm. A scanning rate of 267 nm/min is employed with 1 nm slits. Prior to sample measurements, the device is calibrated to 100% and 0% transmitted intensity for blank beam and blocked-beam measurements. The recorded transmittance for each measurement is normalized to 1.

3.1.2 Dynamic light scattering

This section is based on ref [56]. Dynamic Light Scattering (DLS) is an important metrological technique utilized for determining the distribution of particle sizes within colloidal dispersions, allowing for detection of particle sizes down to 1 nm. The technique measures the sizes, and more precisely the average hydrodynamic radii of particles in dispersions due to Brownian motion. During measurements, a coherent monochromatic beam of light illuminates the sample. Brownian motion leads to fluctuation in the particle position which causes fluctuation in the intensity of light scattered by particles. The fluctuations in intensity are measured as a function of time and input into a correlator. The diffusion coefficient of the scatterers in the sample is estimated from the rate of decay of scattered light fluctuations. This rate of decay is lower for larger particles as compared to smaller particles. The correlation is represented by means of a correlation function, with a correlation coefficient C, where C = 1 signifies perfect correlation and C = 0 signifies no correlation.

The output of DLS measurements is normalized time autocorrelation function $\mathrm{G}^{(2)}(\tau)$ of the scattered light intensity fluctuation, given by:

$$G^{(2)}(\tau) \;=\; \frac{\langle I(t)\rangle\langle I(t+\tau)\rangle}{\langle I(t)\rangle^2} \tag{3.4}$$

with $\langle I(t)\rangle$ being the initial scattered intensity at time t, and $\langle I(t+\tau)\rangle$ being the scattered intensity after a time delay τ.

The correlation after a short time interval is high, and the intensity is unchanged, while the correlation at longer time delays decreases, with exponential decay in the correlation function, reaching zero when intensity correlation is lost.

The fluctuations in scattered intensity are correlated with fluctuations in the electric field, where the correlation function of the scattered electric field is obtained by the Siegert relation:

$$G^{(2)}(\tau) = 1 + \beta[G^{(1)}(\tau)]^2 \tag{3.5}$$

where β is the coherence factor determined by the geometry of the instrument representing the scattered light's degree of spatial coherence over the detector. For a monodisperse dispersion or a dilute suspension, the correlation function decays with a decay rate Γ:

$$G^{(1)}(\tau) \;=\; e^{-\Gamma\tau} \tag{3.6}$$

The decay rate Γ is related to the correlation time τ and the translational diffusion coefficient D_t as:

$$\Gamma \;=\; D_t q^2 \tag{3.7}$$

and the momentum transfer q is given by:

$$q = \frac{4\pi n_0}{\lambda_0} sin \frac{\theta}{2} \tag{3.8}$$

where λ_0 refers to the wavelength of the incident laser beam, n_0 refers to the refractive index of the sample dispersion and θ is the scattering angle between the detector and the sample.
The Stokes-Einstein equation then determines the hydrodynamic radius of the sample, which is linked to the diffusion coefficient of the molecule:

$$D \;=\; \frac{k_B T}{6\pi\eta_0 R_H} \tag{3.9}$$

where k_B is the Boltzmann's constant, η_0 is the solution viscosity, T is the absolute temperature and R_H is the hydrodynamic radius.

For polydisperse samples of two different particle sizes, the autocorrelation function is a sum of two exponential decays for the individual species:

$$G^{(1)}(\tau) \;=\; A_1[e^{-\Gamma_1\tau}] \;+\; A_2[e^{-\Gamma_2\tau}] \tag{3.10}$$

where ($A_1 + A_2 = 1$) are the amplitudes of decay modes, Γ_1 and Γ_2 are the inverse of correlation times τ_1 and τ_2.

DLS measurements are conducted on a 3D LS Spectrometer from LS Instruments with a 632.8 nm, 21 mW HeNe laser source. The instrument can measure particle sizes from 0.15 nm to 5 µm, determined by the kind of solvent and dispersed particles. A laser is utilized as a light source to illuminate a sample, contained in a quartz glass cell, surrounded by decalin, due to the refractive index of decalin being the same as quartz glass.

3.1.3 Optical microscopy

The optical microscope functions by utilizing visible light and a lens system for the creation of magnified images of objects. It is well suited to resolve micron length scale structures and visualize the topology of thin film surfaces.

In order to evaluate the thin film microstructure, topology and overall homogeneity, optical microscopy was employed. Measurements were performed on a Zeiss Axiolab A microscope and microscopy images were recorded over a 1280 x 1024 px^2 PixeLink USB CCD camera with 1.25x, 2.5x, 10x, 50x and 100x magnification. ImageJ software was utilized for analysis and real space distances were calculated according to transformation factors listed in Table 3.1.

magnification	NA	R (λ = 700 nm) [μm]	pixel size [μm]
1.25	0.035	12.2	6.258
2.5	0.075	5.7	3.2
10	0.20	2.1	0.8
50	0.70	0.61	0.16
100	0.75	0.57	0.08

Table 3.1: Magnification, Numerical aperture, resolution and pixel size for the available objectives of the Axiolab A optical microscope.

The resolution limit is given by

$$R = \frac{1.22\ \lambda}{2\ NA} \tag{3.11}$$

where NA is the numerical aperture, λ is the wavelength of the illumination source.

3.1.4 Scanning electron microscopy

Scanning electron microscopy (SEM) is a useful way to probe and characterize surface morphologies at the nanoscale. The technique utilizes probing a material with electrons. The de Broglie wavelength of electrons (within the picometer regime) is shorter than that of visible radiation, which increases its resolution manifold, as compared to visible light, reaching resolutions as low as 1 nm. The source of the excitation probe electrons is typically a heated tungsten filament, with a potential that may be tuned between 3 - 30 kV. Typical excitation voltages of 5 kV are used to characterize perovskite samples. Initially, electrons are generated by an electron gun with a defined kinetic energy by field emission or thermal emission. It is possible to generate electrons by a combination of both effects. The generated electron beam is collimated and focussed with the aid of electromagnetic lenses which defines the shape and size of the electron beam. An aperture defines the beam size and scan coils are utilized for guiding the beam over the sample surface to a desired position for raster scanning a region of interest. On hitting the source surface, the incident electrons penetrate the sample and are scattered, thereby emitting lower energy secondary electrons, providing topographical contrast. The incident electrons generate a plume within the sample which contributes to the detected signal. These secondary electrons are recorded by a detector which scans through the surface at each point to reconstruct a nanoscopic image of the sample. SEM at any given time provides a local image of the sample being measured. The quality of the image is affected by the contrast of the signal. Contrast of secondary electrons depends on the atomic number of the element, surface work function and surface topography. Within samples of the same material and with topological variance, areas with increased height appear brighter owing to reduced working distances compared to regions with reduced height and topography. Conducting carbon tape is utilized to prevent charging effects within the sample which diminish the contrast of the material. SEM measurements were carried out using a Gemini NVision 40 FIB-SEM by Zeiss. A schematic of the instrument is given in Figure **??**.

3.1.5 Photoluminescence spectroscopy

The energetic landscape of a material is given by photoluminescence response. On being excited by incoming radiation (phototexcitation), PL refers to the material's capacity to emit light (luminescence). Within PL measurements, a material is excited with photons which can be absorbed by the sample (excitation energy is usually slightly larger than the absorption maxima of a specific absorption transition). The PL intensity, in the simplest case signifies the amount of incoming radiation exciting a particular energetic transition within the material. Material emission on photoexcitation arises from two mechanisms: phosphorescence and fluorescence. Phosphorescence refers to a slow relaxation process resulting in a delayed emission due to a change in the spin multiplicity of the transition. Fluorescence refers to the emission on a rapid decay of an excited state to the ground state of the material. Photoluminescence spectra in this thesis are recorded by an OceanOptics QE Pro spectrometer through an optical fiber. Samples are illuminated through solid state laser diodes of 532 nm or 405 nm.

3.1.6 X-ray diffraction

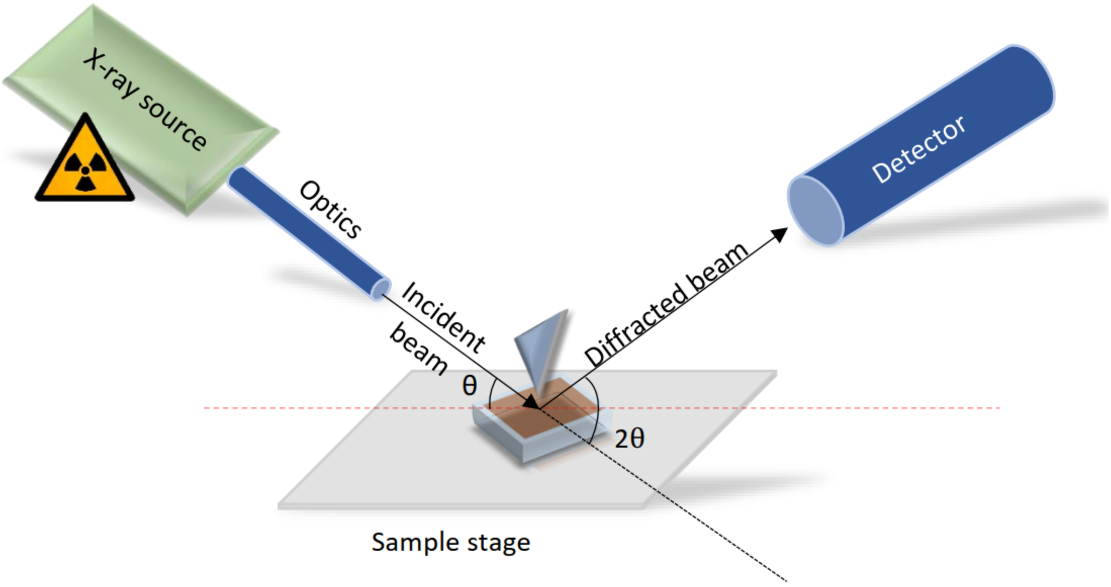

Figure 3.2: Schematic figure of an x-ray diffractometer

X-ray diffraction is a standard technique utilized to probe crystalline structures at an atomic level. The method is sensitive to thin films of atomic dimensions of thicknesses of many tens of microns. Since the advent of the technology, x-ray diffraction enables fingerprint characterization of ordered materials as each solid has a unique scattering pattern. X-ray methods are generally non-destructive, and they can provide a facile route to obtain structural information on thin films and multilayers. Briefly, an incident photon wave encounters an electron density from atoms and undergoes elastic scattering, and as a result experiences diffraction in case of the presence of periodic structures, for crystalline lattices. The angle of the diffracted beam gives information about the sample crystal structure whilst the intensity of the received signal at each angle provides information about how much of the sampled volume has that periodicity. X-rays are utilized towards this end, as the lattice plane spacings are of the order of the wavelength of x-rays. X-ray diffraction measurements on crystalline thin films were carried out on a Bruker D8 advance diffractometer, employing Cu-K radiation (8 keV/ 1.5418 Å) operated at 40 kV and 40 mA. Three Soller slits were used to collimate the incoming beam and minimize parasitic scattering effects, with widths of 0.2 mm, 0.2 mm and 0.1 mm respectively. A knife edge was placed above the surface in order to truncate photon footprints from the substrate. Prior to measurements, the setup is aligned as follows. First, the source is lined up with the detector by removing the sample from the beam path. X-ray scattered intensity was plotted against 2θ, keeping the incident angle constant. The second step was to align the sample to the incoming beam. This was done at a vertical position so as to cut-off the scattered intensity from the sample at half its maximum value. The final alignment step was a rocking scan between the source and the sample, measuring the variation of scattered intensity, as a function of the incident angle, to ensure that the detector was in line with the sample. Finally, the sample was scanned under the Bragg-Brentano reflection geometry to record the diffraction pattern. Briefly, incoming radiation was incident at an angle θ with respect to the surface of the sample, and the scattered interference signal was recorded at angles of 2θ, with respect to the incident beam. The geometry maintained the diffraction vector normal to the surface of the sample. Outgoing radiation was recorded by a Lynxeye silicon strip detector. The angles θ which satisfy the diffraction conditions give a diffraction peak and this information can then be used to determine the interplanar distance.

3.1.7 Grazing incidence wide-angle x-ray scattering

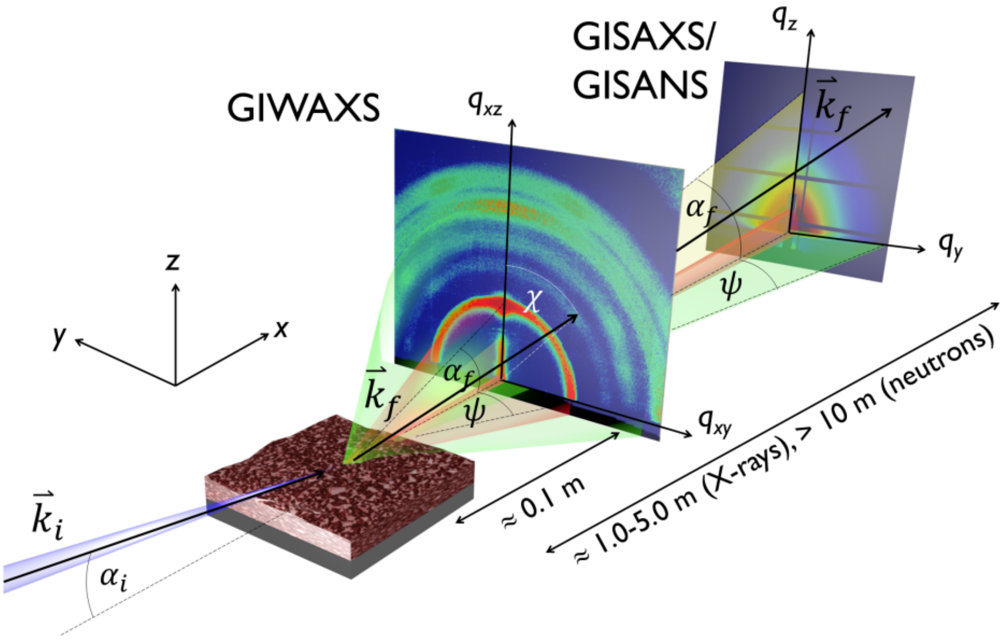

Figure 3.3: Schematic illustration of a Grazing incidence wide-angle x-ray scattering experiment for the characterization of thin film characteristics. An x-ray beam is impinging a sample under a shallow incidence angle α_i. The scattered x-ray beam is characterized by scattered wave $\vec{k_f}$, an in-plane exit angle α_f, an out-of-plane exit angle ψ and an azimuthal scattering angle χ. The outgoing signal is recorded on an area detector. By tuning the sample-detector distance, one can probe different regimes of material characteristics. Under short sample-detector distances, in GIWAXS information on crystallographic properties is obtained. At larger distances in GISAXS, information about material domains and arrangement is gained. Adapted from [57] with permission of John Wiley and Sons.

This section is based on the ref [57]. The morphologies of thin films vary throughout the depth of the film due to the presence of interfaces that lead to different kinds of interactions of the film components with their surroundings. Grazing incidence wide-angle x-ray scattering (GIWAXS) is a methodology which enables non-destructive structural investigation of materials, especially thin films. Such studies provide information on thin film crystallinity, preferred orientations and morphology in a non-destructive manner. By varying the sample to detector distance (SDD), real space distances ranging in the sub-nm regime can be probed. Contrary to real space imaging techniques that sample small surfaces and areas, GIWAXS measurements probe inner film volumes and provide information on film thicknesses. Under grazing incidence, by choosing a shallow incident angle, large footprints of the sample can be illuminated, reaching areas of a few cm^2 and contributing to larger scattering volumes for better statistics. The grazing incidence also probes the sample interior, as compared to transmission geometry. In Figure 3.3, a schematic setup of a GIWAXS experiment is depicted. The frame of reference of the sample is placed such that x points in the direction of the x-ray beam and z points normal to the sample. The sample is tilted at an incident angle α_i, typically $< 1°$ versus the incoming x-ray beam. The incident x-ray beam with momentum q_i is scattered and exits the sample at a vertical exit angle α_f with respect to sample surface with a momentum of q_f. The exit angle spans an angle of $\alpha_i + \alpha_f$ with respect to the incoming beam and spans a lateral angle ψ with the xz specular plane. An area detector positioned at a distance SDD records the scattered diffused intensity as a function of the scattering angle, at the scattering vector q_f. Intensity maxima are recorded at the Bragg angle 2θ on the detector. As per Bragg's law, the scattering angle 2θ signify net d spacings on length scales ranging from Å to nm regime. For maximizing sample volume and the scattering signal, a small incident angle α_i is employed. In order to limit the scattering signal from the substrate, incident angles smaller than the critical angle of the substrate are employed such that the scattering signal is mostly from the sample material, whose critical angle is smaller than the incidence angle. The wide exit angle is attained through shorter SDD which give rise to diffraction maxima at larger angles. Moreover, the wide exit angle has the advantage of measuring large values of momentum transfers and thus affords crystallographic information. Owing to the grazing incidence geometry, there is a loss in symmetry within the anisotropy of the scattered signal at the substrate-film interface of the thin film. The q_x component of the scattering vector q can not be neglected as q splits into a specular q_{xz} component and a q_{xy} component in the sample plane. The q$_z$ component, perpendicular to the sample surface is accessible for $q_y = q_x = 0$. This condition is true when lateral divergence $(\psi_f) = 0$ under the specular condition $\alpha_f = \alpha_i$. This gives rise to a missing wedge in diffuse scattering of GIWAXS when 2D scattering patterns are mapped in the q_r-q_z representation. Inaccessible data from the missing wedge region can be measured by XRD as a complementary measurement technique. Within XRD, the specular reflection is directly measured, herein $\alpha_i = \alpha_f$ and q_z is directly accessible.

GIWAXS experiments were conducted on a Cu K_α equipped Saxslab Ganesha 300 XL SAXS-WAXS setup. The Xenocs GeniX^{3}d Cu ULD SL consists of a copper anode producing a high flux of 10^8 photons/s, operated at 49.79 kV and 0.59 mA with an energy of 8.047 keV. Beam collimation is accomplished through a system of three slits of dimensions 0.4 x 0.4 mm^2, 1 x 1 mm^2 and 0.3 x 0.05 mm^2. An incidence angle of 0.4°, above the critical angle of hybrid perovskites was employed, with a SDD in the range of 100 mm. A Pilatus 300k detector containing 619 x 487 silicon single photon counters was employed, with a pixel size of 0.172 x 0.172 µm^2 and a thickness of 0.32 mm. The detector is considered noise free owing to the employed cooling system. Measurements were conducted at a pressure of 1.87 x 10^{-2} mbar. Data treatment was conducted through the MATLAB based software GIXSGUI [58], providing a graphical user interface for the GIXSDATA toolbox, developed by Zhang Jiang from the Advanced Photon Source at the Argonne National Laboratory. Firstly, the experimental details are input into the software, with the direct beam details obtained from the direct beam empty measurement. The position of the specular peak is utilized for the determination of the direction of the scattering plane, and if needed, for the correction of tilt corrections. Corrections to the solid area are applied through the software. Measurements in the Saxslab Ganesha are conducted in vacuum, thus the effective path length for efficiency corrections is set to 0. For laboratory x-ray sources, the x-ray source is unpolarized. Reshaping the 2D data to q_r vs q_z requires the input of the detector dimensions. The powder integrations are conducted with input of the detector dimensions, and signals at higher exit angles are truncated in higher values of the solid angle. By comparison to XRD data, corrections to SDD in GIWAXS measurements can be made. Azimuthal cuts can be utilized for determining the extent of preferential orientation with respect to isotropic orientation.

3.2 Synchrotron source

In situ experiments in the multimodal analytical cell were carried out at the 12.3.2 Microdiffraction beamline at the Advanced Light Source, Lawrence Berkeley National Laboratory. Hard x-rays in the energy spectrum of 6 - 22 keV from the synchrotron source were focused into the experimental hutch through a toroidal mirror, and further focused to a spot with the aid of roll slits and KB mirrors. Measurements were carried out at an energy of 10 keV with $\sim 10^9$ photons focused onto a spot size of 10 µm x 10 µm. Data were collected within a shallow incidence geometry of 1° incidence angle. Data were collected on a Pilatus 1 M detector placed at an angle of at a frame rate of 1 frame sec^{-1}. The sample detector distance (SDD) was $\sim$ 155 mm and the detector was positioned at an angle of 39° from the sample plane.

3.3 Analytical cell for following *in situ* crystallization

This section is based on the publication
”Probing the in situ dynamics of structure–property evolution in hybrid perovskite thin films spincoated from complex fluids by a custom-designed beamline-compatible multimodal measurement chamber”
S. Pratap, N. Tamura, C. Stan, Z. Yuan, H. Goudey, A. MacDowell, T.-B. Song, N. Barchi, P. Müller-Buschbaum, C. Sutter-Fella and J. Slack, *Acta Crystallographica* **2019**, a75, a155-a156;
DOI: 10.1107/S0108767319098441
Reprinted with permission from IUCrJ, Copyright 2019.

Understanding both the structure and properties of thin films during formation *in situ* is crucial to fundamental and applied science and in developing new materials with desirable properties. This is particularly true in the case of hybrid organic-inorganic perovskites, where photoluminescence measurements show chemical evolution on the second to minute time scale, but previous structural measurements were performed ex situ, in some cases many hours later. Here an experimental sample cell is developed that mimics common laboratory thin film formation conditions while being installed inside a synchrotron hutch. The sample cell combines remote precursor injection, spin coating, and heating, with IR thermography, photoluminescence spectroscopy and x-ray diffraction measurements in real time. It is automated and portable, and available for use by interested scientists in cooperation with the Advanced Light Source and the Joint Center for Artificial Photosynthesis at Lawrence Berkeley National Laboratory. A technical drawing of the analytical cell is presented in Figure 3.4.

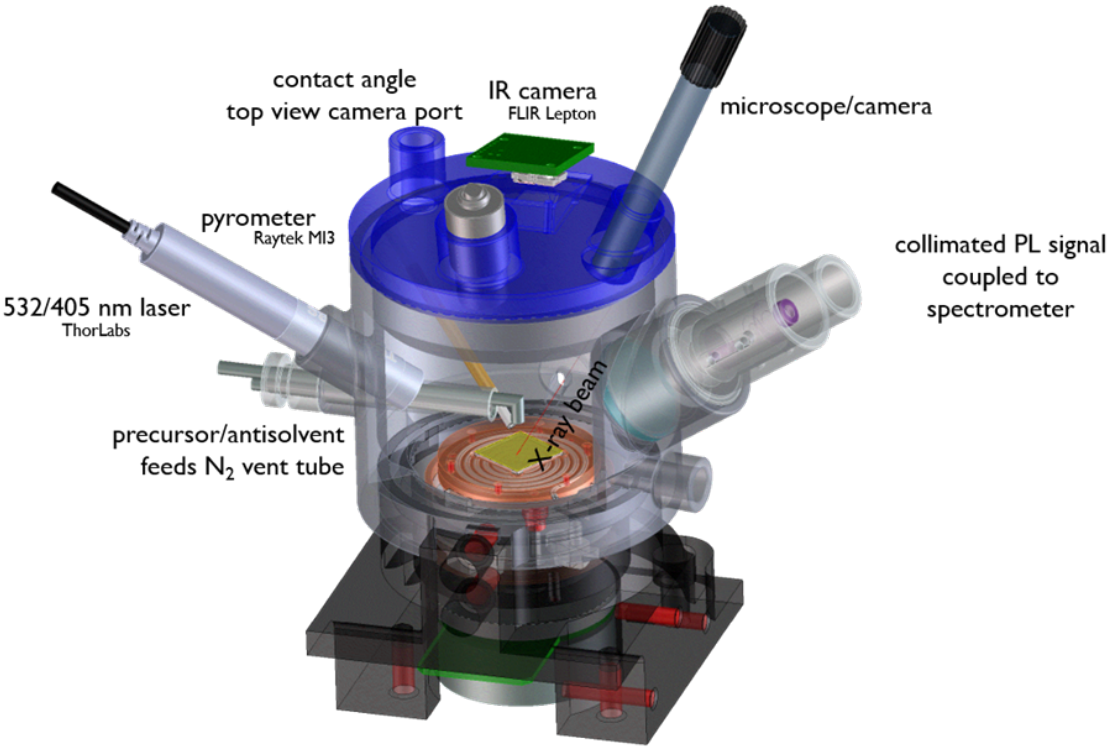

Figure 3.4: Multimodal analytical cell to follow the *in situ* crystallization of thin films. The cell contains a spin coating copper puck with embedded resistive heating elements upon which a substrate is placed. Fluid precursors are dispensed through the precursor feed tubes upon the surface of substrates through remotely controlled syringe pumps. The sample is illuminated by an excitation laser positioned in the 3 D printed body of the chamber, outgoing photoluminescence signal is captured via a plano-convex lens and collimated to a spectrometer. An incident x-ray beam impinges the sample under shallow angles and the outgoing GIWAXS signal is captured through an exit window at the fron of the cell on an area detector. The temperature of the resistively heated copper puck is monitored via a pre-calibrated pyrometer and an IR camera. placed at the top lid of the cell. The experiment is observed with a USB microscope positioned at the top of the cell. Reprinted from [20] with permission from IUCrJ.

The cell consists of multiple metrological equipment for the simultaneous processing of thin films out of fluid precursors formed by the antisolvent route of crystallization. The setup included a removable spin coating stage serving as the sample holder, here referred to as the copper "puck" placed at the heart of the body of the 3-d printed chamber. The copper puck (38 mm diameter) was magnetically coupled and powered to spin through a flat, brushless DC servo motor. The appropriate placement of the spinning puck to the motor shaft was ensured by 3 strong magnetic elements, placed at the lower copper disc of the puck. The magnets were positioned 120° apart on a circular plane, facilitating the puck to be concentrically placed to the spinning shaft of the motor. The substrates were placed at the centre of the top surface of the circular puck, adhered through a uniform layer of heat transfer paste. Fluids of interest were remotely dispensed via distinct ports built into the body of the setup, with a specialized port which enabled fluid dispensing at right angles to the spinning/ stationary film, via syringe pumps (New Era Syringe Pump, NE-1000). The multiple microfluidics ports were designed in order to account for varying surface tension, capillary forces exhibited by different fluids and precursors. Spincoating was triggered remotely, with user defined spinning protocol(s), controlled via a servo motor controller. The spincoated thin film was annealed on the puck itself pre/post spincoating realized by resistive heating. A glass fiber clad Nichrome heating element was wound in a spiralled fashion to regulate heat distribution through the copper discs, between which the nichrome element was sandwiched itself. Heating was realized through pneumatically triggered actuators, connected to user-controllable electrical power supply. The temperature of the substrate was regulated through monitoring the temperature of pre-measured, calibrated high emissivity surfaces via the output of a pyrometer (Raytek MI3, 20 LTS), which was housed in the top cover of the spincoater. The temperature output of the pyrometer was coupled to a PID loop, through a Keysight 34970A data acquisition / data logger which tracked and recorded the temperature of the puck and the substrate. Local variations in temperature/ emissivity were visualized and monitored via a radiometric IR camera (Flir Lepton 3.5) with an interface board (PureThermal 2). While the pyrometer regulated a spot temperature, the radiometric IR camera visualized temperature, emissivity fluctuations throughout the puck and edges of the chamber. Ports were designed for implementation of optics required for conducting PL measurements. An entry port for generic laser modules (Thorlabs) directed the illumination of representative spots on the film surface, which were simultaneously probed via GIWAXS. The outcoming PL signal was focused and transmitted via a 1” plano convex lens integrated into the body of the chamber, collimated by a fiber optics compatible collimating head (F220SMA, Thorlabs) and coupled to a portable spectrometer (QE Pro, Ocean Optics) through an optical fiber (Thorlabs). The incumbent laser wavelength was filtered via appropriate 1” outer diameter long pass filters (FEL, Thorlabs), placed in the outgoing path of the PL signal, between the 1” plano convex lens and the collimator head. A port for the incident x-rays was planned with a large window, in order to be able to tune a large range of incident angles between the x-rays and the substrate and a kapton window placed at the diagonal opposite of the incoming port, with a sufficiently large exit window, ensuring outgoing diffraction signals upto 57° being captured via the area detector (Pilatus 1M). The entire setup was flushed with a flow gas of choice (N_2) with user-control over partial / overpressure to regulate atmospheric conditions critical for experimentation. The entire setup was placed upon a motorized stage.

3.4 Materials

In the following section, the basic materials utilized during the preparation of samples in this work are described.

Glass

Microscope glass slides (76 mm x 26 mm, 1mm thick, soda lime glass) from Carl Roth GmbH, Karlsruhe, Germany were cut with a glass cutter to the required dimensions and used as substrates for film formation.

Mesoporous titania

Mesoporous titania was utilized as the substrate and electron transport material upon which perovskite films were fabricated. A nanocrystalline transparent paste from Dyesol (30 NR-D) was utilized. The titania paste was dispersed in ethanol by preparing a 1:5 v:v dispersion and utilized for spin coating thin films of mesoporous titania.

Lead iodide

Lead iodide (PbI_2) was employed as an inorganic precursor and a source of lead and iodide ions. The here employed lead iodide was obtained from Sigma-Aldrich Inc. (99% purity).

Lead bromide

Lead bromide ($PbBr_2$) was employed as inorganic salt and source of bromide and lead ions. The here employed lead bromide was utilized as is from Alfa Aesar (98% purity).

Methylammonium iodide

Methylammonium iodide was utilized as the source of organic methylammonium ions and inorganic iodide ions. The salt was obtained and utilized as is from Solaronix S.A.

Methylammonium bromide

Methylammonium bromide was utilized as the source of organic methylammonium ions and inorganic bromide ions. The salt was obtained and utilized as is from Greatcell Solar (formerly Dyesol).

Formamidinium iodide

Formamidinium iodide was employed as the source of organic formamidinium ions and inorganic iodide ions. The salt was obtained and utilized as is from Greatcell Solar (formerly Dyesol).

Dimethylformamide

N,N-Dimethylformamide (anhydrous) (>99.8%) from Sigma Aldrich Inc was utilized as the solvent for dissolving and preparation of perovskite precursors. The solvent was stored in the glovebox.

Dimethylsulfoxide

Dimethylsulfoxide (>99.9%) from Sigma Aldrich Inc was utilized as a solvent for dissolving and preparation of perovskite precursors. The solvent was stored in the glovebox.

Chlorobenzene

Chlorobenzene from Sigma Aldrich was utilized as an antisolvent for the preparation of crystalline perovskite thin films. The solvent was stored in the glovebox.

3.5 Sample preparation

Preparation of glass substrates

The standard glass substrates with a thickness of 1 mm were cut into desired dimensions with a diamond cutter. Thereafter, the substrates were washed by sequential rinsing and sonication with deionized water, Alconox soap solution, deionized water, ethanol, acetone and isopropanol respectively. After cleaning, the glass slides were dried with compressed air or nitrogen.

Plasma treatment

After washing and drying, the glass substrates were subject to oxygen plasma treatment. This step was carried out to remove any organic residues from the cleaning protocol by ashing. The pressure of the treatment chamber was lowered to around 0.3 mbar, with a working power of 250 W. The procedure was carried out for 10 minutes to afford plasma cleaned, uniform substrate, that provided better wettability for polar precursors.

Precursor preparation

All precursor preparations were carried out in a glove box, as the precursor salts are known to be hygroscopic in nature. The precursor preparation proceeds in two steps and was carried out at room temperature. In the first step, the inorganic salt was weighed on a digital scale. This salt was dissolved within a solvent mixture of 4:1 DMF:DMSO according to a desired molarity, typically 1M by stirring with a magnetic stirring bar. To ensure full dissolution of the inorganic salt, if needed, the solution was heated on a heating block, and cooled thereafter to prepare the inorganic precursor. In the second step, targeted weights of the organic salt were weighed on a digital scale. To this organic salt, calculated volumes of the inorganic precursor were pipetted and added. The mixture of the organic and inorganic salts were shaken for preparation of a uniform dispersion and this dispersion was then utilized as a precursor.

Thin film fabrication

The entire procedure was carried out in a nitrogen filled glove box or custom analytical cell. Thin films of perovskite crystals were developed by loading the glass substrates covered with mesoporous titania with 150 µL of the previously prepared precursor solution. The precursor was allowed to infiltrate the pores by allowing a standing time of 15 s before the spinning protocol was initiated. The film was subject to a 2 step spinning process, the first was at 100 rpm for 10 s, followed by 3000 rpm for 30 s. 15 s prior to the end of the spinning process, 150 µL of chlorobenzene was dispensed onto the spinning substrate in a smooth go. Chlorobenzene is a halogenated solvent which is miscible with the solvents employed, but insoluble with the perovskite itself. The chlorobenzene leads to instant initiation of crystallization by removing the organic solvents from the film. At this state, the film is recognized to exist in an intermediate phase, in a matrix of the organic and inorganic components with some residual solvents as a solvent complex. The intermediate solvent complex phase is then converted to the perovskite phase by annealing the films at 100°C for 5-10 minutes. Some perovskite systems like $FAPbI_3$ required higher annealing temperatures (140°C) due to their higher formation energies.

4 Semiconducting colloidal perovskite precursors

This chapter is based on the publication
”Emergence of lead halide perovskite colloidal dispersions through aggregation and fragmentation: insights from the nanoscale to the mesoscale”
S. Pratap, E. Keller and P. Müller-Buschbaum, *Nanoscale* **2019**, 11, 3495-3499; DOI: 10.1039/C8NR09853K.

Introduction

Perovskite materials are solution processed from colloidal precursors which have multivariate, tunable characteristics properties. The ease of solution tunability of perovskite chemical compositions and their various structural identities have enabled extensive research and commercialization efforts into structuring the material for a wide range of applications, in its various states of assembly. The entire range of solution-processed structures, extending from nanocrystals, to thin films and to single crystals share innocuous property of the precursors, namely their colloidal state [39, 41, 59–61].

The colloidal nature of the precursor imparts intensive degrees of freedom to the fluid sol state, which deviate from properties of true solutions. Moreover, the precursors are known to be dynamic and strongly affected by processing parameters and in turn impact the resulting thin film morphologies [20, 62]. The colloidal nature itself emerges due to the non-trivial, physico-chemical interactions [63] between the dispersed solid precursors and the solvent media (Figure **??**). Despite the existing knowledge about mechanisms of nucleation and growth of nanoparticles, [64] it remains imperative to understand the structure of the colloids in the fluid phase, in order to obtain predictive correlation between initial precursor chemistry and the final thin film morphology of hybrid perovskites. To this end, the structural and optoelectronic properties of mixed halide perovskite colloidal precursor dispersions of $MAPbBr_3$, $MAPbI_3$ and a 1:1 mixture of $MAPbBr_3$ and $MAPbI_3$ to afford $MAPbBr_{1.50}I_{1.50}$ are investigated. Comprehensive optical spectroscopic UV-vis measurements and DLS measurements are used to measure and characterize the properties of colloidal precursors which are used for fabricating thin films.

4.1 Visualizing the colloidal nature of precursors

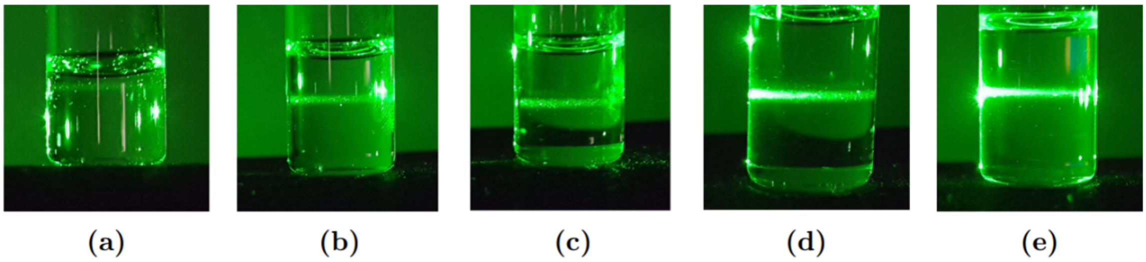
(a) (b) (c) (d) (e)

Figure 4.1: Tyndall cone created by a green laser pointer for a) 4:1 DMF:DMSO b) 0.5 M $MAPbBr_3$ c) 1M $MAPbBr_3$ d) 2M $MAPbBr_3$ and e) 3 M $MAPbBr_3$ each dispersed in a 4:1 DMF:DMSO solvent medium [65].

Before conducting advanced experiments on the precursors, their colloidal nature was tested by visualizing Tyndall cones of scattering. The experiment was conducted in the dark for visualizing the scattering from colloids clearly. The experiment was conducted on the basis of the phenomenon of light scattering by particles dispersed within a medium when particles within the medium are sized roughly in the range of the wavelength of light. Notably, true solutions of well intermixed and dissolved solutes in solvents (or more generally, any dispersed state in a medium) do not exhibit the Tyndall effect. For a colloidal medium, light cannot pass unobstructed and therefore undergoes scattering leading to a visible cone. For visualizing the colloidal nature of samples, dispersions of the precursor were sampled at different concentrations levels and a laser beam was incident upon the samples individually. (Figure 4.1)

A 532 nm laser was incident each on samples of the pure solvent medium of 4:1 DMF:DMSO in which all samples were prepared (Figure 4.1 a). Samples included a 0.5 M dispersion of $MAPbBr_3$ (Figure 4.1 b), a 1 M (Figure 4.1 c), 2 M (Figure 4.1 d) and 3 M dispersion of $MAPbBr_3$ in 4:1 DMF:DMSO. The Tyndall effect was observed for all the $MAPbBr_3$ samples. Notably, samples with higher concentrations displayed a more prominent scattering cone as compared to samples with a lower concentration. Such trends in behaviour were attributed to the higher complexation and larger sizes of the colloids causing higher scattering. Deeper insights into the change in behaviour of colloids with concentration required more detailed UV-vis and DLS measurements.

4.2 Evolution of optoelectronic properties of $MAPbBr_3$

Foremost, the optical properties of precursor sols are studied by UV-vis measurements. In the UV-vis measurements, the absorbance of $MAPbBr_3$ dispersions was measured in the visible region of the spectrum and corrected against the background of the solvents used. Measurements below 300 nm were not conducted due to the interference by atmospheric parameters such as oxygen, water vapour etc. A series of concentrations for the precursors are utilized in order to decohere the effects and mark the boundaries of changes within colloid structure by the aggregation and fracture of entities within the fluid phase. A stock solution of an exemplary concentration has been prepared and is then sequentially diluted in order to obtain lower concentrations of interest.

The samples are measured against a blank of the solvent mixture of 4:1 of DMF : DMSO, in which the precursors have been dispersed. The first sol investigated is a dispersion of the precursors of $CH_3NH_3PbBr_3$ (CH_3NH_3Br + $PbBr_2$ in 4:1 DMF:DMSO) for which a stock solution of 3 M was prepared. The absorbance properties of the 3 M and subsequent lower concentration precursors are measured sequentially, in order to regulate similar physical and atmospheric conditions (Figure 4.2).

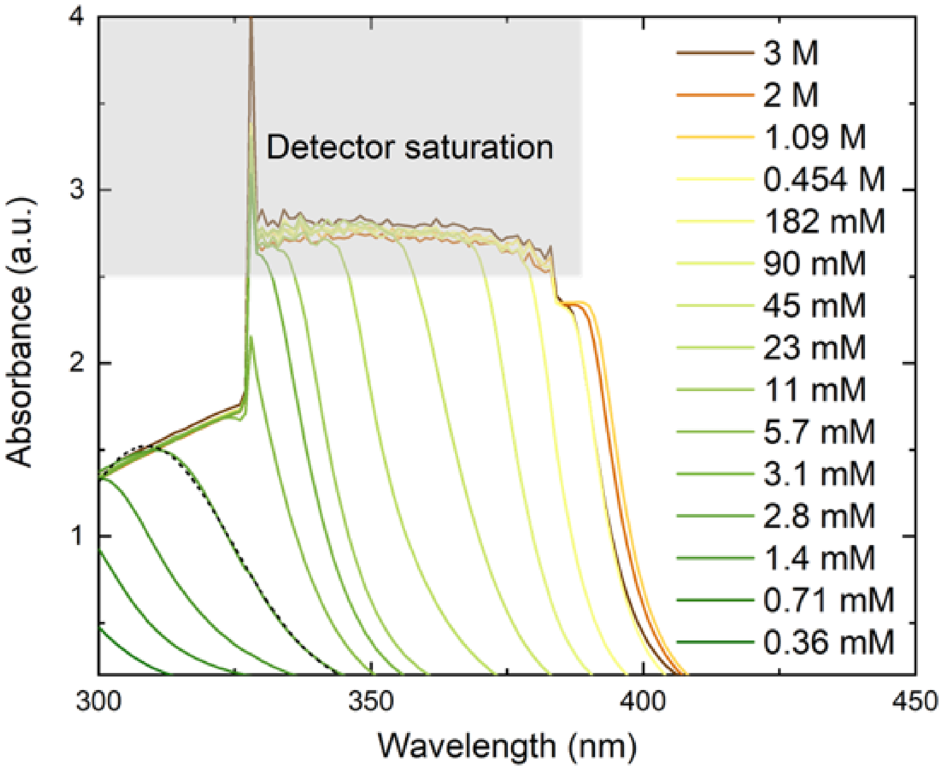

Figure 4.2: Overview of UV-vis absorbance data of aliquots of $MAPbBr_3$ precursor in a 4:1 DMF:DMSO solvent system, at concentrations obtained by sequential dilution of a stock solution (3 M) $MAPbBr_3$ precursor. Data show large red shifts in absorption edges of dilute colloidal precursors in range from 0.36 mM to 0.45 M. Absorption edges at large concentrations are found to be similar. Reprinted from [18] with permission from the Royal Society of Chemistry.

The data showed the absorption profiles for the optically transparent colloidal precursors in the blue regime of the electromagnetic spectrum. Reflecting sharp absorption onsets for the precursors, the data showed strong absorbance characteristics for the samples. With dilution of the sample, the overall trend showed distinct changes in the absorption onsets, especially when low concentrations were reached.

The overall absorbance data suggest the presence of two distinct (and three identifiable) structural regimes (Figure 4.3). For precursors of high concentrations ranging from 3 M to around 1.3 M, the dispersions all display similar absorbance

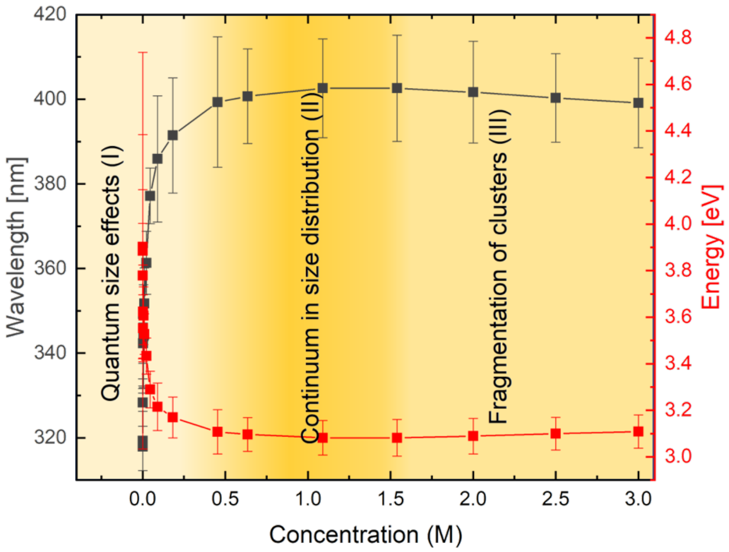

Figure 4.3: Evolution of optical properties of MAPbBr$_3$ precursor with changing concentration by sequential dilution. Data represent the change in the absorption onsets of samples as a function of concentration of the sample. Differences arise due to change in size of colloidal entities within 3 representative structural growth regimes with changing concentration. Reprinted from [18] with permission from the Royal Society of Chemistry.

profiles with absorption onsets around 405 nm. The absorption onsets of precursors of concentrations in this high concentration regime (Figure 4.3; III), appear slightly red-shifted with each dilution (Figure 4.4). From 1.3 M until 0.45 M (regime II), the precursors express stabilized structural sizes wherein the absorbance characteristics remain predominantly invariant with decreasing concentration with minor blue shifts with subsequent dilutions.

At concentrations below 0.45 M (regime III), the precursor sols show noteworthy blue-shifts in their absorption onsets with each dilution. Individual material absorbance peaks could not be resolved due to saturation at the detector at absorbance values around 2.5 wherein the maximum of the absorbance signal is lost due to its high magnitude, owing to the high absorption coefficient of the precursor. For a singular concentration of 2.8 mM, the absorbance maxima could be resolved by the detector, and a quasi-Gaussian profile of the absorbance peak is obtained (Figure 4.2).

Thereafter, the size distribution of particles in the precursor fluid is probed

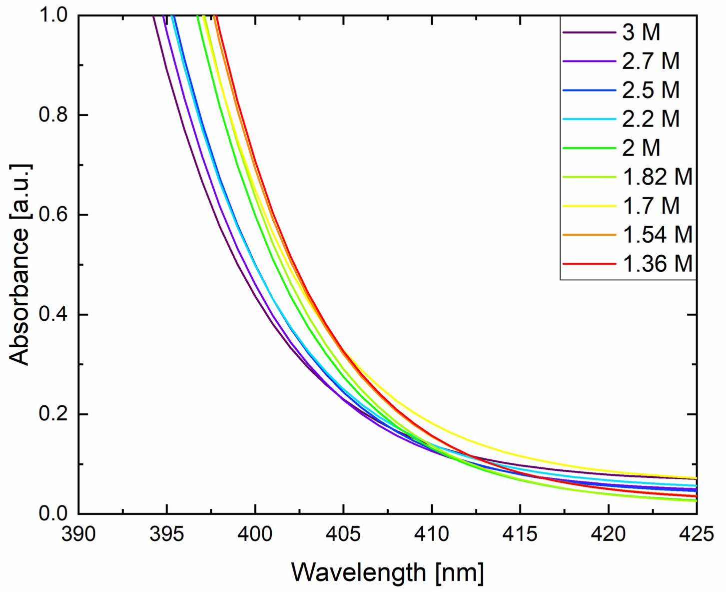

Figure 4.4: Absorbance data of $MAPbBr_3$ in high concentration range (regime III) displaying a red shift in the absorption edge with increasing dilution. Data suggest an increase in the size of absorbing colloidal particle with sequential dilution in regime III. Reprinted from [18] with permission from The Royal Society of Chemistry.

through DLS measurements for $MAPbBr_3$ at concentrations ranging from 3 M down to 0.1 M. The auto-correlation function exhibited two distinct decay timescales suggesting two discernible structure distributions of scattering objects (Figure 4.5). The first decay corresponds to hydrodynamic radii of structures within the nm range (Figure 4.6) and the second decay exhibits hydrodynamic radii of structures within the µm range (Figure 4.7).

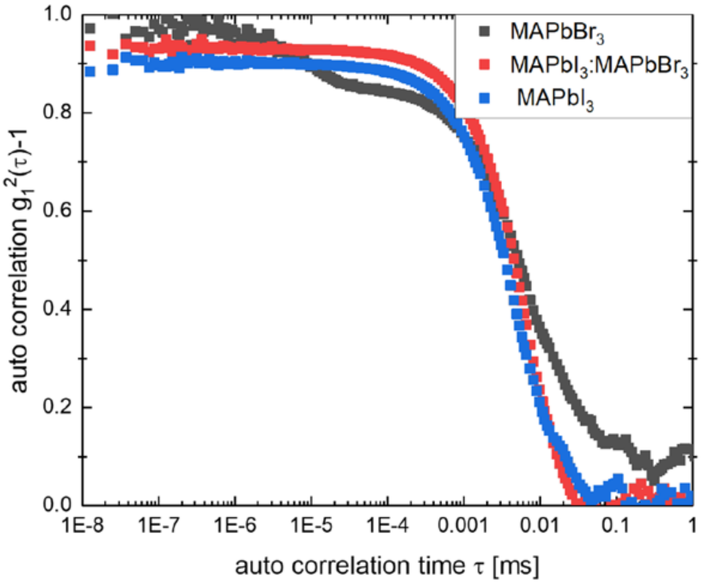

Figure 4.5: Auto-correlation functions exhibiting the decay times for precursors of 1M $\mathrm{MAPbBr_3}$ (grey), $\mathrm{MAPbI_3}$ (blue) and $\mathrm{MAPbI_{1.50}Br_{1.50}}$. $\mathrm{MAPbBr_3}$ exhibits two distinct decays signifying the presence of two structural size regimes discernible by DLS. Reprinted from [18] with permission from The Royal Society of Chemistry.

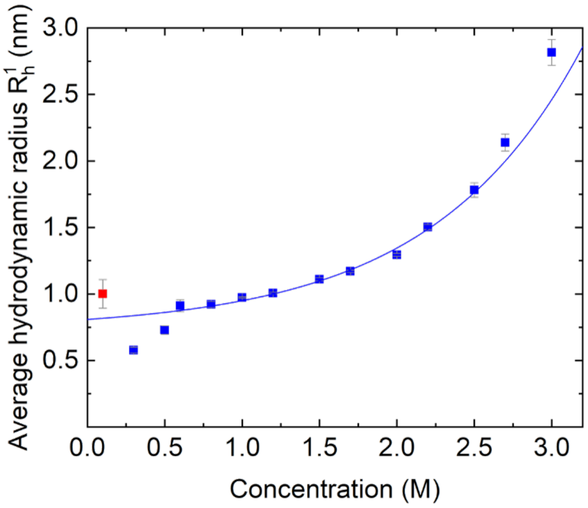

Figure 4.6: Hydrodynamic radii of $\mathrm{MAPbBr_3}$ nanoparticles ontained from DLS data (small structures) evolving with increasing concentration. The structures represent a sequential increase in the sizes detected. Red point signifies the smallest concentration reached within DLS experiments by dilution. Reprinted from [18] with permission from the Royal Society of Chemistry.

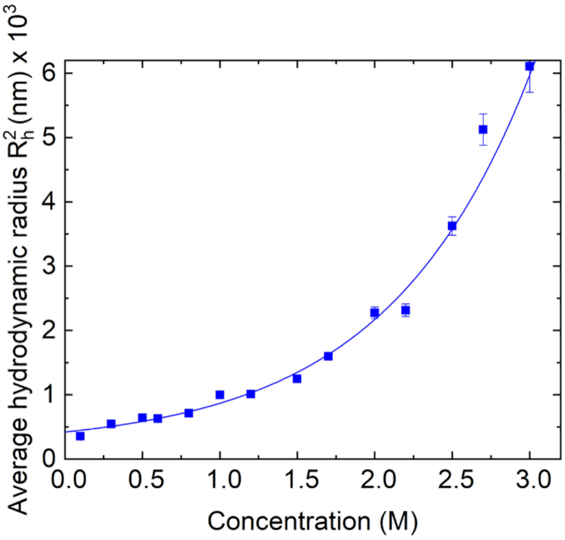

Figure 4.7: Hydrodynamic radii of $MAPbBr_3$ clusters (large structures) evolving with increasing concentration. Structures represent a continuous increase in sizes of scattering entitites as a function of concentration. Reprinted from [18] with permission from the Royal Society of Chemistry.

4.3 Evolution of optoelectronic properties of $MAPbI_3$ and $MAPbI_{1.50}Br_{1.50}$

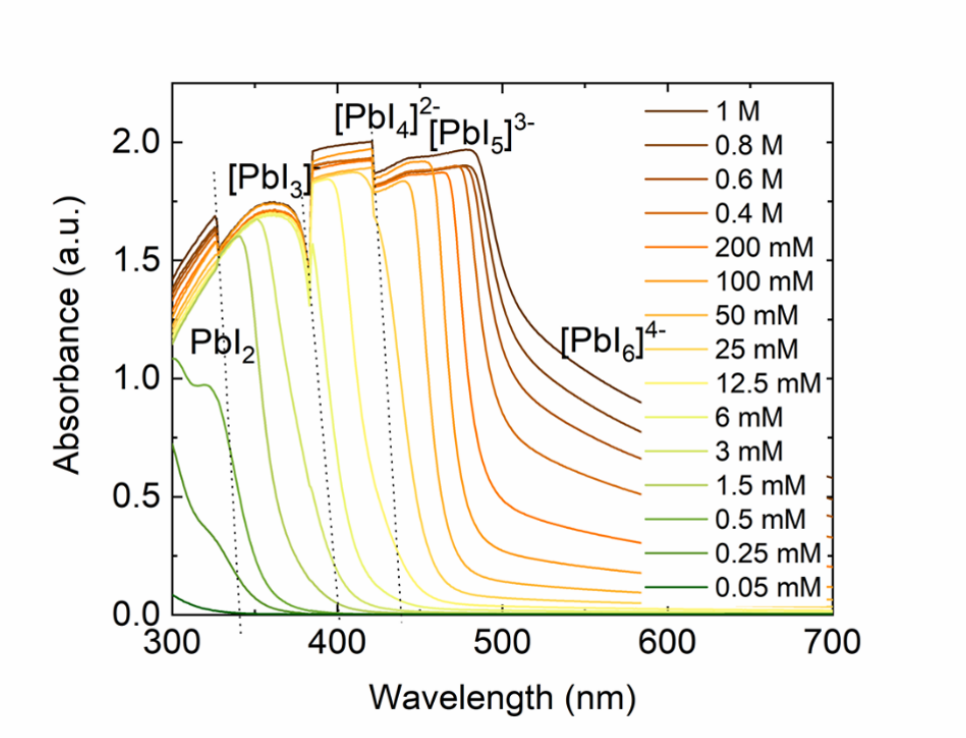

Figure 4.8: Overview of UV-vis absorbance data of aliquots of $MAPbI_3$ precursor in a 4:1 DMF:DMSO solvent system, at concentrations obtained by sequential dilution of a stock solution (1M) $MAPbI_3$ precursor. Data show rich optical signatures and sharp absorption edges from co-ordinated lead plumboiodide structural complexes with increasing concentration. Reprinted from [18] with permission from the Royal Society of Chemistry.

For the precursors corresponding to $MAPbI_3$, a stock solution of 1M was prepared. A higher concentration is not intended for the stock solution since the fluid precursor quickly turned translucent due to high supersaturation and the growth of large clusters threatened the integrity of measurements. The absorbance data is non-trivial and what at first glance appears as measurement artefacts are in fact, rich optical signatures from plumbo-iodate complexes (Figure 4.8), as confirmed by multiple sets of measurements.

Individual absorbance signals [66] are isolated from PbI_2 at around 340 nm; for

$[PbI_3]^-$ at 400 nm; for $[PbI_4]^{2-}$ at 438 nm and for $[PbI_5]^{3-}$ as well as $[PbI_6]^{4-}$ at more red shifted wavelengths. For $[PbI_5]^{3-}$ the absorption edge varied strongly with concentration. For $[PbI_6]^{4-}$, the absorption edge is not visualized.

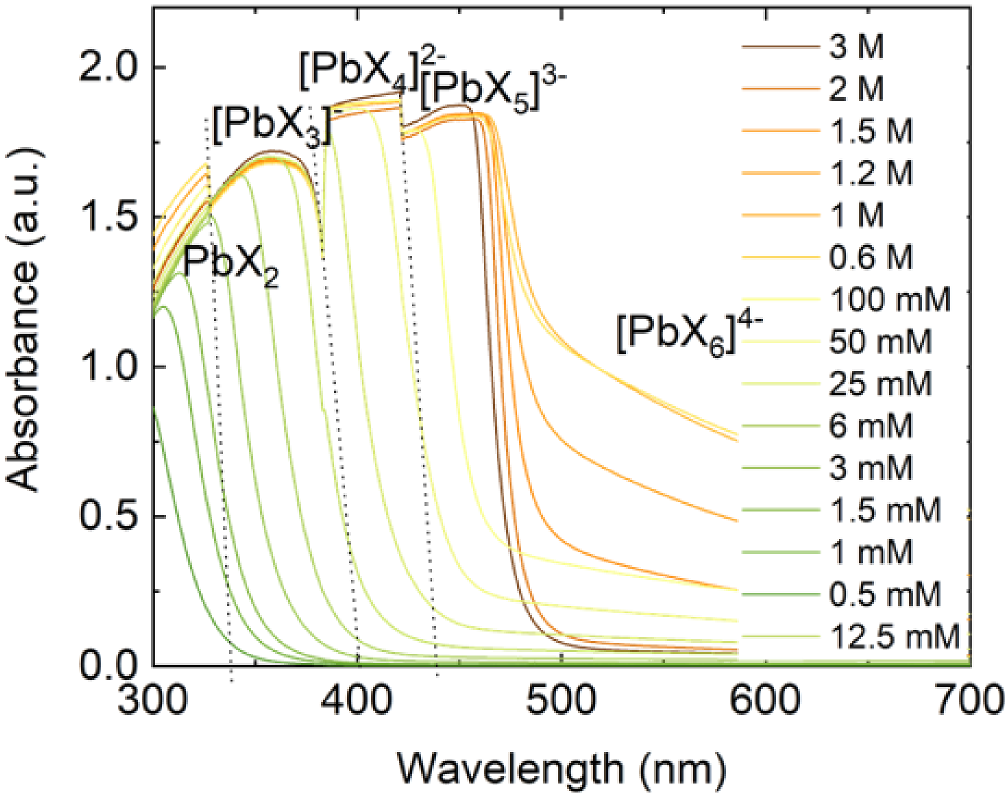

Figure 4.9: Overview of UV-vis absorbance data of aliquots of $MAPbI_{1.50}Br_{1.50}$ precursor in a 4:1 DMF:DMSO solvent system, at concentrations obtained by sequential dilution of a stock solution. Data show rich optical signatures and sharp absorption edges from coordinated lead plumboiodide structural complexes with increasing concentration. Reprinted from [18] with permission from the Royal Society of Chemistry.

It is striking to observe the identical signatures from the plumbo-iodate complexes within the precursor corresponding to $MAPbI_{1.50}Br_{1.50}$ at the exact wavelengths as designated for the complexes obtained from the $MAPbI_3$ precursor (Figure 4.9). Moreover, at concentrations beyond 1 M, the absorbance data of $MAPbI_{1.50}Br_{1.50}$ provides a rare and fascinating insight into the structure evolution of the concentrated fluid phase. It is observed that within the high concentration regime, the absorbance signal corresponding to $[PbI_6]^{4-}$ starts diminishing with increasing concentration and the absorption onsets experience a blue shift until 3 M (Figure 4.10).

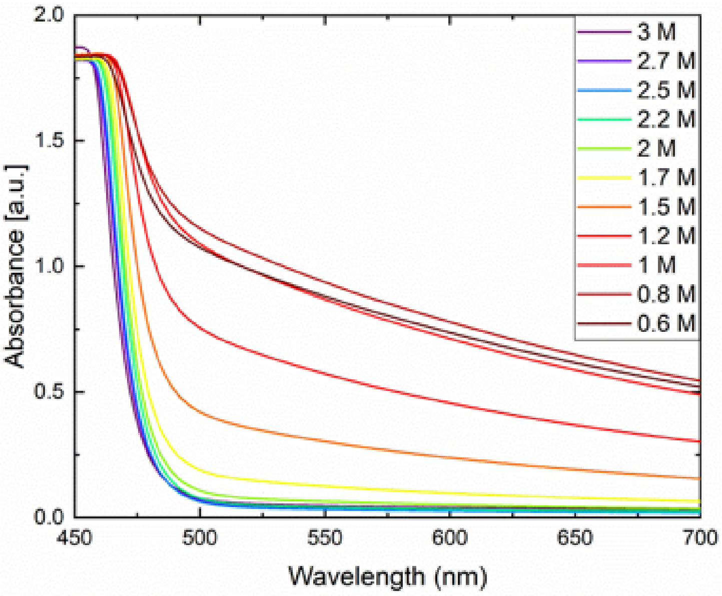

Figure 4.10: UV Vis data for $MAPbI_{1.50}Br_{1.50}$ in high concentration regime showing a red shift of the absorption tail and increasing background at high wavelengths with increasing dilution, the emergent spectroscopic signature from large plumbo-halide complexes. Reprinted from [18] with permission from the Royal Society of Chemistry.

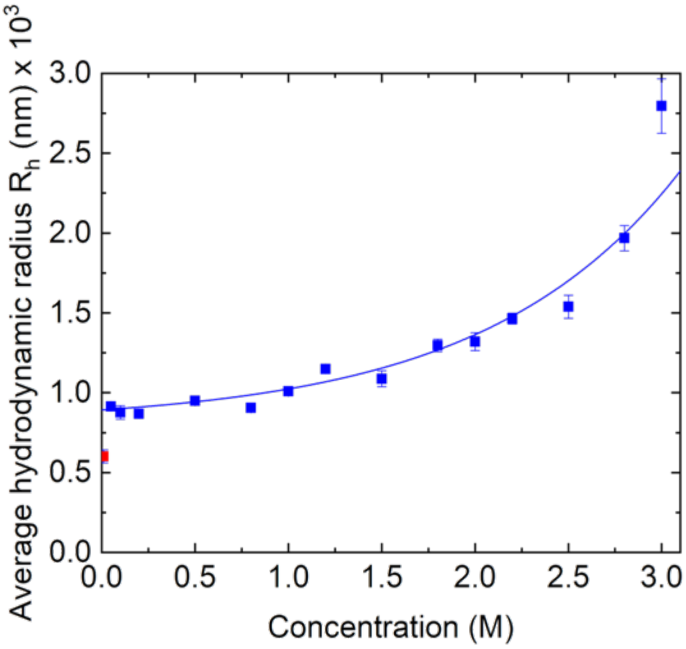

Figure 4.11: Hydrodynamic radii of MAPbI$_{1.50}$Br$_{1.50}$ nanoparticles obtained from clusters of colloidal particles formed by the combination of MAPbBr$_3$ and MAPbI$_3$. DLS data evolving with increasing concentration. The structures represent a sequential increase in the sizes detected. Red point signifies the smallest concentration reached within DLS experiments by dilution. Reprinted from [18] with permission from the Royal Society of Chemistry.

Table 4.1: DLS raw scattering intensities from colloidal precursors at 25°C. Reprinted from [18] with permission from The Royal Society of Chemistry.

Parameters	**$MAPbBr_3$**	**$MAPbI_{1.50}Br_{1.50}$**	**$MAPbI_3$**
Scattering intensity	170 kHz	430 kHz	440 kHz

Within DLS, unlike the case of $MAPbBr_3$ where 2 distinct decays were isolated and fitted to nanoparticles and larger clusters, in the case of both, $MAPbI_3$ and $MAPbI_{1.50}Br_{1.50}$, no clear distinctions for different structural size distributions could be made (Figure 4.4). The DLS data corresponding to $MAPbI_{1.50}Br_{1.50}$ (Figure 4.11) indicate hydrodynamic radii within the µm range, which show an exponential increase with increased concentration. The DLS data for $MAPbI_3$ (Figure 4.12) suggest the presence of smaller scattering objects which is however not indicative of the true nature of the fluid precursor.

This is evident from the raw scattering intensities of the different precursors: $I[MAPbI_3] > I[MAPbI_{1.50}Br_{1.50}] > I[MAPbBr_3]$

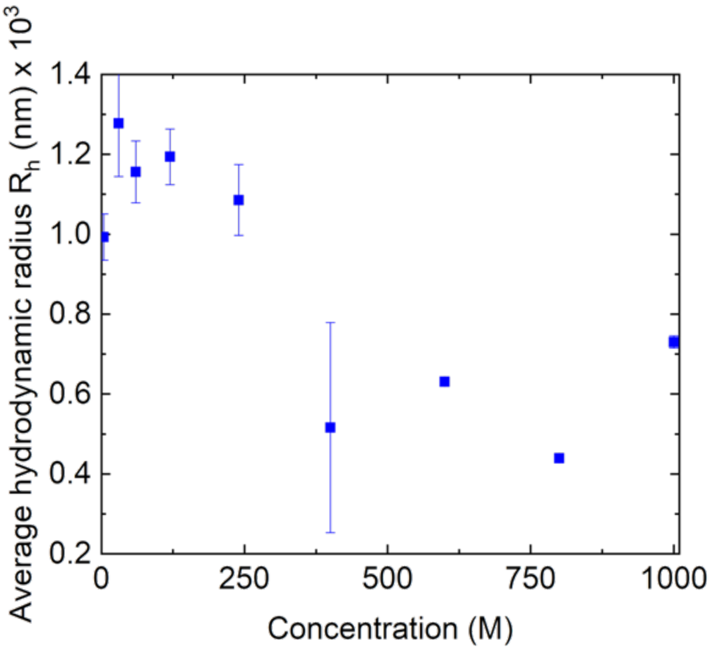

Figure 4.12: Hydrodynamic radii obtained from DLS data for MAPbI$_3$ showing varying sizes of clusters of colloidal particles. Reprinted from [18] with permission from the Royal Society of Chemistry.

4.4 Impact of precursor concentration on fluid physicochemical interactions

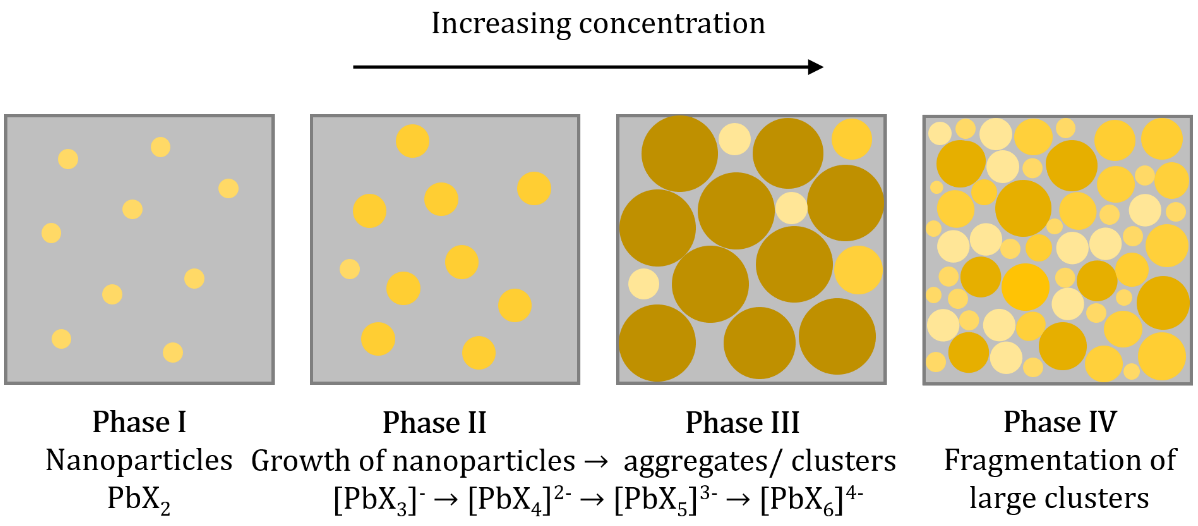

Figure 4.13: Schematic of the evolution of structures with increasing concentration: Starting from nanoparticles (phase I), followed by increasing size of nanoparticles (phase II), followed by the formation of large aggregates / complex clusters (phase III) until fragmentation of large aggregates (phase IV) occurs as a function of increasing volume fraction of the dispersed phase in the dispersion medium. Reprinted from [18] with permission from The Royal Society of Chemistry.

Colloidal precursors are complex species and as evident, are strongly affected by the chemical environment. (Figure 4.13) describes the fate [67, 68] of the colloidal dispersion as a function of increasing concentration of the precursor in the solvent media. At low volume fractions, the dispersed particles are small (nanoparticles) and experience quantum confinement effects. This behaviour is reflected through the red shifts within absorption profiles of growing structural entities as the concentration of the solute is increased within the dispersion. An increase in volume fraction favours the growth of small entities into larger clusters, rather than increased number of smaller individual particles [69]. As a result, higher order complexes (more relevant for I-containing precursors) or simply particles with increased size/ increased co-ordination emerge with increasing concentration [70, 71]. At any given volume fraction, the size/ structure of the dispersed phase/ solvent complex is limited by the concentration of the precursor. In this regime, growth/ structural evolution of nanoparticles is favoured as the dispersed entities have high degree of translational freedom which affords a larger volume available to the said entities for diffusion [72] because entropic considerations favour growth. The above growth processes fall under phase I and II of the above schematic. These phases also coincide with the quantum size regime observed in the UV-vis measurements and serve as the explanation as to the emergence of new spectroscopic signatures from higher order Pb-X complexes with increasing concentration. Growth of nanoparticles continues until a stable cluster size is obtained by the dispersed phase. This phase lasts within a concentration range wherein the size of the colloids remains primarily unchanged but the dispersion experiences an increase in packing density. Once a critical packing density is reached (which varies with chemical composition, owing to changing interactions of the dispersed chemical species with the dispersion medium), any further increase in the concentration of the dispersed phase leads to the jamming of the colloid (phase III) as the volume available to clusters for diffusion (excluded volume) is depleted. Further growth of particle size is no longer favoured due to increased repulsion between the densely packed colloid clusters as the system enters a non-ergodic regime [73] and the increased volume fraction of the precursors leads to a significant, nonlinear increase in the viscosity of the fluid marking a change in the rheology of the precursor [74] (Figure 4.14). The diffusion of the particles is arrested and the viscosity induced shear forces in addition to the steric frustrations experienced by the colloidal clusters lead to the fragmentation (or deaggregation) of the erstwhile stable, homeomorphic particles to form smaller, more numerous and dissimilar clusters (phase IV). This explains the blue shift of the absorption tails at high concentration. Moreover, it is the same phenomenon responsible for $MAPbI_{1.50}Br_{1.50}$ exhibiting drastically diminished spectroscopic signatures from the $[PbX_6]^{4-}$ complex, the largest of the various complexes expressed, within concentration regimes well within the supersaturation of the fluid phase. The boundaries between different growth regimes in different dispersions are variable and the sizes of particles at specific volume fractions are strongly sensitive to the distinct chemical environment and the physical characteristics of the liquid media.

It is worthwhile to note that the scattering intensity within DLS scales as r^6 with

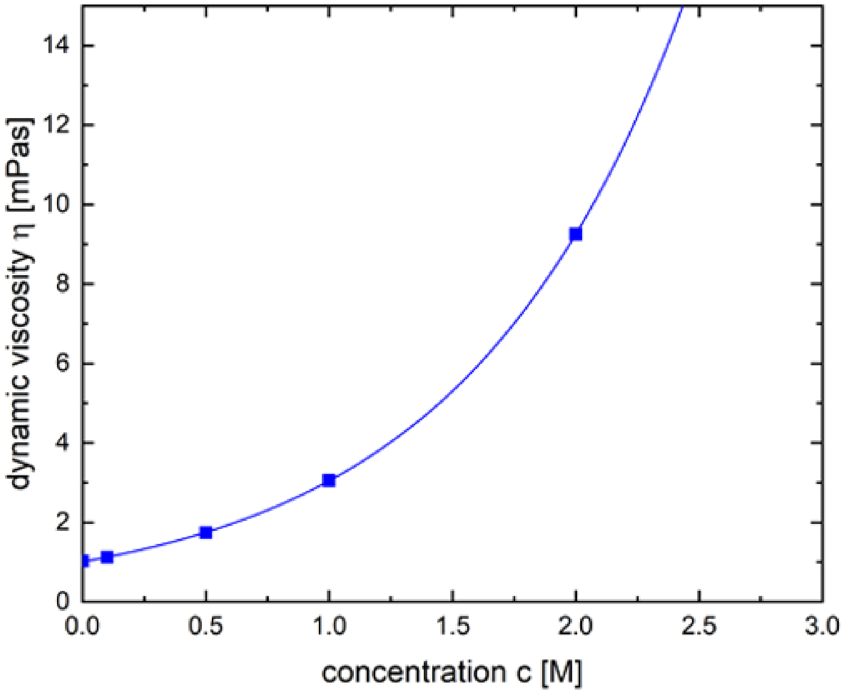

Figure 4.14: Evolution of viscosity of the $MAPbBr_3$ precursor fluid with increasing concentration showcasing the transition of a Newtonian fluid to a non-Newtonian fluid. Reprinted from [18] with permission from The Royal Society of Chemistry.

the particle radius (r). Thus, a particle 10 times the radius of another would scatter 10^6 stronger than the other. A distinct decay corresponding to small nanoparticles, as was the case for $MAPbBr_3$ would be indicative of a significant population of the colloidal precursors exhibiting the size within the nm regime, in order for the decay to even be sensitive to the measurement itself. This confirms the presence of distinctly polydisperse scattering objects as per DLS measurements.

Hydrodynamic radii obtained from the measurements overestimate the radius of the scattering particles. Moreover, for $MAPbBr_3$, each dilution leads to an increase in the excluded volume of the colloidal dispersion, providing the particles with an increased volume for diffusion. In the jammed state of the precursor, due to considerably increased viscosity, the packed clusters, in spite of a stabilized size, appear rather as a large scattering entity with slow diffusion timescales, which explains why the data affords extremely large hydrodynamic radii for $MAPbBr_3$.

For the I-bearing counterparts, due to the presence of a plethora of solvent complexes of distinct sizes and shapes, the polydispersity is manifold and more complex as compared to the relatively simple Br-bearing precursor. The DLS measurements for the $MAPbI_3$ dispersion is challenging to probe and the data and the trends are not truly representative, possibly due to Mie scattering from the large solvent complexes, which would require angle resolved DLS measurements to account for the anisotropic scattering. Perovskite precursors consist of structures possessing high flexibility. As a result, thin film morphologies are strongly affected by the rheology of the viscoelastic precursor sols.

4.5 Impact of precursor concentration on thin film crystallization

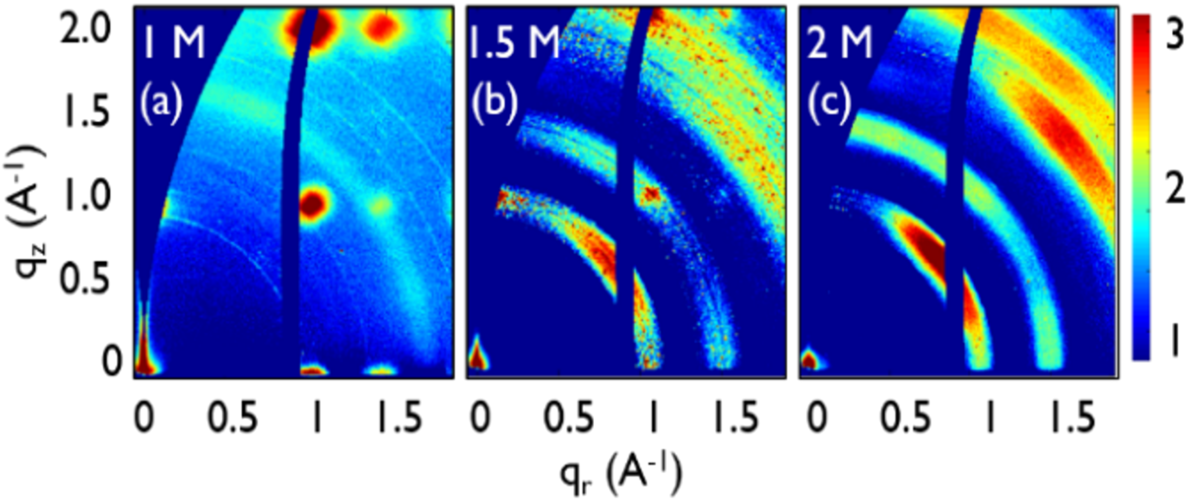

Figure 4.15: 2D GIWAXS data of $MAPbBr_3$ thin films prepared from indicated precursor concentrations: (a) 1M, (b) 1.5M and (c) 2M. Reprinted from [18] with permission from The Royal Society of Chemistry.

At nominal concentrations of the fluid precursor, crystallization is guided through thermodynamically controlled routes and thin films form such that the system settles into the minimal energy state, with high degree of morphological order Figure 4.15a and a state of minimum energy is attained by the emergence of 100 facets with a narrow azimuthal spread. At higher concentrations, the viscosity of the precursors sees an increase as dispersed particles obtain jammed characteristics while existing under entropic stress. The high volume fraction of the dispersed precursors drives the fluid well into supersaturation and resultant thin films are formed by kinetic arrest of the precursor, as crystal growth occurs through stochastic routes, far-off from thermodynamic equilibrium. Thin films formed from such precursors exhibit reduced microstructural homogeneity, as kinetically guided crystallographic directions emerge 111 with broad azimuthal spreads (Figure 4.15c).

4.6 Summary

Precursors of $MAPbBr_3$, $MAPbI_3$ and $MAPbI_{1.50}Br_{1.50}$ contain a dispersion of the organic and inorganic phase within the solvent. On varying their concentrations, optoelectronic signatures of plumbohalide solvent complexes are visualized. The co-ordination extent of the complexes alters with changing concentration and higher concentrations display increased co-ordination. The viscosity of the precursor is affected on changing concentration and this impacts the morphology of thin films fabricated thereof. Kinetically arrested orientations and structures are found emergent from higher concentration precursors whereas thermodynamic orientations are found emergent from precursors of lower concentration.

5 Hybrid perovskite thin films

This chapter is based on the publication
”Hierarchical Structures from Nanocrystalline Colloidal Precursors within Hybrid Perovskite Thin Films : Implications for Photovoltaics”
S. Pratap, J. Schlipf, L. Bießmann and P. Müller-Buschbaum, *ACS Applied Nano Materials* **2020**, 12, 11701-11708;
DOI: 10.1021/acsanm.0c03000.

Introduction

Hybrid perovskite based systems have attracted high attention from the scientific community, especially for their exemplary performance in photovoltaic devices which was first demonstrated in the past decade [10]. Since then, the continued research and engineering efforts have led to the device efficiencies of perovskite solar cells witnessing record-breaking improvements in a short span of time, with the technology transcending conventional terrestrial domains and being successfully operated in space [75]. Together with their silicon counterparts, novel photovoltaic technologies project trends indicating the most inexpensive and depreciating technoeconomic [15] costs of generation of electric power in history [76]. Moreover, the breadth of utility of hybrid perovskites has been extended into a range of applications far beyond photovoltaics [77]. Such attention to hybrid perovskites is not only because of the myriad characteristics that make them a lucrative material for optoelectronic applications, [33, 78–81] but also because the system serves as a rich reservoir for investigating a range of unusual material properties [82–91]. Of these developments, a major share is attributed to the compositional engineering of hybrid perovskites to prepare novel chemical mixtures with tunable material properties. Particularly of interest is the facile solution preparation routes through which chemical tuning can be accomplished.

In this chapter, hybrid perovskites are chemically engineered by mixing of stoichiometric equivalents of liquid precursors and spin coating into thin films. Structural equivalents of three perovskite systems namely $MAPbBr_3$, $FAPbI_3$ and $MAPbI_3$ are combined into two categories of solid solutions. $MAPbBr_3$ and $MAPbI_3$ are combined to form $MAPb(Br_xI_{1-x})_3$ hybrid halide perovskite alloys. $MAPbBr_3$ and $FAPbI_3$ are combined to form $(MAPbBr_3)_x(FAPbI_3)_{1-x}$ hybrid mixed perovskite alloys. By thermal annealing, the mixtures of perovskite compositions are intermixed and the optical, structural and morphological properties are investigated by UV-vis, XRD, SEM and GIWAXS respectively. Such alloyed perovskite structures are useful for engineering band gaps, structural and morphological properties of perovskite structures.

5.1 Structural solid solutions of hybrid perovskites

Perovskite based systems have the advantage of the capability of forming crystallographic frameworks combining organic and inorganic chemical entities. By the chemical combination of individual perovskite compositions, it is also possible to produce hybrid systems wherein the individual components react with each other at an atomistic scale in order to give rise to alloys [92]. Structurally, the individual chemical components share similar characteristics with deviations in elemental and resultant size and electronic properties [9, 26]. A wide range of intermittent compositions are accessible by stoichiometric design and facile solution processing within suitable solvent systems [93]. Distinct from physical mixtures, solid solutions reflect unique physicochemical properties, and often give rise to distinctive tunable structural and mechanical characteristics on mixing. The structures of the resultant compounds are verified by x-ray diffraction. It is notable that all mixture ratios lead to a novel structure, distinct from their precursors or pure perovskite species. By means of the peak position of the bragg reflexes, it is possible to calculate the unit cell dimensions of the perovskite structures. For perovskite ABY_3 based systems, alloying was demonstrated by two means; mixing of anionic species (hybrid halide perovskite alloys) $AB(Y_xY'_{1-x})_3$ and by mixing both cationic and anionic species (hybrid mixed perovskite alloys) $(A_xA'_{1-x})B(Y_xY'_{1-x})_3$.

5.1.1 Hybrid halide perovskite alloys

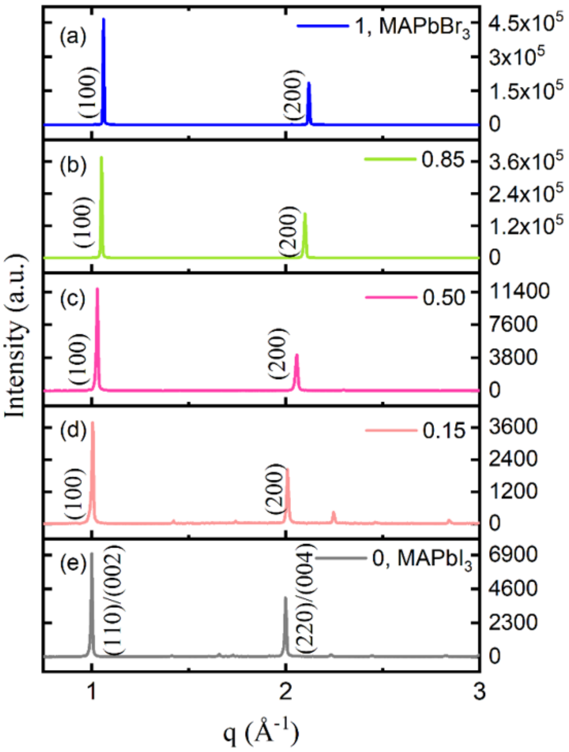

Figure 5.1: X-ray diffraction patterns for $MAPb(Br_xI_{1-x})_3$ for x = 1, 0.85, 0.50, 0.15, 0. $MAPbBr_3$ displays a cubic structure. x = 0.85, 0.50, 0.15 display pseudo-cubic diffraction structures. $MAPbI_3$ crystallizes in a tetragonal form. Adapted from [20] with permission from American Chemical Society, copyright 2020

The solid solutions are formulated by combining the stoichiometric equivalents of parent precursors of $MAPbBr_3$ and $MAPbI_3$ in suitable solvents and fabricating thin films by annealing. Every compositions exhibits unique structural features (Table 5.1) with distinct Bragg reflections from their parent compounds. The absence of Bragg peaks from the parent compounds, and the distinctive lattice spacings signify the presence of thermodynamically alloyed structures rather than physical mixtures. The compounds $\mathrm{MAPb(Br}_x\mathrm{I}_{1-x})_3$ exhibit a pseudo-cubic structural symmetry in their diffraction patterns for $x \neq 0$ (Figure 5.1.1). For $x = 0$, $\mathrm{MAPbI_3}$, the diffraction pattern exhibits a tetragonal lattice structure with additional reflexes around q 1.6 Å^{-1} due to reduced structural symmetry compared to pseudo-cubic form [94].

Mixed halide perovskite thin films are produced by combining the inorganic precursors of Lead bromide and Lead iodide with the organic precursor Methylammonium bromide and Methylammonium iodide.

x $\mathrm{PbBr_2}$ + (1-x) $\mathrm{PbI_2}$ + x MABr +(1- x) MAI → $\mathrm{MAPb(Br}_x\mathrm{I}_{1-x})_3$

Generic perovskite structures are known to display three structural phases namely orthogonal, tetragonal and cubic forms, depending on conditions of temperature and pressure [95]. $\mathrm{MAPbI_3}$, at room temperature, and atmospheric pressure is known to exist in the tetragonal crystallographic structure, and above 327 K in the cubic crystallographic form. In the tetragonal structure, $\mathrm{MAPbI_3}$ deviates from the simplistic cubic structure with the Pb-I bond length about the c axis slightly elongated. The origin of the reduced symmetry is known to be merely steric in nature. The increased bond length causes the octahedral frame formed by the plumboidiode matrix to develop a slight tilt along the c-axis. The I atoms however maintain their corner-sharing connectivity [38].

5.1.2 Hybrid mixed perovskite alloys

By stoichiometric mixing of parents precursors corresponding to $\mathrm{MAPbBr_3}$ and $\mathrm{FAPbI_3}$ within suitable solvents, alloys of mixed perovskites are attained in Table 5.2

Mixed perovskites are formed by combining the inorganic precursors Lead bromide and Lead iodide with the organic precursors Methylammonium bromide and Formamidinium iodide.

x $\mathrm{PbBr_2}$ + (1-x) $\mathrm{PbI_2}$ + x MABr +(1-x) FAI → $(\mathrm{MAPbBr_3})_x(\mathrm{FAPbI_3})_{1-x}$

Table 5.1: Structural parameters of hybrid halide perovskite solid solutions. Parameters obtained from fitting of the (100) reflex position represented in Figure 5.1.1

Perovskite system $AB(Y_xY'_{1-x})_3$	**q spacing** $Å^{-1}$	**d spacing** Å	**Unit cell volume** $Å^3$
x = 1 $MAPbBr_3$	1.061	5.921	207.64
x = 0.85 $(MAPbBr_3)_{0.85}(MAPbI_3)_{0.15}$	1.051	5.978	213.66
x = 0.50 $(MAPbBr_3)_{0.50}(MAPbI_3)_{0.50}$	1.028	6.112	228.33
x = 0.15 $(MAPbBr_3)_{0.15}(MAPbI_3)_{0.85}$	1.004	6.258	245.10
x = 0 $MAPbI_3$	tetragonal 1.000	6.284	990

The alloys too exhibit unique structural parameters with Bragg peaks distinctive from parent compounds (Figure 5.2). All structures display diffraction signals concomitant with a pseudo-cubic structure. Compositions corresponding to x = 1, x = 0.85 display highly textured thin films as evident from the high intensities from the (100) and (200) lattice planes and the lack of intensity from other lattice planes. Films corresponding to x = 0.50, x = 0.15 (Figure 5.2 c,d) display significant strain within thin films and possible amorphous content contributing to a broad background due to chemical and structural entropy. All mixed systems show distinct diffraction peaks, suggesting that the materials are crystalline. As expected from the ionic radii of their constituents, there is a distinct trend in the q-values of the perovskite systems. $FAPbI_3$ has a larger d-spacing, owing to the larger radii of I (2.2 Å) and FA (2.1 Å), as compared to $MAPbBr_3$ whose constituents are the smaller Br (1.96 Å) and MA (1.8 Å). The trend was in accordance with Vegard's law [96] that necessitates that at a given temperature, the lattice parameter of a solid solution follows the given rule

$$a_{A_{(1-x)}B_{(x)}} = (1-x)\ a_A + (x)\ a_B, \tag{5.1}$$

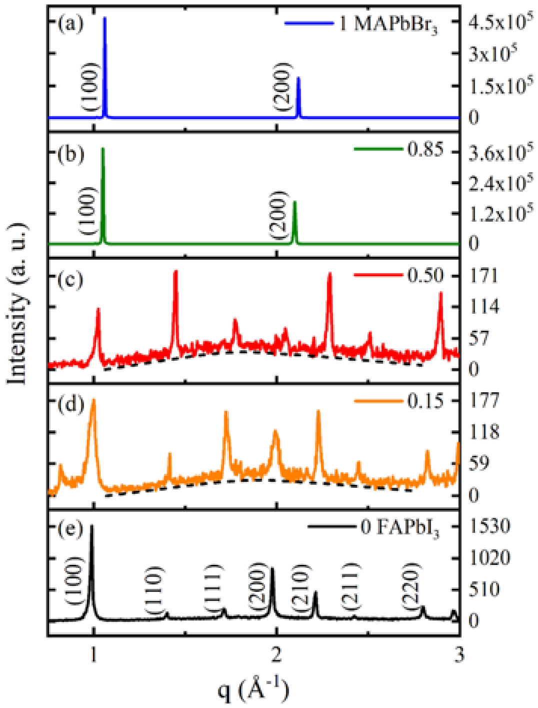

Figure 5.2: Structural hybrids combining MAPbBr$_3$ and FAPbI$_3$ within alloyed crystalline frameworks (MAPbBr$_3$)$_x$(FAPbI$_3$)$_{1-x}$ for x = 1, 0.85, 0.50, 0.15, 0. Adapted from [20] with permission from American Chemical Society, copyright 2020

where $a_{A_{(1-x)}B_{(x)}}$: lattice parameter of the alloy a_A, a_B : lattice parameters of the pure constituents x : percentage composition of B.

Notably, lattice strain are expected to manifest within thin films as a result of thermodynamic considerations, which may result in deviation of lattice parameters from expected trends. For a given iodide composition, mixed perovskite based systems display higher lattice parameters than mixed halide systems due to the size difference between MA and FA radicals, with FA ionic radius being larger than MA.

Table 5.2: Structural parameters of hybrid mixed perovskite solid solutions. Parameters obtained from fitting of the (100) reflex position represented in Figure 5.2

Perovskite system $(A_xA'_{1-x})B(Y_xY'_{1-x})_3$	**q spacing** Å^{-1}	**d spacing** Å	**Unit cell volume** Å^3
x = 1 $MAPbBr_3$	1.061	5.921	207.64
x = 0.85 $(MAPbBr_3)_{0.85}(FAPbI_3)_{0.15}$	1.051	5.978	213.66
x = 0.50 $(MAPbBr_3)_{0.50}(FAPbI_3)_{0.50}$	1.019	6.161	233.89
x = 0.15 $(MAPbBr_3)_{0.15}(FAPbI_3)_{0.85}$	0.991	6.341	255.02
x = 0 $FAPbI_3$	0.988	6.361	257.39

5.2 Band gap tuning of hybrid perovskites

Alongside the advantage of the ability to form solid solutions and unique lattice parameters, hybrid perovskites with chemical engineering can be tuned for their bandgaps [97] through the visible and NIR electromagnetic spectrum, which has advantageous implications for optoelectronic applications. In an ABX_3 system, the bandgap of materials increases with an increase of the electronegativity of the constituent species, while it reduces with an increase of the lattice constants of the system. Moreover, for the same material existing in different crystallographic structures, the polymorph bearing lower symmetries usually shows larger band gaps: E_g (tetragonal) $>$ E_g (cubic) [26]. To investigate the optical properties of mixed halide perovskites, firstly methylammonium lead halide anionic alloys were investigated. The anions were varied between different percentages of iodide and bromide. The intermediates were formed with precursor solutions with targeted desired compositions. The precursor solutions were made in a manner to prevent formation of individual perovskites. This was achieved by separate mixing of the inorganic components in the solvent media, to which the organic components were

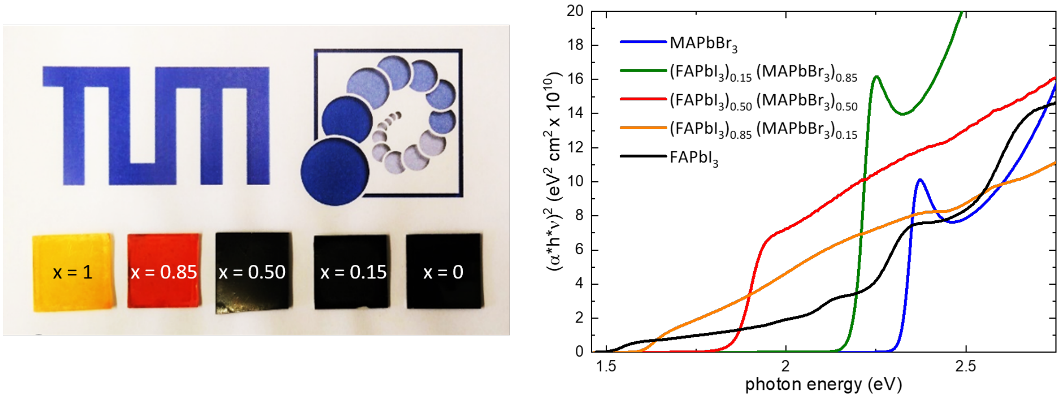

Figure 5.3: Juxtaposition of colorful thin films of hybrid perovskites (MAPbBr$_3$)$_x$(FAPbI$_3$)$_{1-x}$ with increasing iodide content from left to right, demonstrating band gap tunability through the visible and NIR electromagnetic spectrum.

later added to yield a saturated precursor solution. This precursor solution was then deposited onto a substrate and then spin coated to obtain a uniform thin film.

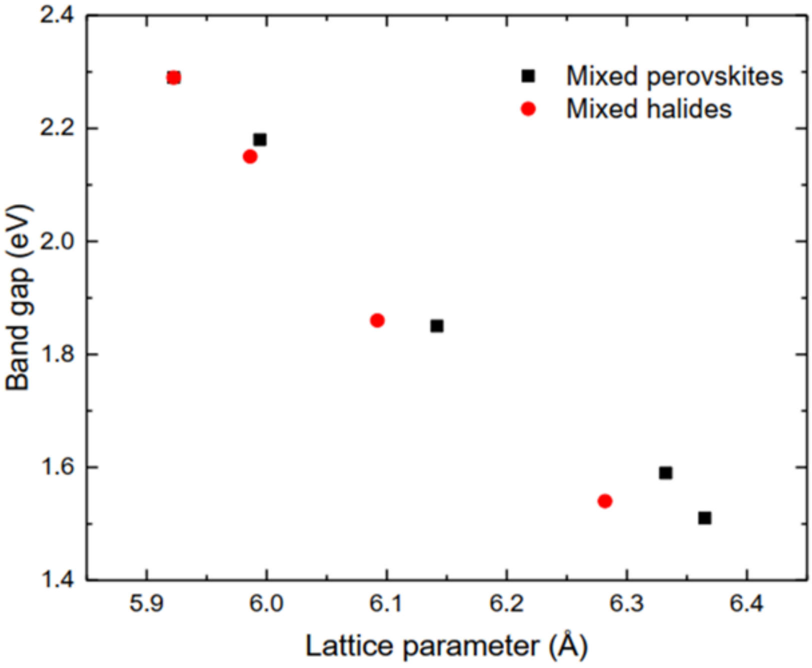

Figure 5.4: Variation of band gaps of mixed perovskite and mixed halide based systems with iodide (and bromide) content.

The onset of absorption in the Tauc plot is sharp (Figure 5.3), signifying a direct band-gap, which could be tuned by varying the composition resulting in colorful films. The colors ranged from light yellow for pure bromide to an increasingly darker hue, for a stark black iodide film. An evident red shift in absorption of the thin films on increasing the content of I is visible. This trend is attributed to the varying atomic radii of halides, and their electronegativities. I has lower electronegativity than Br, and a replacement of I by Br, makes the Pb-X bond longer, resulting in an increase in band gap. The cation has a lesser impact on the band gap of the perovskite mixtures and can modulate the band gap by modifying the lead-halide bond distance. Consequently, the shifts produced by substituting the organic cation are less pronounced than those produced by substitution of the halide. Band gap tunability arises ultimately due to both alloying effects and changes in the lattice constant. Figure 5.4 illustrates the linear relationship between the lattice constants of a perovskite system, and the corresponding band gap measured by UV-Vis spectroscopy. This observation too is in accordance with the Vegard's law which is applicable for the band gaps of solid solutions of semiconducting systems, wherein the band gap of a semiconductors' solid solution is approximately a linear function of the lattice parameter.

$$E_g A_{(1-x)} B_x = (1-x)\ E_g\ A + x\ E_g\ B \tag{5.2}$$

5.3 Emergence of hierarchical microstructures in thin films

The tunability of their material properties has been extensively explored and hybrid perovskites reflect a wide spectrum of functional and structural characteristics which arise from their versatile structure. This allows for the partial and/or complete chemical substitution within the crystallographic framework of the prototypical ABX_3 structure, forming solid solutions of a single perovskite phase. Consequently, the compositional engineering of perovskites has been established as common practice within the field for engineering materials with properties tuned toward specific optoelectronic parameters, such as band gaps, lattice parameters, charge carrier mobility and structural stability. One of the crucial consequences of compositionally tuning such hybrid systems is the impact on the film structure developed during crystallization.

The thin film deposition technique utilizes a complex mechanism wherein a number of chemical species react during a dynamic process. The inorganic perovskite precursors are dissolved in a mixed solvent phase, to which the organic counterpart of the desired perovskite are added and then spin coated onto a substrate. During the process, to enforce crystallization, an anti-solvent is dynamically dropped onto the spinning substrate to afford thin films. Irrespective of the production process, it is noteworthy that different perovskite films settle into different microstructures which are essentially kinetic instabilities occurring at different length scales.

Surface morphologies in perovskites are known to be affected by a number of factors, that range from the thin film deposition technique, the solvent system utilized, the precursors and additives utilized. Different morphologies of materials are known to exhibit varying physical properties. Thus it is worthwhile to note that one may control the required properties of a material by tuning its' morphology. Typically, phenomenon of wrinkling in natural systems such as aging skin, drying fruit and wet fingertips occur due to compression of thin films on a foundation. Wrinkles are a manifestation of mechanical instabilities in films caused by buckling, wherein an otherwise flat film develops out-of-plane undulations [98]. Such undulations are typically known to be regular, but they become spatially heterogeneous with increasing stress, eventually developing sharp, localized folds. There is a distinct wrinkle to fold transition observed in structures. Repetitive and successive wrinkle-to-fold transitions in a thin film are known to form hierarchical pattern of folds [99]. Folds are known to rearrange in time as their domains are mechanically linked. It is further known that such folds communicate and affect the growth and propagation of neighboring folds. Studies show that it is possible to have some control over the wrinkling pattern and morphologies by controlling certain boundary conditions. Hierarchical structures lead to texturing of thin films, which is beneficial for light trapping [81] in solar cells wherein a photon bounces back and forth within the layer multiple times, rather than escaping into the surroundings and is almost completely absorbed. This significantly reduces loss of light-generated carriers to recombination. Light trapping is usually achieved by changing the angle at which light travels in the solar cell by having it be incident on an angled surface. A textured surface also reduces reflection while coupling light into the solar cell, thus giving a longer optical path length than the physical film thickness.

5.3.1 Impact of hybrid perovskite chemical composition on thin film surface morphology

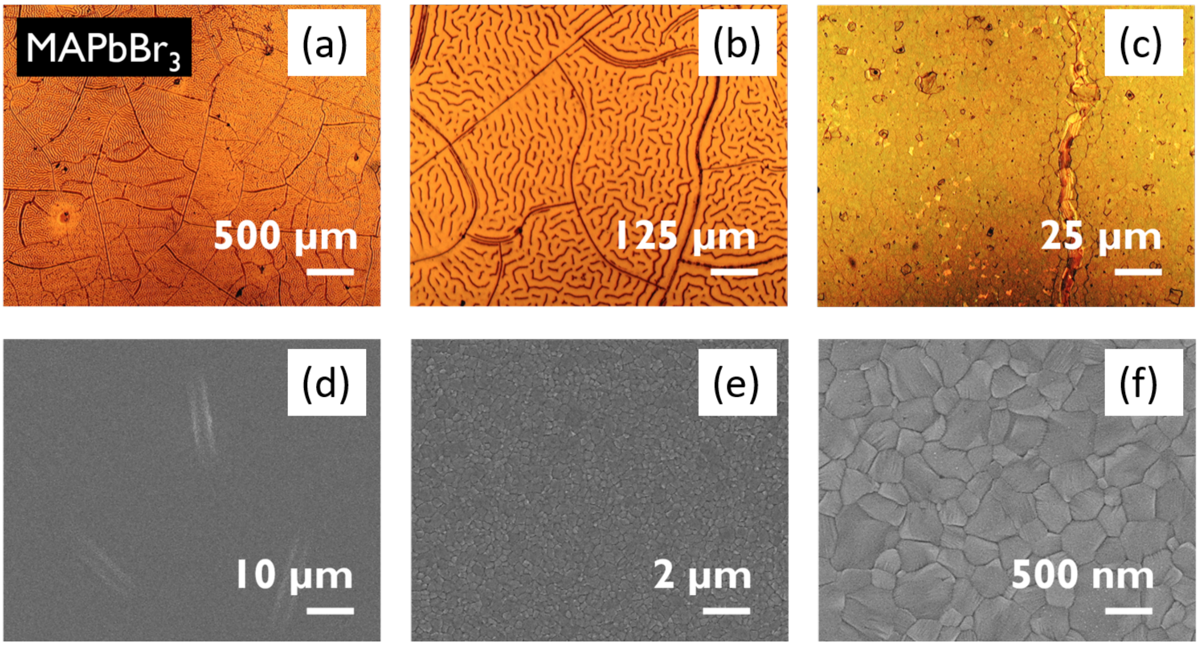

Figure 5.5: (a, b, c) Optical microscopy images and (d, e, f) Scanning electron microscopy images displaying morphological features of (x = 1) $MAPbBr_3$. OM showcases mud crack and worm-like features. SEM display compact, dense crystals.

The morphological variations within crystalline perovskite thin films have been demonstrated to be responsible for heterogeneities in the functional material response [100–103]. Such morphological inhomogeneities are a nominal consequence of one of the promises of perovskite manufacturing namely low temperature processing. The crystallization of the material is determined by a complex interplay of kinetic and thermodynamic processes as it occurs away from equilibrium, and causes the development and evolution of inherent microstructure within polycrystalline thin films [51]. The range of film microstructures is strongly affected by the chemical composition of the precursor. While many investigations explore routes of obtaining desirable morphologies, [104, 105] a fundamental understanding of the innate impact of chemical species within mixed composition on the nano- and mesoscale film structures and their implications for optoelectronic applications is imperative for further technological developments. Compositionally engineered fractions of distinct perovskite entities, $MAPbBr_3$ and $FAPbI_3$ are combined by mixing the desired stoichiometric equivalents of the inorganic and organic precursors within a common solvent system to afford colloidal nanocrystalline precursors [106]. The resultant precursors are spin coated following the one-step, anti-solvent assisted route of film formation [40] and are finally annealed into thin films with an exemplary composition of $(MAPbBr_3)_x(FAPbI_3)_{1-x}$. Notably, the fabrication route for all mixtures is maintained for direct comparison between different chemical compositions of perovskite precursors. To impose the avoidance of any epitaxial impact from a structured or planar substrate on the final film morphology, isotropic substrates of mesoporous nanocrystalline titania (30 nm) are used.

The first investigated film corresponds to the composition $MAPbBr_3$ (x = 1) . After spin coating, the film surface appears wrinkled to the naked eye. Optical microscopy (OM) data reveal two distinct type of structures, the first being reminiscent of drying cracks in mud (Figure 5.5) [107]. On closer inspection, these areas are found to be raised regions formed by the collision of disparate crystalline boundaries during grain growth. Apart from raised domain boundaries, parts within the crystalline island domains exhibit ‘worm-like’ undulations. Such undulations are sparse, and prevalent throughout the film, with varying length scales. Scanning electron microscopy (SEM) investigations too display these meandering ridges upon the film surface, which appear as slight wrinkles over the film surface. The crystals themselves are planar and contain nominal nanoscale morphological growth artefacts such as growth steps, towards the grain boundaries.

The next system which is investigated has a precursor composition corresponding to x = 0.85, or $(MAPbBr_3)_{0.85}(FAPbI_3)_{0.15}$. The microstructure of the film is dense and it exhibits a macroscopically rough, extensively folded film. OM and SEM data confirm the presence of a network of folds running over the entire film surface (Figure 5.6), unlike for the composition corresponding to x = 1, where short, disjointed folds within the film are observed. Locally, the folds themselves consist of smooth crystals at the surface. The film is distinctly polycrystalline, planar, compact and displays well-defined crystals with fairly monodisperse crystal sizes and distinct grain boundaries as observed by SEM. The undisturbed (flat) part of

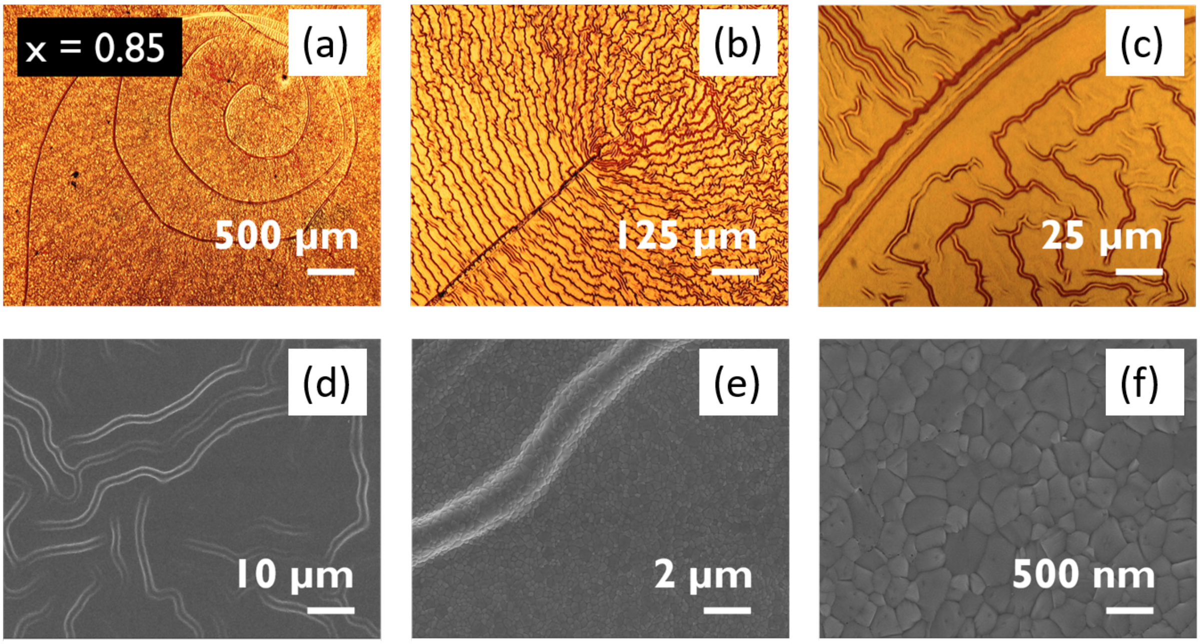

Figure 5.6: (a, b, c) Optical microscopy images and (d, e, f) Scanning electron microscopy images displaying morphological features of (x = 0.85) $(MAPbBr_3)_{0.85}(FAPbI_3)_{0.15}$ reflecting macroscopically rough, folded film. OM display dense network of folds and SEM displays compact, smooth crystals

the rest of the film and the morphology of the crystals of the smooth surfaces are predominantly indistinguishable from crystals forming the folds.

For x = 0.50, the density of folds see an increase, and there are no longer any macroscopic cracks observable on the film surface (Figure 5.7). Interestingly, the folds within the film are found to be interacting and the structures display self-organizing labyrinthine characteristics. This order at the macroscopic length scale is however compromised and locally, the crystals within the folds as well as within the flat film surface coarsen and the smooth, well-cut faces, which are visible for x = 1 and x = 0.85, are replaced by unshapely crystals. Thus, the morphology coarsens at local as well as macroscopic length scales, with rough, self-assembled folds within the thin film.

For x = 0.15, the folds as well as the cracks disappear and are replaced by a macroscopically smooth film with no visible undulations (Figure 5.8). The crystals themselves are smooth with a ‘striped’ surface with visible light and dark domains. The size of these dark and light domains are comparable within nano lengthscales.

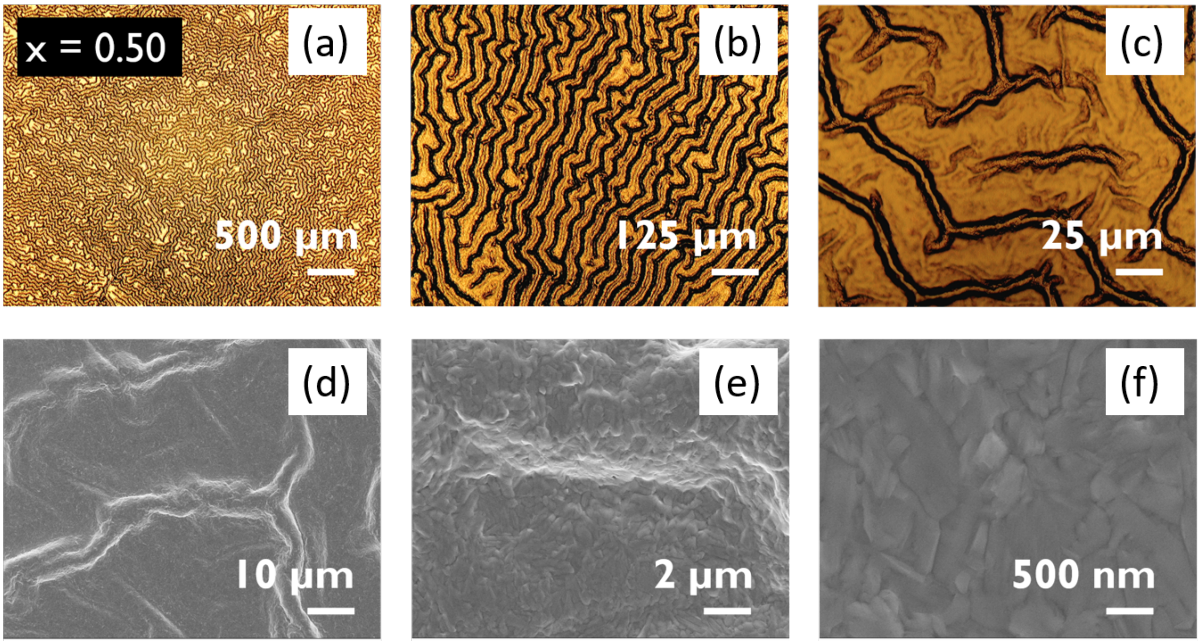

Figure 5.7: (a, b, c) Optical microscopy images and (d, e, f) Scanning electron microscopy images displaying morphological features of (x = 0.50) $(MAPbBr_3)_{0.50}(FAPbI_3)_{0.50}$. OM showcasing labyrinth of hierarchical self-organized folds. SEM display dense coarse folds and rough crystal facets

Their origin can be attributed to the presence of twinned domains [108,109] within the crystallized structure.

For $x = 0$, the well-studied $FAPbI_3$ is formed. This system shows interesting structures of the cubic and hexagonal phases, which are locally identified in different regions of the film. There are no folds or cracks visible upon the film surface. The crystals exhibit a rough surface morphology, while the crystal surfaces are structured with features such as growth steps and facets visible within the SEM images (Figure 5.9). A position within the film is locally found wherein a hole is present within the film and the crystalline material is not dense (Figure 5.10). Visibly, the film seems yellow around the hole, which suggests that the film has undergone degradation from the black, cubic α-phase to the yellow, hexagonal δ-phase polymorph of $FAPbI_3$. Intriguingly, optical microscopy images within these regions depict the presence of hexagon-shaped crystallites. These hexagonal masses are isolated within the film and observed through SEM as well. The sample when placed such that the yellow non-perovskite phase is intercepted by the beam path in XRD show strong signals from the δ-$FAPbI_3$.

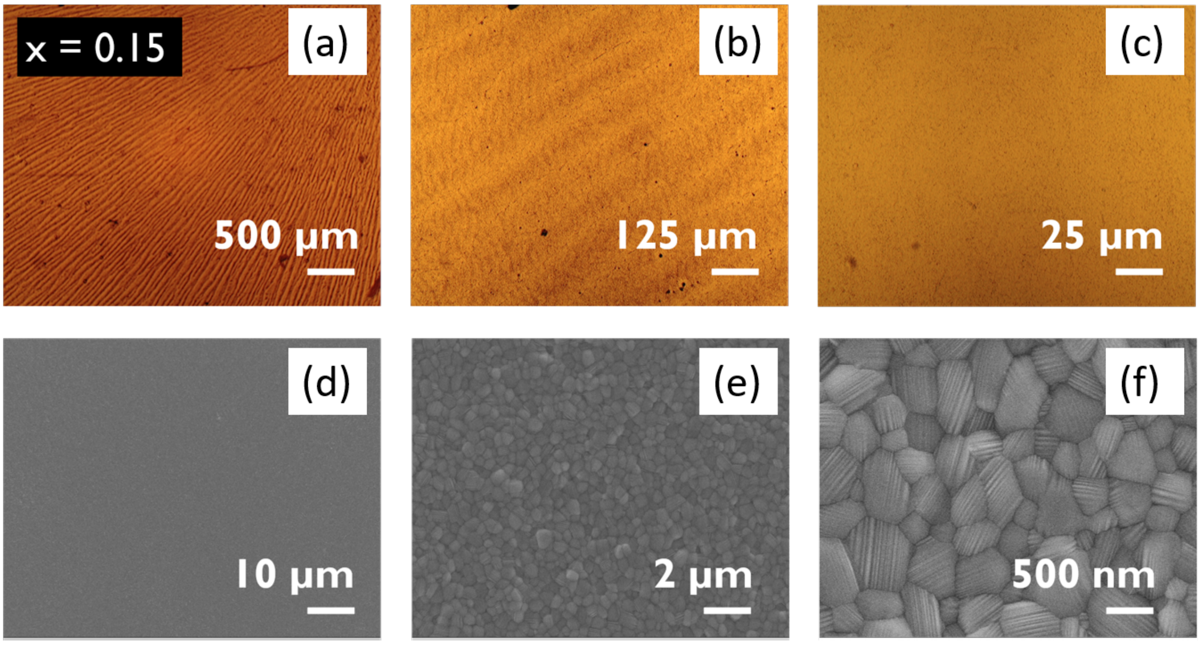

Figure 5.8: (a, b, c) Optical microscopy images and (d, e, f) Scanning electron microscopy images displaying morphological features of (x = 0.15) $(MAPbBr_3)_{0.15}(FAPbI_3)_{0.85}$ showcasing overall smooth surface with striated surface from spin coating in OM data. SEM display striped crystal surface from twinned crystals.

5.4 Impact of chemical composition on internal film structure

Apart from the surface morphology of the film, it is imperative to probe the internal crystalline characteristics of the thin film, as the local charge generation and transfer processes originate from nano and sub-nano lengthscales. A straightforward way to probe crystalline nature of films is through X-ray diffraction (XRD). Apart from crystallographic identity of the materials, the organization of the crystals within the film with respect to the substrate is a pertinent parameter, which notably translate into the directional anisotropy (in-plane and out-of-plane) of functional properties, of particular relevance in devices within thin film architectures. This parameter serves as a measure of the crystallographic orientations within a film and signifies the spatial arrangement and spread of the various lattice planes within films. High extent of preferred orientation would create preferential and focused pathways for charge extraction and transfer within functional stacks which can be appropriately engineered in accordance with the inherent preferred orienta-

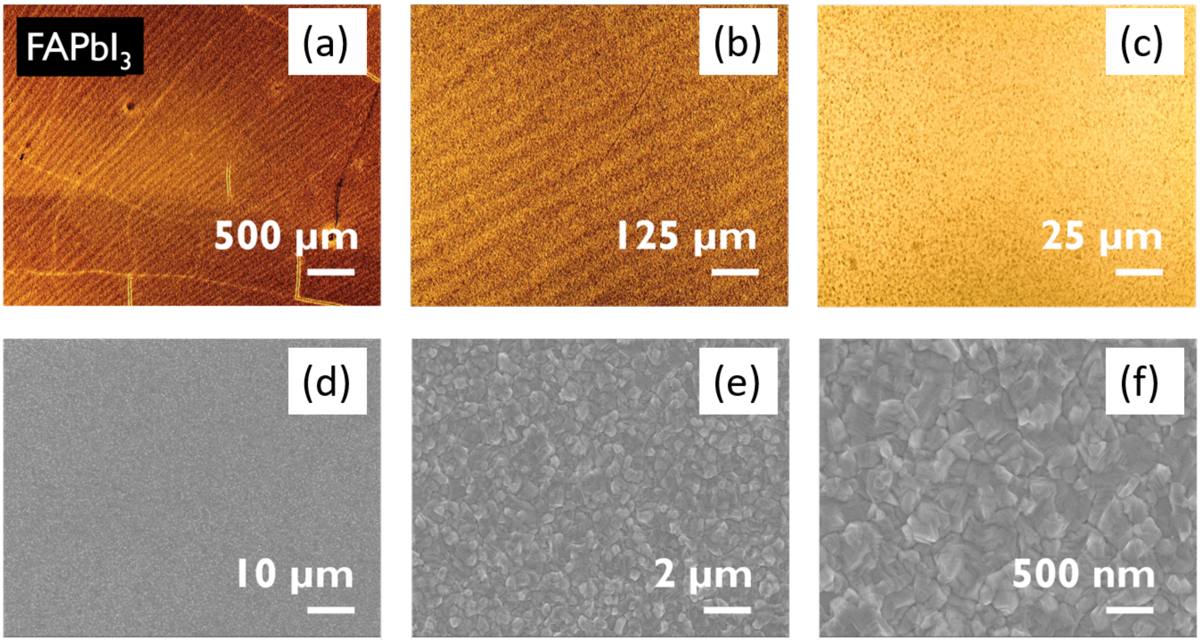

Figure 5.9: (a, b, c) Optical microscopy images and (d, e, f) Scanning electron microscopy images displaying morphological features of (x = 0) $FAPbI_3$.

tions within samples. Crystallographic preferred orientations are investigated by means of grazing-incidence wide angle x-ray scattering (GIWAXS). This technique has been well established and is especially well-suited for characterization of perovskite films [57, 110].

Within the hybrid perovskite systems, for $x = 1$, the XRD data of $MAPbBr_3$ suggest a lattice spacing of $a = 5.92$ Å with a high degree of preferred orientation within the thin film (Figure 5.11). The intensities corresponding to the (110) and (111) lattice directions are hardly recorded, which arises due to the limitation of XRD, wherein contributions from lattice planes scattering away from specular directions are beyond the scope of detection. The limitations of XRD are overcome by means of GIWAXS, wherein the diffraction signal is recorded by means of a two-dimensional (2D) detector. The 2D GIWAXS data of $MAPbBr_3$ confirms the high degree of crystalline preferred orientation and the (100) plane is found to be perpendicular to the substrate normal, within the Cartesian sample reference frame. The (110) plane is oriented at 45° from the substrate, with a narrow azimuthal spread (FWHM) of 1.63°, and the (111) plane is oriented at 57° with an azimuthal spread of 1.45°. The pattern by itself reflected the cubic symmetry from

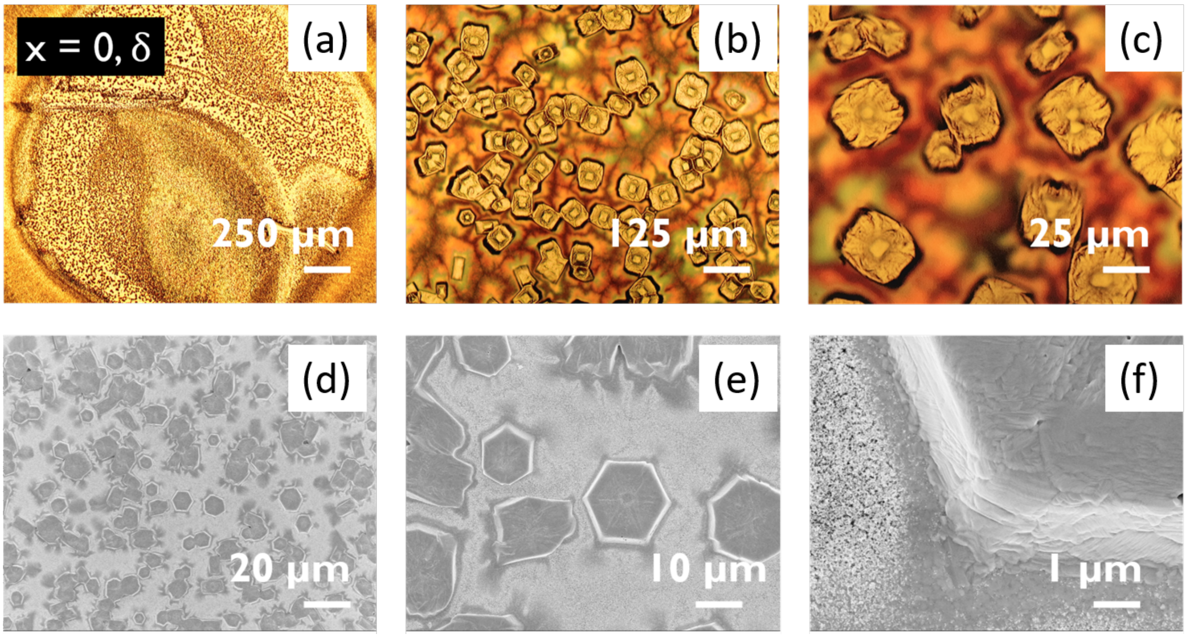

Figure 5.10: (a, b, c) Optical microscopy images and (d, e, f) Scanning electron microscopy images displaying morphological features of the degraded, undesirable hexagonal phase of $FAPbI_3$.

the well-defined crystalline orientations. In accordance with the x-ray data, SEM shows flat surfaces which correspond to the (100) planes of perovskite.

For x = 0.85, the XRD data suggest a lattice spacing of a = 5.99 Å (Figure 5.12). The FWHM of the Bragg reflections within XRD increase with respect to x = 1. This suggests an increased structural disorder, which is in order with the mixed perovskite species, where the lattice can hold higher structural variations on average. SEM suggests slightly larger crystallite sizes for the sample, which rules out size effects responsible for the observed broadening. The material is well textured and the (100) plane is aligned along the substrate. The GIWAXS data confirmed the cubic symmetry of the material and a preferred orientation is found with an increased azimuthal spread of the planes compared to x = 1, signifying a decreased extent of preferred orientation within the film. The azimuthal broadening of the (110) plane is 1.75°, and 1.72° for the (111) plane. The data suggest that in spite of the microstructure within the film, the material displays a high extent of order and the minor increase in mosaicity can be a direct impact of the folded film.

For x = 0.50, the XRD data display the known crystallographic peaks concordant with a pseudo-cubic symmetry, with lattice spacings of a = 6.14 Å (Figure

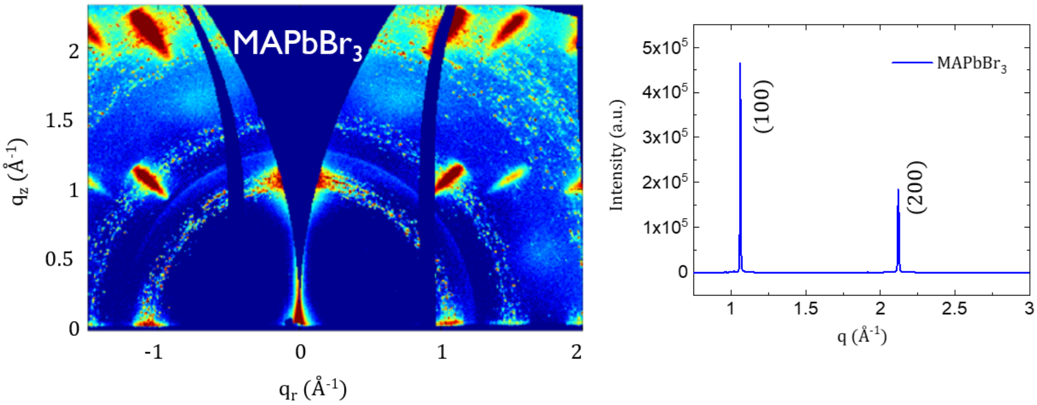

Figure 5.11: 2D GIWAXS and XRD data for (x = 1) MAPbBr$_3$ showcasing a highly textured thin film in the (100) direction.

5.13). The diffracted intensities of the sample are significantly lower as compared to x = 1 and x = 0.85 and in addition to the high background, the data suggest increased structural disorder and increased roughness within the sample with a possible increase in the amorphous content in the film. The observations are also in line with enhanced diffused scattering. This serves as a distinct indication of the considerably increased mosaic nature of the thin film apart from microscopy observations. The increased FWHM of the Bragg peaks implies material strain. Notably, this strain is attributed to composition driven intrinsic disorder within the thin film. The mixed lattice reflects strain due to structural distortions arising

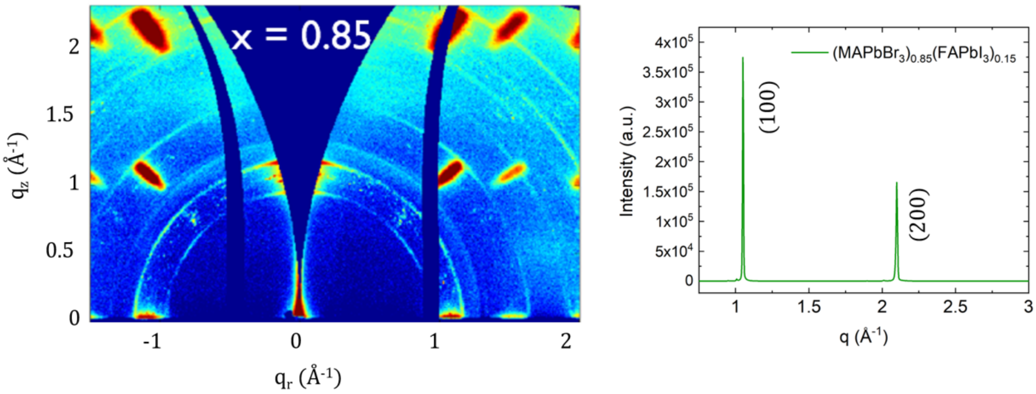

Figure 5.12: 2D GIWAXS and XRD data for (x = 0.85) (MAPbBr$_3$)$_{0.85}$(FAPbI$_3$)$_{0.15}$ showcasing a highly textured thin film in the (100) direction.

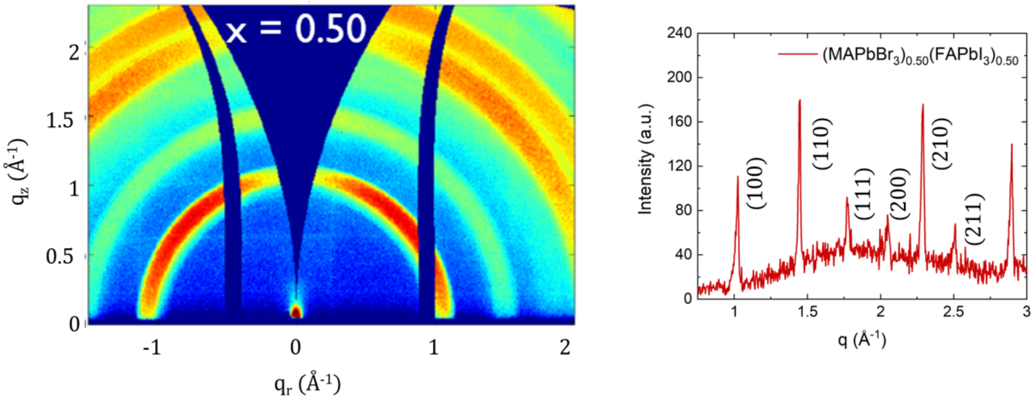

Figure 5.13: 2D GIWAXS and XRD data for (x = 0.50) $(MAPbBr_3)_{0.50}(FAPbI_3)_{0.50}$ showcasing a mosaic spread of orientations.

because of the stochastic distribution of cationic and anionic species. Both, the octahedral structure forming Br and I ions have equal probability to occupy positions within the octahedral lattice sites, as well as the MA and FA ions to occupy the cubo-octahedral sites. Such strain and disorder exists at sub-nano lengthscales and sustains long annealing treatments within perovskite lattices. GIWAXS data for the material confirm the mosaic nature of the film with drastically reduced extent of preferred orientation within the film with the FWHM of the azimuthal spread of the (100) plane being around 49.71°. The azimuthal spread of the various crystallographic peaks suggests a preferred orientation of the (111) plane normal to the substrate. The emergence of the orientation is reconstructed on the basis of the orientation of (100) plane. SEM data exhibit crystals with rough surfaces and non-homogeneously cut facets which are characteristic of vicinal crystallographic planes.

For (x = 0.15) the XRD data (Figure 5.14) suggest a pseudo-cubic structure with a lattice parameter of the system calculated from XRD corresponding to a = 6.33 Å. XRD data display lower diffracted intensities as well as a higher background, indicating increased surface roughness as well as the presence of possible amorphous content within the film. The Bragg reflections have increased FWHM, indicative of increased strain within the crystallites. The GIWAXS data suggest the distributed azimuthal preference of the (100) plane being around 25.38° and the (001) plane at about 55.56°. Together the two planes are twinned about the axis of the (112)

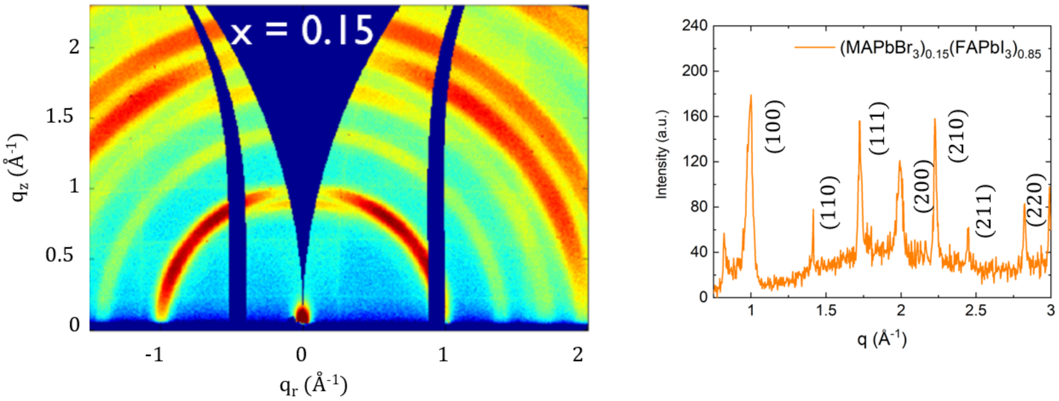

Figure 5.14: 2D GIWAXS and XRD data for (x = 0.15) $(MAPbBr_3)_{0.15}(FAPbI_3)_{0.85}$ representing preferred orientations about (100) and (001) planes at 25.38° and 55.56° twinned about the (112) plane.

plane, which is normal to the surface of the substrate. SEM data too reflect striped crystal surfaces, which have been earlier attributed to nanotwins.

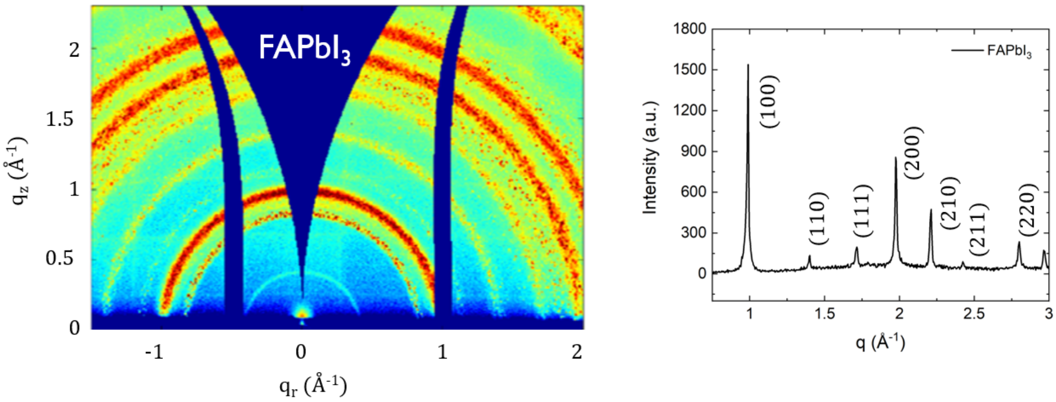

Figure 5.15: 2D GIWAXS and XRD data for $FAPbI_3$ representing the absence of any preferred orientations.

For x = 0, the XRD data suggest the lack of discernible preferential orientations with a lattice parameter of a = 6.36 Å (Figure 5.16). 2D GIWAXS data confirm the absence of preferred orientations, alongside the presence of a hexagonal phase. SEM data of $FAPbI_3$ depicts rough and faceted crystals with visible growth steps on the crystal surface. $FAPbI_3$ crystals also have larger crystallite size as compared to other compositional equivalents. This fact is concordant with the X-ray data wherein the FWHM of the Bragg reflections are narrower as compared to the other hybrid perovskite structures.

5.5 Soft crystalline solids : Implications for crystallization and photovoltaics

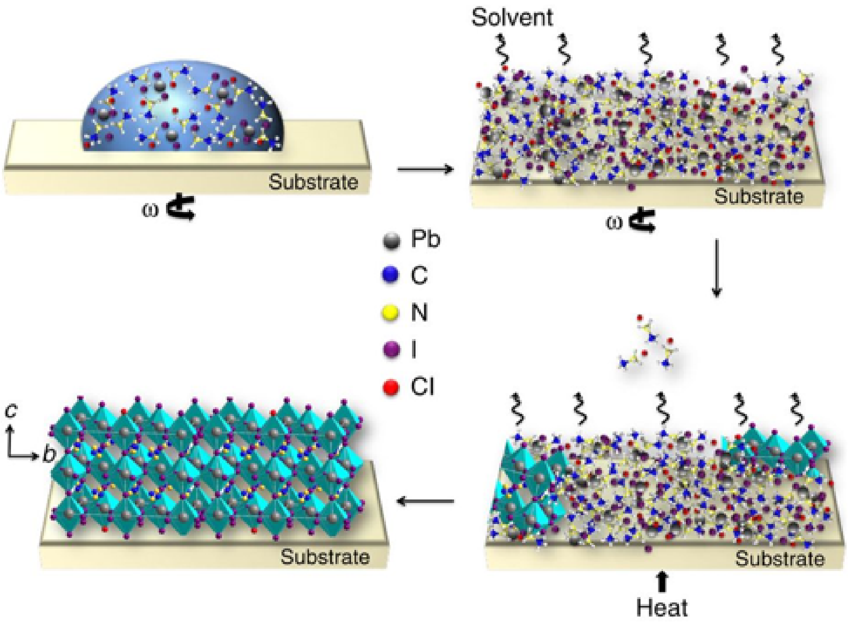

Figure 5.16: Crystallization of perovskites proceeding via spin coating of precursor, removal of excess solvent during spinning and the deposition of intermediate complexes onto substrate. Thermal annealing leads to the transformation of the solvent complex into perovskite. Reprinted from [52] with permission from Springer Nature

Hybrid organic-inorganic halide perovskite alloys alike soft matter systems display varying interaction strength between formational chemical entities within suitable processing media and are characteristically determined by competing entropic and enthalpic contributions. Such systems have extensive degrees of freedom and display cooperative behavior when processed into technologically pertinent architectures such as thin films. The emergence of hierarchical and self-organizing structures has been an extensive field of research where novel material morphologies have been reported in a ubiquitous [111] range of systems including bio-inspired materials, polymer thin films, colloids, droplets, nanoparticles, and even perovskite thin films [17]. Active evolution of hierarchical microstructures and structural heterogeneity [112] has been studied in literature and been attributed to the visco-elastic [113] response of the complex, soft [114] drying fluid to shear stresses experienced during spin coating. Such behavior is indicative of high degrees of freedom of the species within precursor mixtures, which are sensitive to entropic and enthalpic contributions towards free energies of thin films of any particular composition and can be harnessed towards the facile engineering of technologically relevant structures [115]. This is in accordance with reports from literature suggesting that the precursor solution exist as complex colloidal nanocrystalline dispersions rather than simple solutions [18]. Upon deposition of the precursor solution onto the substrate, the precursor is pinned to the base of the substrate. Owing to different interaction affinities between the ionic species present within the precursor state and the solvents used for dispersion, typically discussed within the Lewis acid-base framework for hybrid perovskites, [116] the specie with a higher affinity for the solvent (iodide) is predicted to remain more strongly co-ordinated as compared to the competing ionic specie (bromide). As a result, during spin coating, the removal of the solvent from the nutrient solution typically leads to the emergence of chemical gradients, which on further drying leads to the development of a glass-like state, [117] characterized by the presence of perovskite solvent-complex wherein intermediate prevails atop the underlying precursor volume [118]. Akin to polymeric systems, this glassy state does not hamper evaporation of the solvent, allowing the continued reduction of the more volatile solvents from underneath during annealing. The formation of a glassy state leads to the emergence of dynamic surface instabilities within the fluid fractions held under the gel-state of the intermediate. Marangoni flows [119] within the fluid fractions lead to the emergence of distortions on the film surface. The development of surface features too is guided through the glassy state. The evolution of the film in non-equilibrium during deposition and drying triggers the development of hierarchical features such as buckles, folds, cracks, etc. A drying film develops cracks during volume reduction on evaporation of the solvent from the system and the crystallization of material when the temporal evolution of stresses within the dynamic system and strain responses within the film occur at timescales that the drying film lags in response to the internal stresses it experiences. Once the material cohesive strength is transcended by the tensile stress, the material develops crack patterns. In case of buckling, strain evolves such that the material is able to partially relieve some of the dynamic stresses generated during drying. This indicates that the precursor suspension experiences anisotropic drying rates, shape/volume distortions and has the capability to self-organize to the stress fields it experiences, contingent on the time scales of evolution of the stress [120]. Thus, hierarchical structures within thin films can be an outcome of the rapid diffusion limited cluster aggregation, wherein the formation of a gel-like state is well-known, especially within saturated colloidal dispersions. The evolution of microstructure is attributed to the fluctuations in energetics of the liquid state during evaporation of the solvent from the precursor solution due to transient imbalances between the radial spread of the aforementioned solution on a rough surface and the evaporation of the solvent from the same solution stretched upon the substrate. The scale of morphological irregularities are guided by competition between forces stabilizing local crystallographic microstructures versus forces destabilizing macroscopic morphology affecting larger length scales, even exceeding several mm. Thus, the form of topological design for different chemical systems varied, which is attributed to altered chemical equilibria and differences in the energy dissipated during the outspread of different precursor fluids, as well as the length scales of forces experienced by the fluid during drying. Materials crystallizing over isotropic, mesoporous titania substrates with distinct preferred orientations are indicative of growth modes wherein the crystals while grown on a substrate with highly varying crystallographic growth directions, nonetheless exhibit preferred orientations guided through the interplay of kinetics and thermodynamics of the process of crystallization from a complex fluid phase [19]. The emergence of diverse preferred orientation suggests that the drying phase would possess energy and follow growth kinetics compatible with energies required in order to organize into a state akin to thermodynamic equilibrium, with the settlement of adatoms to their energetic minima.

Emergence of orientations away from equilibrium would result in the growth of non-singular crystal planes [121] due to kinetic instabilities occurring within the drying precursor, since the growth of flat faces has higher energetic barriers and thus, the slowest kinetics. Non-singular crystal faces are known to possess atomically rough surfaces, due to the presence of a large number of kinks as well as terraces and ledges as is observed in case of the $x \neq 1$ and $x \neq 0.85$ compositions.

Roughening of such nature has energetic demands for the growth of vicinal planes by mass transfer. The broad mosaic spread of the lattice plane orientations is in accordance with the rapid kinetic growth of the crystals since the growing crystals have no temporal possibility of evolutionary selection or ripening. The instability continues to affect the film at a larger length scale, too, as evident through the overall rough film surface. The emergence of intense hierarchical patterns suggests the highly viscoelastic nature of the precursor, wherein the molecular interactions are no longer akin to a true fluid state, but rather entangled, limiting molecular motions and resulting in turbulent flow. During spin coating of such a viscoelastic fluid, the film experiences shear forces, and the response of the materials causes it to undergo macroscopic rearrangements. Different parts of the film develop different patterns due to anisotropic distribution of shear stresses across the film during spin coating. Another response to growth instability can be twinning within crystals, which occurs due to the presence of stacking faults, which originate from shear experienced during crystallization. Such an event leads to increased strain within the crystal and be concordant with the high FWHM of Bragg signals in XRD. In addition to twinning, shear stresses can also lead to phase transformations within materials, wherein an exemplary cubic phase could undergo transformation into a hexagonal phase by dislocation of gliding planes along a stationary axis Higher activation energies of crystallization as in the case of $FAPbI_3$ would depict that at nominal processing temperatures, the system has high dynamic disorder. Crystal growth in such cases is again kinetically driven, leading to the lack of preferred orientations arising within the thin film. Nuclei with orientation freedom have a higher probability to emerge and during subsequent growth, the energetic barrier for formation of new steps or kinks is lower as compared to smooth surfaces. Consequently, the film surface develops with a rough and irregular surface. Further growth of the crystal seed continues via an arbitrary transient shape, followed by a series of growth steps, which finally determine the steady state parameters of the final crystal (i.e. size, shape, surface smoothness).

Considering the lattice structure of hybrid perovskites, for pure Br perovskites, the inorganic matrix is stiffer as compared to I based systems, due to differences in the Pb-X bond lengths and bond angles. The variances give rise to differences in structural order within the inorganic matrices, with the I-containing framework reflecting higher disorder compared to the Br framework. This disorder within the inorganic octahedral could serve as the primary source of varying structural

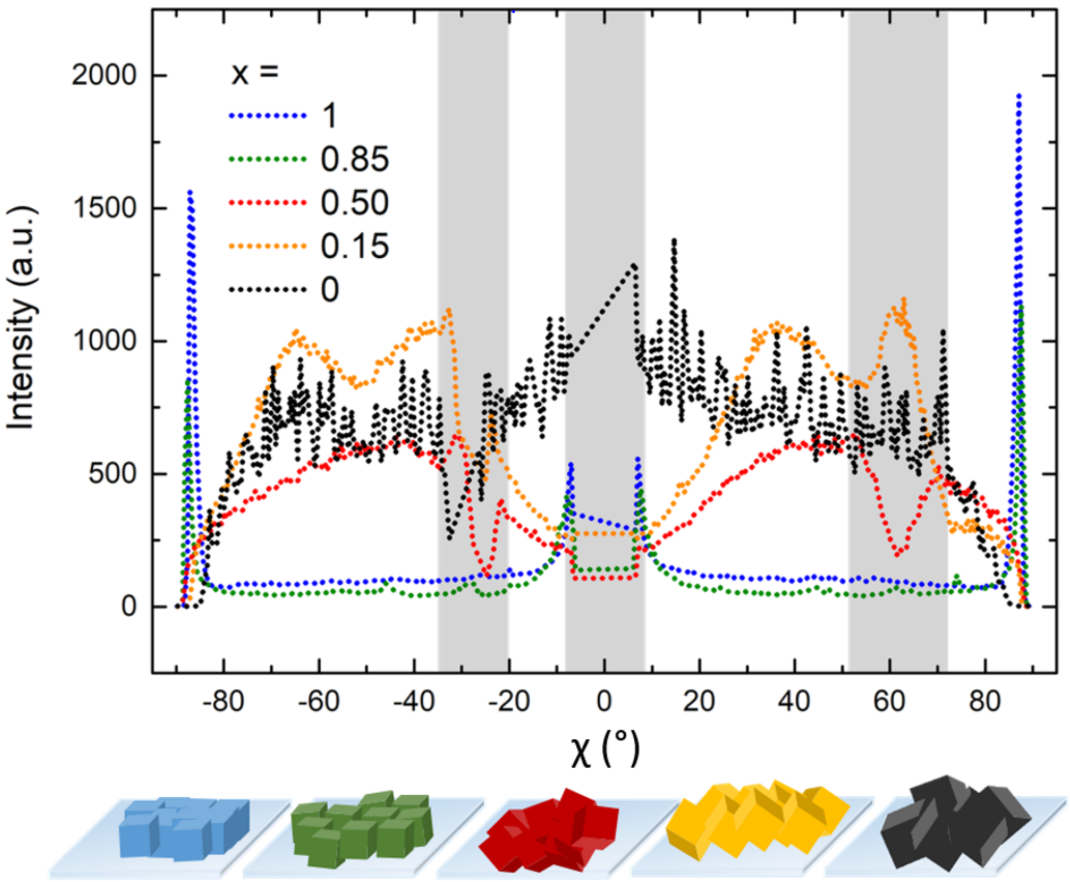

Figure 5.17: Azimuthal (χ) spread of the (001) lattice plane for $(MAPbBr_3)_x(FAPbI_3)_{1-x}$ films reflecting preferred growth directions of crystallites in thin films. Greyed regions correspond to the inaccessible detector gaps and the missing wedge from Ewald sphere correction of the 2D GIWAXS data. Adapted from [20] with permission from American Chemical Society, copyright 2020

identities within resultant thin films and could explain difference in the crystalline preferred orientation within different compositions of hybrid perovskites 5.17. Ideally, structural disorder within hybrid mixtures would be between the octahedral forming halide species in question, with the organic species occupying the cubo-octahedral positions. In order to distinguish the effects of the cationic organic and anionic inorganic species, the morphologies of hybrid halide systems are investigated. While maintaining the cationic species, and by varying the ratio of halides within $(MAPbBr_3)_y(MAPbI_3)_{1-y}$, the highest extent of crystalline preferred orientations is observed for $MAPbBr_3$. On increasing the iodide content within the mixed systems, the extent of preferred orientations decreases, as evidenced by the azimuthal spread of the lattice plane reflections in GIWAXS. However, when compared to the mixed cation-mixed anion compositional counterparts, the mixed halide films display notably higher structural order with increased tendencies for the (100) planes to be aligned along the substrate and a narrower spread within the azimuthal angular distributions, while showcasing absent signatures of amorphization in the form of a broad background and noisy diffraction peaks observed in mixed cation-mixed halide systems (x = 0.50, 0.85). This suggests that while Br-rich compositions show less variation (narrower FWHM) within the spread of the crystallographic orientations as compared to their I- counterparts, the inclusion of an additional cation induces considerable structural disorder.

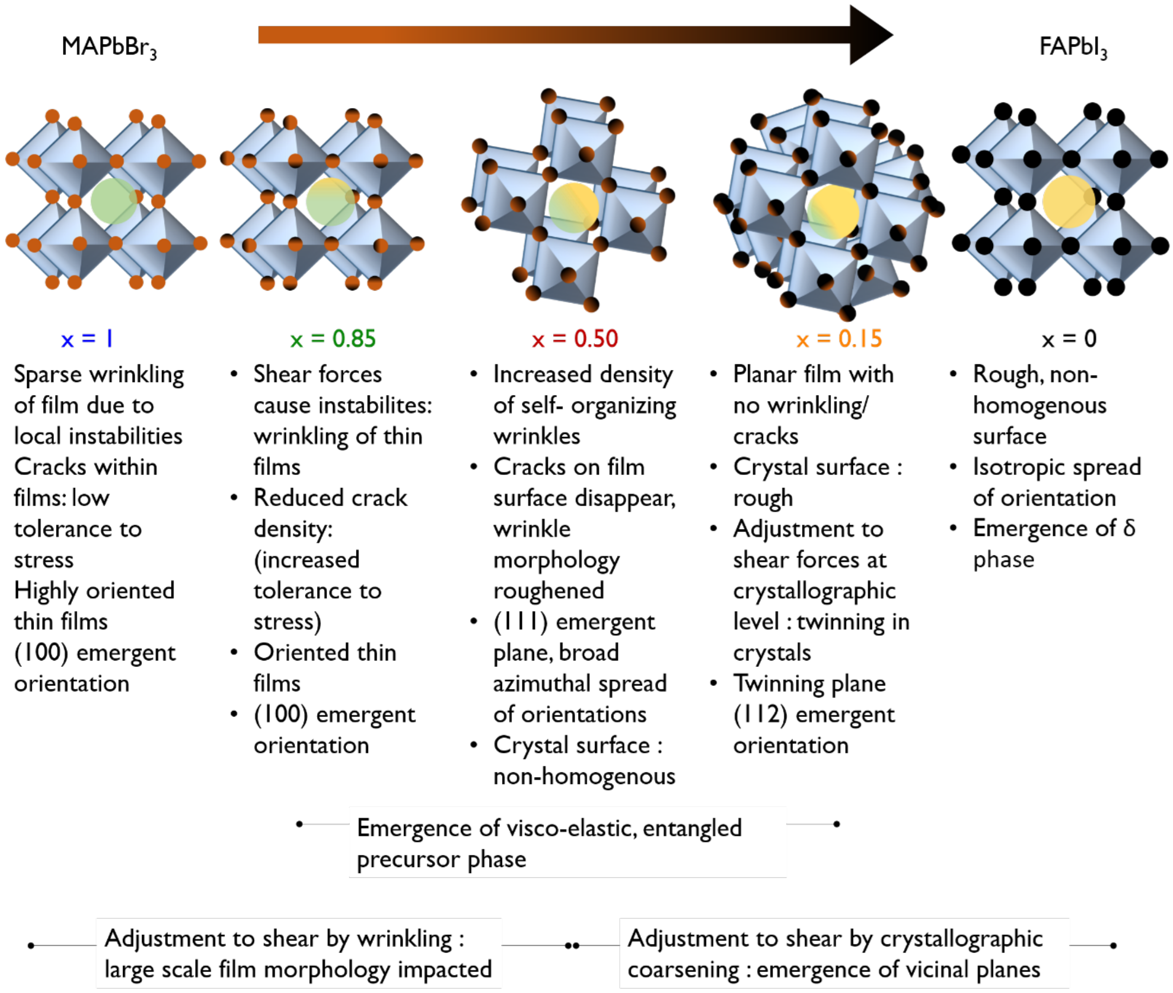

Figure 5.18: Schematic reflecting the structural characteristics of the varied compositions in the hybrid perovskite $(\text{MAPbBr}_3)_x(\text{FAPbI}_3)_{1-x}$ films and the emergent disorder arising within the lattice from their mixing. Adapted from [20] with permission from American Chemical Society, copyright 2020

Mixing of perovskites gives rise to highly complex and dynamic visco-elastic precursors, and the extent of complexity and the degrees of freedom increase with increasing chemical species within the precursor. Such mixtures have increased disorder in positioning of different chemical species within the solid solution formulated thereof (Figure 5.18). This increased structural disorder also results in local structural heterogeneities. Intriguingly, alloyed materials are known to exhibit increased flaw tolerance in the material by inducing structural rearrangement in high stress regimes [122] during drying. Such behavior can explain why mixed perovskites are more resilient to mechanical failures such as cracks, and instead reflect folded or buckled microstructures, suggesting that hybrid systems possess higher 'softness' than their parent compounds. Correlation between high structural disorder and emergence of hierarchical structures within structures suggests drastically changed rheology and other thermomechanical of the precursor and is possibly caused due to entanglement of hybrid perovskite precursor. Such entanglement effects vary as a function of concentration and stoichiometry of the precursors. Hence, film microstructure can be controlled by varying the precursor chemistry and resultant film thicknesses. The structural rearrangement [123] and emergence of preferred orientations within thin films [124] is shown to be feasible even in highly anisotropic and turbulent processes such as spin coating and is a response of the precursor to the anisotropic stresses it experiences during film formation [98]. With the solution-air interface induced instability in drying precursors, emergence of preferred orientation would originate from the precursor-air interface, especially when considering the disordered substrate upon which it grows, which is in accordance with other studies [125]. The impact of the chemical/ colloidal identity of the precursor supersedes the nature of the underlying substrate during the spin coating process and consequently the emergent orientations are independent of substrates. Due to the colloidal nature of the precursor and its self-organizing tendencies, controlling the colloidal chemistry as well as drying kinetics will translate into direct impact on the perovskite film nano and microstructure. The hierarchical structures within thin films present opportunities to overcome demanding technological requirements for film structuring such as photo/electron beam lithography, etching and molding. Structured thin films provide light trapping opportunities as well as intrinsic antireflection layers. The soft and tunable mechano-morphological characteristics of hybrid materials make them tolerant to stress and make them well suited for flexible optoelectronic applications. The tuning of crystallographic orientations within materials is desirable for catalytic and sensing applications.

5.6 Summary

Hybrid perovskites form solid solutions on intermixing of stoichiometric equivalents of precursors. Mixed halide perovskites and mixed hybrid perovskites are fabricated by spin coating of colloidal precursors. Thin films showcase independent crystalline and optical structure on formation and are characterized for their ability to form alloys. Each hybrid composition represents a unique diffraction pattern which can be tuned by substitution at the cationic A or anionic X site within the ABX_3 lattice. Thin films display hierarchical mesoscale and microscale texture in the forms of cracks, folds, wrinkles and twinned crystals. These microstructures emerge at scales concordant with the adjustment of shear at the overall film scale or at the crystallographic scale. For alloyed compositions of pure perovskite compounds, the precursor exists in a viscoelastic, entangled state which leads to rearrangement of the film during its drying. The films represent the capability of self-structuring which holds advantages for the formation of textured surfaces. Further, the softness of the alloyed compositions has beneficial implications for flexible thin films of hybrid perovskites, wherein the material accommodates external deformation by morphological relief.

6 *In situ* crystallization of colloidal precursors to thin films

This chapter is based on the publication
”Out-of-equilibrium processes during phase transitions: An *in situ* crystallization study of organic-inorganic perovskites during spin coating”
S. Pratap, F. Babbe, N. S. Barchi, Z. Yuan, T. Luong, Z. Haber, T.-B. Song, J. L. Slack, C. V. Stan, N. Tamura, C. M. Sutter-Fella and P. Müller-Buschbaum,
Accepted at Nature Communications

Introduction

Metal halide based hybrid perovskite materials have attracted significant research and development interest due to their truly impressive and broad applicability as functional materials. The technoeconomic advantages of hybrid perovskites, in addition to their stellar optoelectronic properties, [77] arise from their facile and low-cost solution processability [15]. Spin coating is a well-established and widely utilized method for the formation of high-quality perovskite thin films. In recent years, improvements over conventionally spin coated thin film morphologies were achieved by exploiting treatment methods such as Lewis acid-base precursor adduct engineering, [126] complex intermediate driven crystallization, [127] additive usage, [116] intramolecular exchange [128] and antisolvent [129] driven film formation. Post deposition film treatments such as thermal [130] and solvent-vapor annealing [40] have also been explored to eliminate undesirable [131] structural constraints and also known to lead to morphological effects such as the emergence of hierarchical microstructures within thin films [20]. Significant efforts toward controlling perovskite thin film qualities have been undertaken because of the correlation [100] between device performance metrics and thin film structural characteristics. Moreover, a growing appreciation of the degree to which the structural quality of thin films is determined during initial kinetic processing of colloidal precursors has instigated close study of the evolving processing-structure-property relationships within thin films.

6.1 Multimodal *in situ* measurements

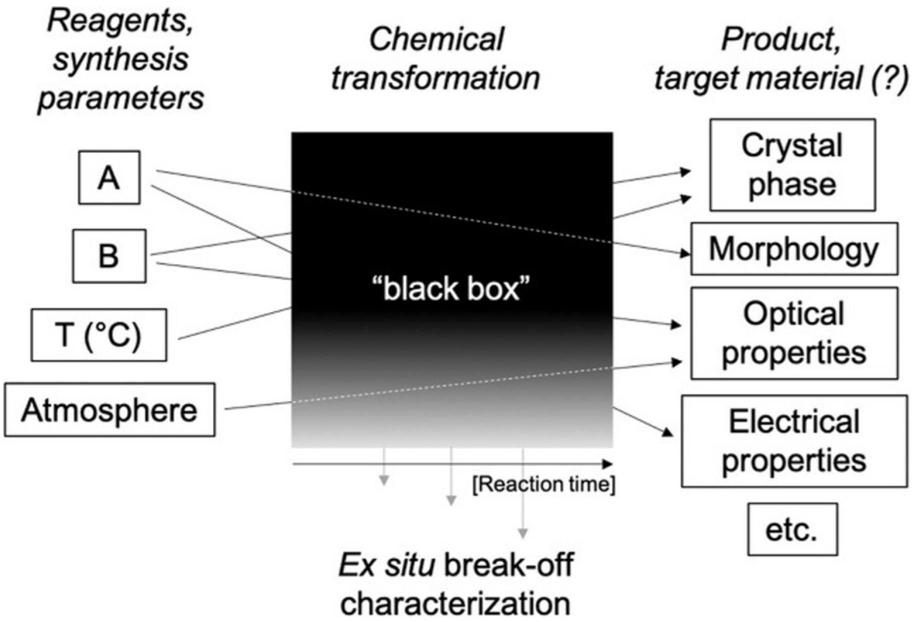

Figure 6.1: The transformation of reagents to products is a complex process which includes the involvement of multiple physical changes and associated chemical phases. Phenomenological correlations during changes are not possible during *ex situ* investigations. Reprinted from [132] with permission from Wiley.

Spin-coating is a solution based processing method, which produces non-equilibrium thin films **(Figure 6.12)**. The crystallization of colloidal precursors of hybrid perovskites has an inherent multivariate nature and is known to lead to reproducibility issues of film characteristics. Routes of crystal growth have been discussed, [45] depicting how starting from generic precursor molecules, materials crystallize to their bulk form through multiple reaction pathways. Complementary and multimodal metrological techniques help elucidate complex transformation mechanisms responsible for reproducibility issues. For instance, it is possible for the precursor to follow physicochemical growth pathways such as spinodal decomposition, [133] which deviate from the reaction pathways involving traditionally nucleated species. Rather, for instance, chemical reactions may proceed through the formation of intermediates, which convert to their final structural form on further treatment.

Conceptualizing an understanding of complex growth processes requires the fixing of processing parameters, which we have done in the present study. In this work, we actuate the advantages of real-time investigation of the evolving structure and optoelectronic properties by combining grazing-incidence wide-angle X-ray scattering (GIWAXS) and photoluminescence (PL) spectroscopy while emulating the one-step antisolvent-assisted crystallization of a perovskite thin film. We chose to investigate methylammonium lead iodide ($CH_3NH_3PbI_3$, $MAPbI_3$), whose structural intermediates and transformation kinetics have been extensively investigated. This was done as a manner of demonstrating that much remains to be learned about out-of-equilibrium assembly processes of exemplary model systems. We report on the characteristics of the metastable structure formed by the first order phase transition occurring during antisolvent induced nucleation from the colloidal precursor sol. Further, there is a partial transformation of the metastable nuclei by concatenation of nanostructures leading to the formation of a solvent-complex, with the solvent-complex being stable against thermally induced degradation up to 100°C. Around 100°C, a second order transformation process of the complex to $MAPbI_3$ is initiated, by evaporation of the solvent from the thin film. Physicochemical reaction gradients are found emergent and attributed to differential rates of removal of strongly coordinated solvent molecules by advection of the evaporating solvent molecules from the film thickness. This mechanism of solvent removal results in a process of dissolution-recrystallization to lead to the final $MAPbI_3$ thin film. Further annealing leads to a ripening process of crystals within the thin film. Evolutionary data signatures, physical concepts and characteristics within structure-function correlations learned from model system of $MAPbI_3$ are transferable to other chemical compositions of hybrid perovskites. These insights are enabled through the developments of a novel analytical cell [19], which allows complete remote control over the spin coating process, antisolvent drop, PL excitation, and the annealing protocols. The processing and measurement environments are housed within an inert gas-purged cell to curb unfavorable degradation by atmospheric oxygen and moisture [134].

6.2 *In situ* crystallization revealed through GIWAXS and PL

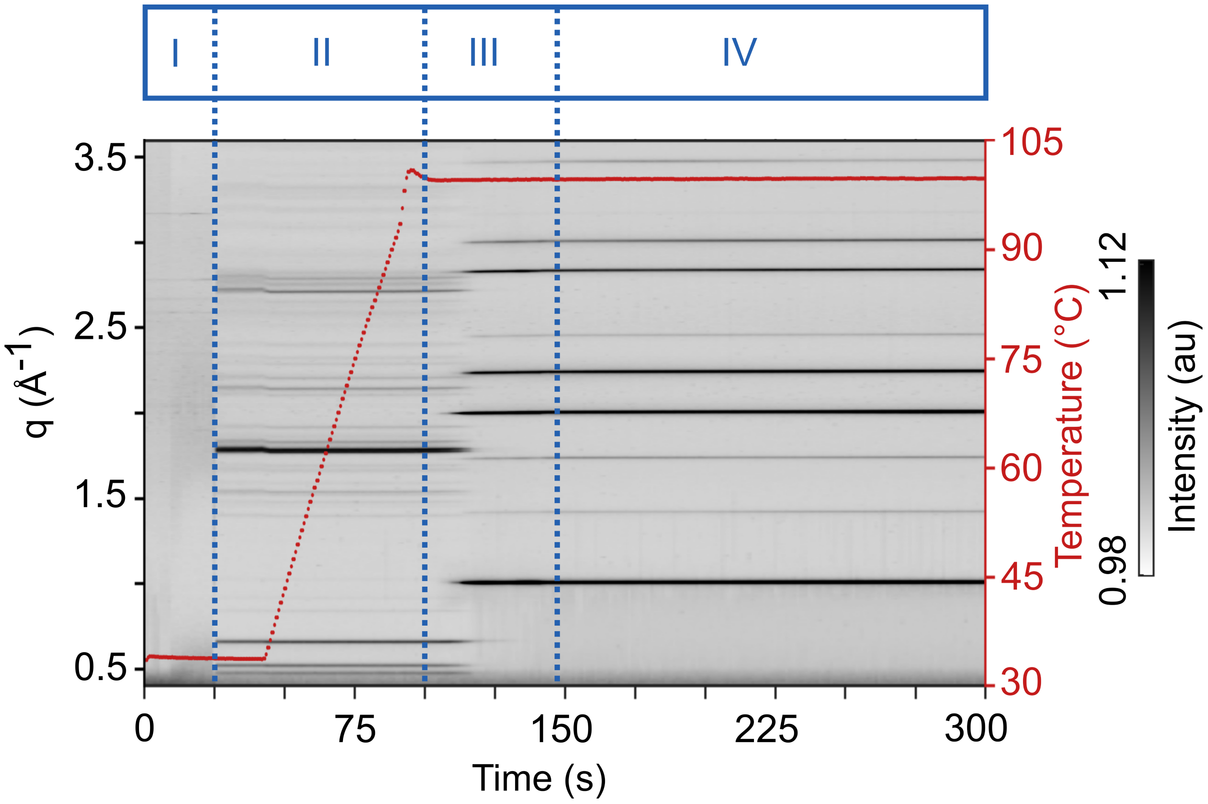

Figure 6.2: Integrated *in situ* GIWAXS data of the crystallization process of a colloidal perovskite precursor prepared by antisolvent drop and thermal annealing, showcasing four conversion phases.

An overview of the evolution of structural and optoelectronic phases recorded by GIWAXS and PL is presented in Figure 6.2 and Figure 6.4. Key structural phase transitions witnessed in diffraction are presented as individual 2D diffraction images in Figure 6.3. During the experiment, four equilibrium phases and three transient conversion processes are registered as explained below.

In the first phase (phase I, $t = 0$ - 24 s), the liquid precursor is spin coated and reflected as diffuse halos centered around 0.5 Å^{-1}, 1.8 Å^{-1} and 3.0 Å^{-1} (Figure 6.3) in the diffraction data. In line with other reports, [135–137] this signal is attributed to scattering from the mixture of the solvent and solute phases, composed of a colloidal dispersion of chemically and structurally diverse plumboiodide scattering species [18,41]. The low scattering contrast of the halos signifies the well intermixed state of the solutes and solvents and the lack of any Bragg diffraction confirms the absence of long-range order within the precursor state. Phase I does not show any PL response. Following 24 s of spin coating, an antisolvent stream is dynamically

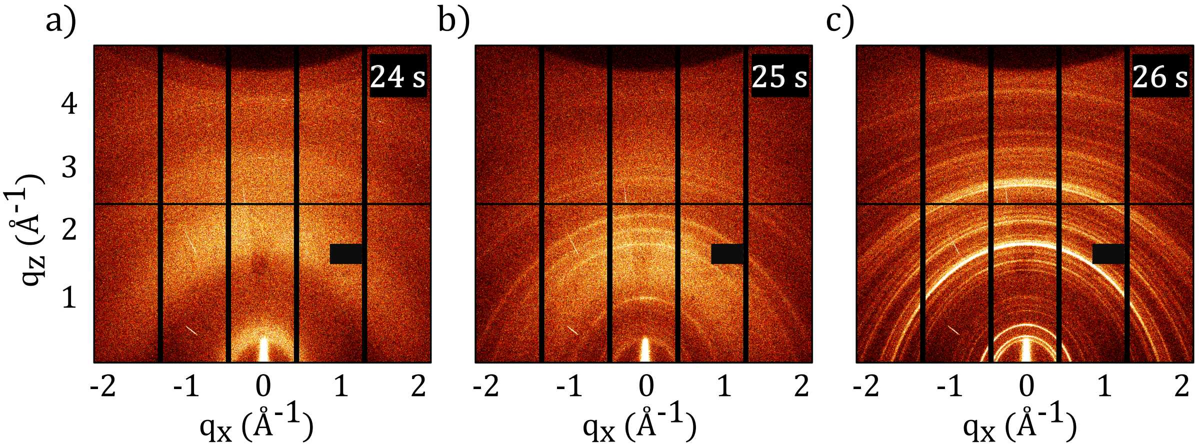

Figure 6.3: 2D GIWAXS data during structural conversion of $MAPbI_3$ thin film (a) before, (b) during and (c) after the antisolvent drop at t = 25 s. Diffraction from (a) colloidal mixture of solid precursors and solvent molecules, (b) instantly nucleated crystalline $MAPbI_3$ nanocrystals and nutrient colloidal phase in slight background and (c) crystalline orthorhombic $MAPbI_3 \cdot DMSO$ solvent-complex.

dispensed (the film is in spinning motion), resulting in rapid structural changes within the precursor phase. The diffuse halos from the precursor phase convert into low albeit distinct intensities with Bragg peaks located at $q = 1.01$ Å^{-1}, 1.78 Å^{-1}, 2.00 Å^{-1}, 2.24 Å^{-1}, 2.84 Å^{-1} and 3.01 Å^{-1}. The amorphous background and low intensities of the Bragg peaks suggest an incomplete conversion of the colloidal precursor to the proceeding state. The film is found to be isostructural in terms of peak positions with cubic $MAPbI_3$. Texture of the nucleating structure is attributed to the directionality of the antisolvent dispensing, which was set normal to the substrate plane. The diffraction signal from the nucleating phase quickly transforms to the proceeding state (phase II) suggesting the metastable nature of the causal nucleating structure.

Starting at 26 s, phase II is initiated and the weak diffraction intensities from the metastable nucleated phase are converted into stronger diffraction intensities at 0.46 Å^{-1}, 0.51 Å^{-1}, 0.65 Å^{-1}, 1.75 Å^{-1} together with several subsidiary peaks with lower intensities. The diffraction peaks correspond to the orthogonal crystalline solvent-complex, $Pb_3I_8.2(CH_3)_2SO.2CH_3NH_3$ ($MAPbI_3 \cdot DMSO$) [138–140]. In agreement with other reports, [141, 142] no DMF-based solvent-complexes are observed in spite of the precursor solvent being DMF-rich, due to the stronger Lewis acid-base complexing ability of DMSO [116, 143]. No uncomplexed PbI_2 is observed either. At the end of the spin coating process, at 44s, the annealing of the thin film is initiated with a linear temperature ramp of 1°C/s to convert the solvent-complex to the crystalline perovskite. During the rest of the annealing process, the peaks from the solvent-complex of phase II remain unchanged in terms of peak positions, intensities and widths, until a temperature of 100 °C is reached and stabilized at 100 s.

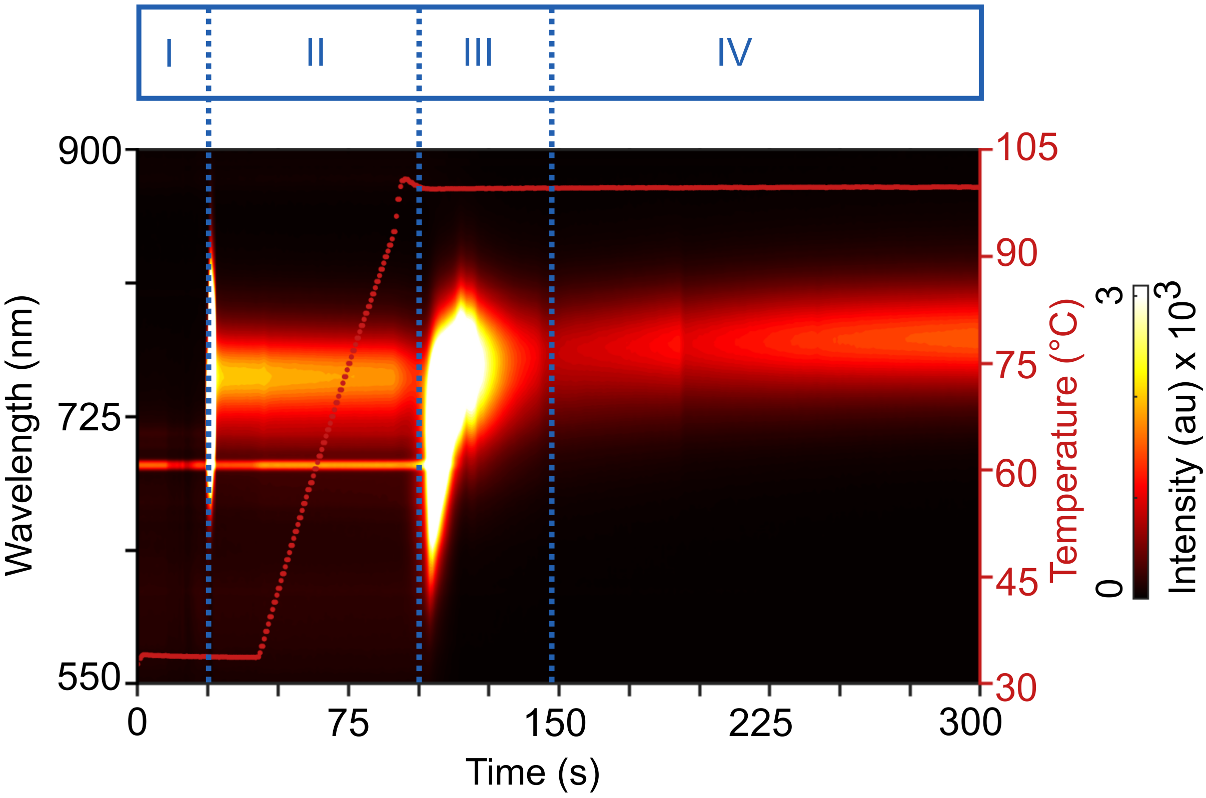

Figure 6.4: *In situ* PL data of the crystallization process of a colloidal perovskite precursor prepared by antisolvent drop and thermal annealing, showcasing four conversion phases.

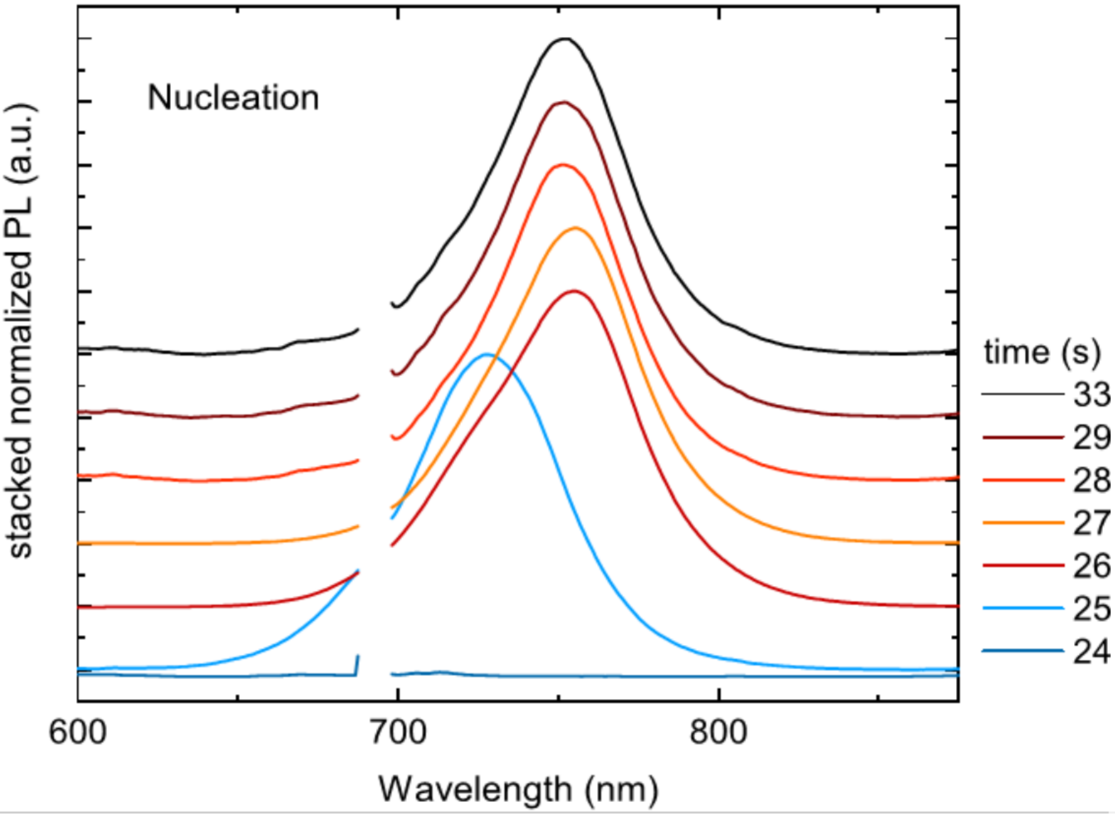

Figure 6.5: Normalized PL data during nucleation and cluster coalescence of phase I after antisolvent drop

The antisolvent drop (t = 25 s) triggers the immediate emergence of an intense and broad PL peak (Figure 6.4) centered at around 730 nm (1.70 eV). The PL emission arises from the instantly formed $MAPbI_3$ nanocrystals, (Figure 6.5) with a polydisperse size distribution of luminescing moieties responsible for the broad FWHM of the PL emission. The peak position, which in first approximation represents the bandgaps, [144, 145] indicates quantum confinement of the charge carriers as typically observed in nanoparticles with a size range within ten nanometers [97, 146–148] (expected room temperature bandgap of bulk $MAPbI_3$ is 1.60 eV [149, 150]. Within the next second, the peak position shifts towards 750 nm (1.65 eV) (Figure 6.5) and remains constant afterwards in phase II. The red shift is due to a growth in the size of nanocrystallites, leading to a reduction in the extent of quantum confinement [148, 151]. The bulk bandgap is not reached, signifying an arrested growth mechanism after a few seconds, due to reaction and diffusion limited constraints [64, 152] of the solvent-complex structures, which required thermal annealing to complete the solvent-evaporation and the transformation of the solvent-complex to crystalline perovskite. The FWHM of the PL peak at 750 nm shows significant narrowing from 130 meV (t = 26 s) to 110 meV (t = 29 s), corroborating the homogenization in size distribution. This occurs through an increase in the average sizes of structures formed by cluster collapse of the nanoparticles which have high correlated surface and interfacial energies. The high surface and interfacial energies are possibly strong driving forces for the cluster coalescence of the nucleated species due to their high surface to volume ratio. Coalescence results in size homogenization of the particles which result in narrowing of the PL spectra. After the polydisperse nucleation process, the $MAPbI_3$ nuclei above a critical radius are expected to remain stable against cluster coalescence. These $MAPbI_3$ crystals which are not bounded into the solvent complex phase are hypothesized to contribute to the remaining luminescence intensity in phase II (the solvent complex does not luminesce). Thereafter, in phase II, the PL response remained unaffected in terms of peak shape, position, and intensity, suggesting remnants of stable perovskite crystals formed during the nucleation process.

On reaching 100°C, around t = 90 s, the solvent-complex undergoes further structural transitions caused by thermal disassociation and subsequent solvent evaporation, marking the initiation of phase III of the crystallization process. Around 103 s, Bragg peaks from a crystallizing perovskite phase start quickly gaining intensity, reaching the maximum at 120 s (Figure 6.6). The evolution of the perovskite phase (black curve) is compared against structural changes of the solvent-complex (green curve) by tracking the intensities of their Bragg peak $q_{100} = 1.00\text{Å}^{-1}$ and $q_{150} = 1.78\ \text{Å}^{-1}$ (Figure 6.6), respectively. The lattice spacings of the perovskite crystals increase while the peak widths narrow, for $t = 104 - 120$s (Figure 6.7). Simultaneously, the solvent-complex Bragg peaks diminish in intensity. This relative intensity change between 104-120 seconds is attributed to the conversion of the solvent-complex to the perovskite state at the film-air interface where the rate of evaporation of the solvent is expected to be the highest.

Beyond 120 s, there is a second, slow decrease in the diffraction intensities of the solvent-complex (Figure 6.6) up to 144 s, which is attributed to the removal of the solvent complex from the deeper parts of the thin film, which require longer annealing times for complete solvent removal. Such an observation confirms insights on the gradients of the structure within thin films, [153] where crystallization occurs within varying thicknesses of the film by solvent evaporation and interdif-

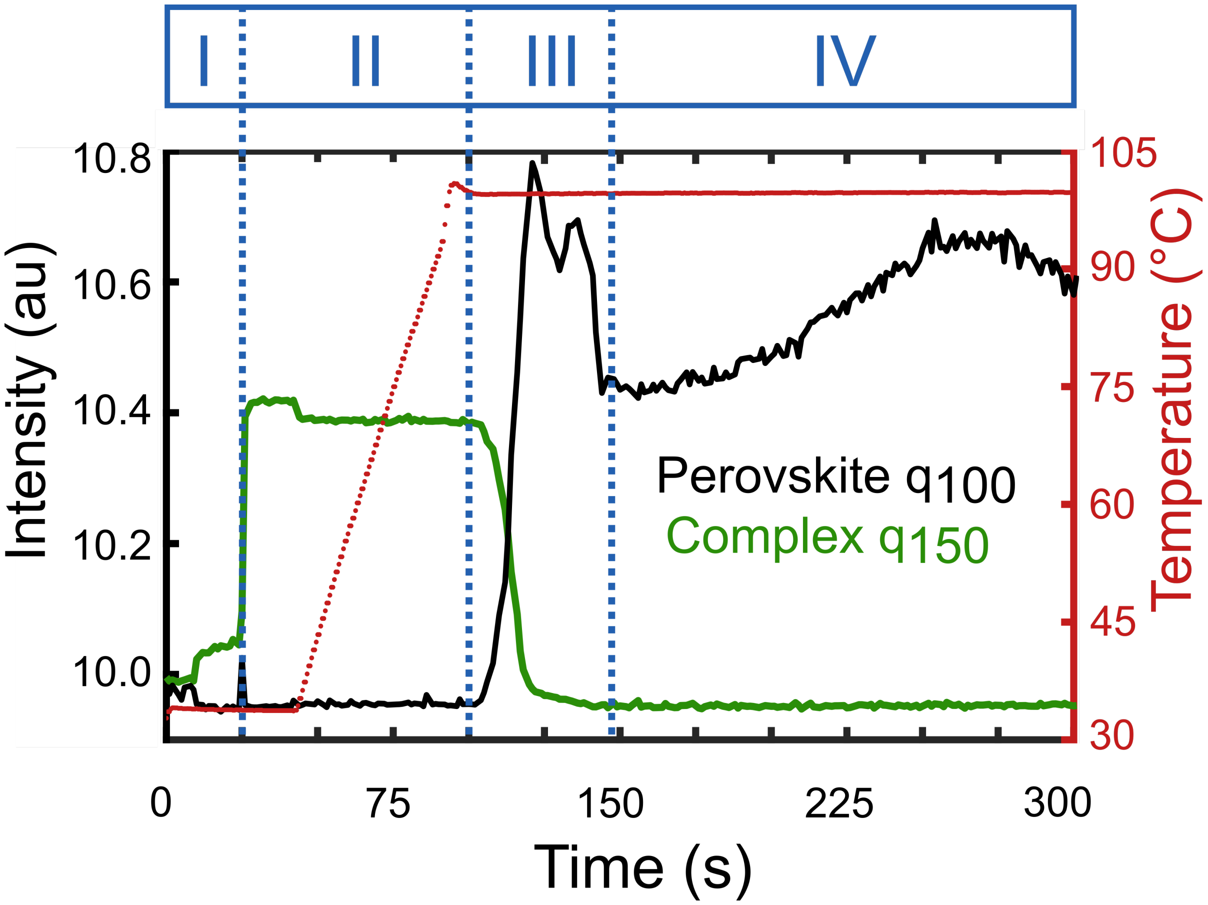

Figure 6.6: The temporal evolution of radially integrated GIWAXS data of $MAPbI_3$ (black) and $MAPbI_3 \cdot DMSO$ solvent-complex (green)

fusion [154] and resultant colloidal assembly [155]. Moreover, the Bragg peaks of the solvent-complex lose intensity from the off-normal orientations faster, and the remaining intensities of the Bragg peaks from the solvent-complex display orientations dominantly normal to the film substrate (Figure 6.8). With continued annealing, the perovskite film crystal orientation becomes increasingly mosaic as seen from the increasing widths of the related Bragg peaks, and the homogenized distribution of the preferential orientation spread of the perovskite Bragg peaks (Figure 6.8). During the gradual removal of the solvent complex, the intensity of the perovskite peak (Figure 6.6) shows distinct fluctuations, first diminishing ($t =$ 121–130 s), then increasing ($t =$ 131-136 s), and then decreasing again ($t =$ 137 – 144 s). These fluctuations are attributed to dissolving and recrystallizing previously formed perovskite crystals as the solvent molecules from deeper interfaces are removed by solvent mass transfer and crystalline rearrangement through the already

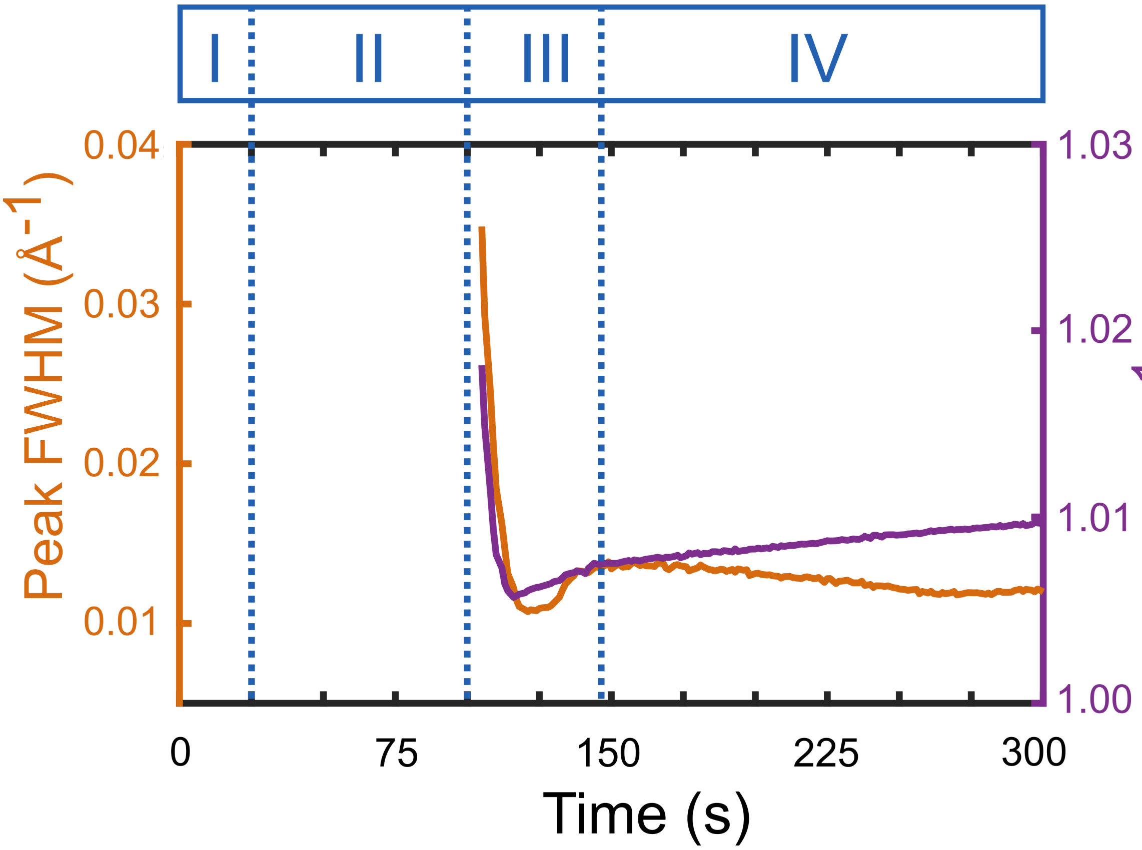

Figure 6.7: The temporal evolution of perovskite lattice parameters during the crystallization process of perovskite solvent complex at 100°C.

crystallized film thickness. The peak width of the perovskite crystals during this stage (t = 121-144 s) increase while the lattice parameters reflect a slight decrease (Figure 6.7), confirming the presence of processes which engender increased structural disorder within the thin film. Any discernible signs from the solvent-complex phase disappear as the film is fully converted into the dry crystalline phase (phase IV, t = 144 s). Upon reaching 100°C in phase III, a second bright PL response emerges between 650 and 740 nm (1.68-1.9 eV), with its center around 1.72 eV and a FWHM of 190 meV (Figure 6.9) observed at t = 104 s (Figure 6.10). This signature is attributed to the co-existence of disparate nanocrystallite sizes with high radiative efficiency. The non-Gaussian peak shape comes from a superposition of luminescence signals with disparate intensity contributions [146, 156]. Akin to the processes occurring during the moments proceeding antisolvent dispensing (t > 25 s), the PL signal intensity decreases and red shifts, indicating growth of the nanocrystallites. The underlying growth kinetics are slower, while the red shift of

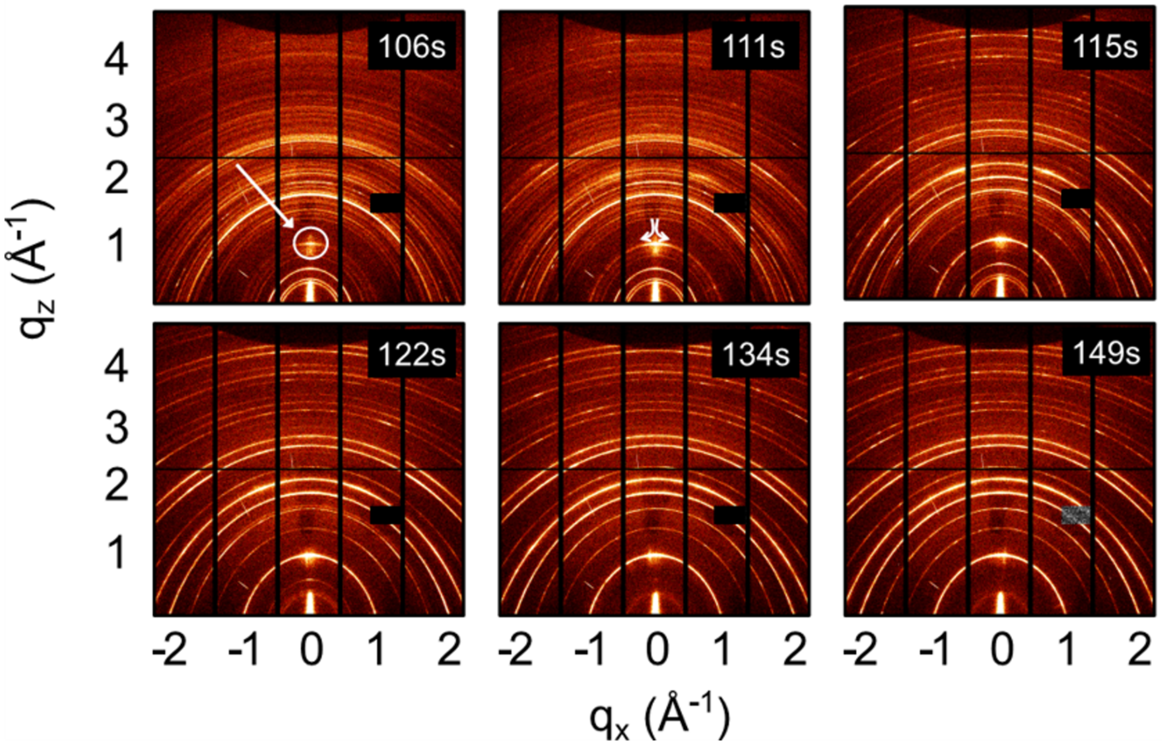

Figure 6.8: 2D GIWAXS data showcasing the growth of the $MAPbI_{3100}$ plane at q 1Å^{-1} with initial face-on preferred orientation (106 s), with other crystalline orientations growing with increased annealing (111 s). Corresponding decrease of intensity from Bragg peaks of $MAPbI_3 \cdot$ DMSO solvent-complex at q 0.7 Å^{-1}, with orientations away from the normal lose intensity faster (115, 134 s) until complete solvent removal (149 s).

the peak maximum is more significant, reaching 1.72 eV at t = 103 s. In parallel, the peak width decreases from 180 meV (t = 103 s) to 130 meV (t = 114 s) (Figure 6.10). After the peak width attains a local minimum (t = 114s), a subsequent re-broadening to 158 meV (t = 135 s) is observed, correlated to a small peak position shift towards higher energies. These trends reflect the dissolution and creation of small clusters with higher bandgap, as the solvent from the deeper parts are removed, confirming the X-ray diffraction data. The final phase IV (t $>$ 144 s) represents exclusive diffraction signals from cubic $MAPbI_3$ at q = 1.00 Å^{-1}, 1.42 Å^{-1}, 1.74 Å^{-1}, 2.00 Å^{-1}, 2.24 Å^{-1}, 2.46 Å^{-1}, 2.84 Å^{-1}, 3.01 Å^{-1} and 3.48 Å^{-1}. In this phase, the intensity of the perovskite peak increases (Figure 6.5) up to 260 s, while the peak width narrows (Figure 6.6), suggesting enhanced crystallinity and reduced lattice strain on longer annealing. The Bragg peak intensity distribution suggests a similar slight preferred orientation of the crystals of the thin film normal to the plane of the substrate, as is observed within the transient

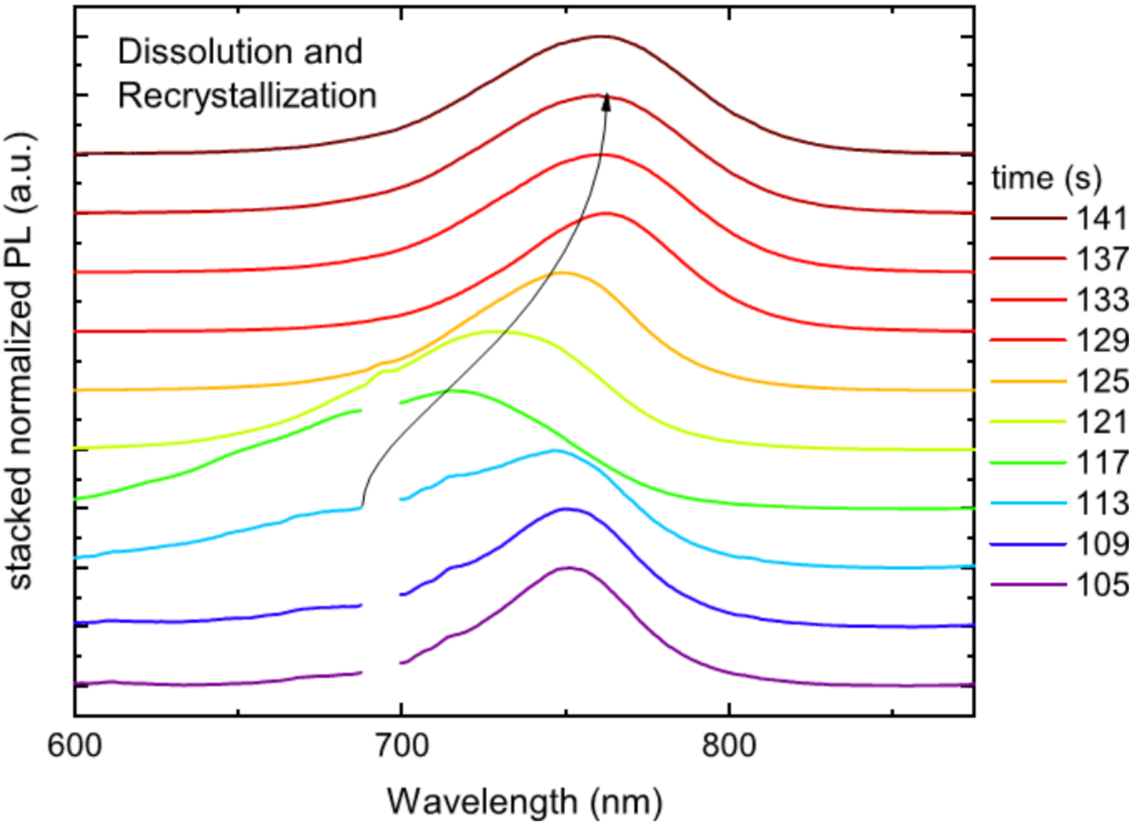

Figure 6.9: Normalized PL data during thermal disassociation of $MAPbI_3 \cdot DMSO$ solvent-complex and crystallization of $MAPbI_3$ on thermal annealing at 100°C

structure (Figure 6.3b) when the antisolvent is dispensed. Beyond 260 s, the peak intensity of the perovskite decreases slightly (Figure 6.6) as the peak width saw a slight increase, which might be indicative of the onset of beam damage. No PbI_2 is isolated although the perovskite peak broadening signifies increased disorder in crystals.

In phase IV, the gradual increase in the overall PL intensities is accompanied by a FWHM narrowing and shift in peak position towards 780 nm (1.60 eV), representative of luminescence from a stabilized bulk $MAPbI_3$ (Figure 6.10). PL data however did not indicate beam damage.

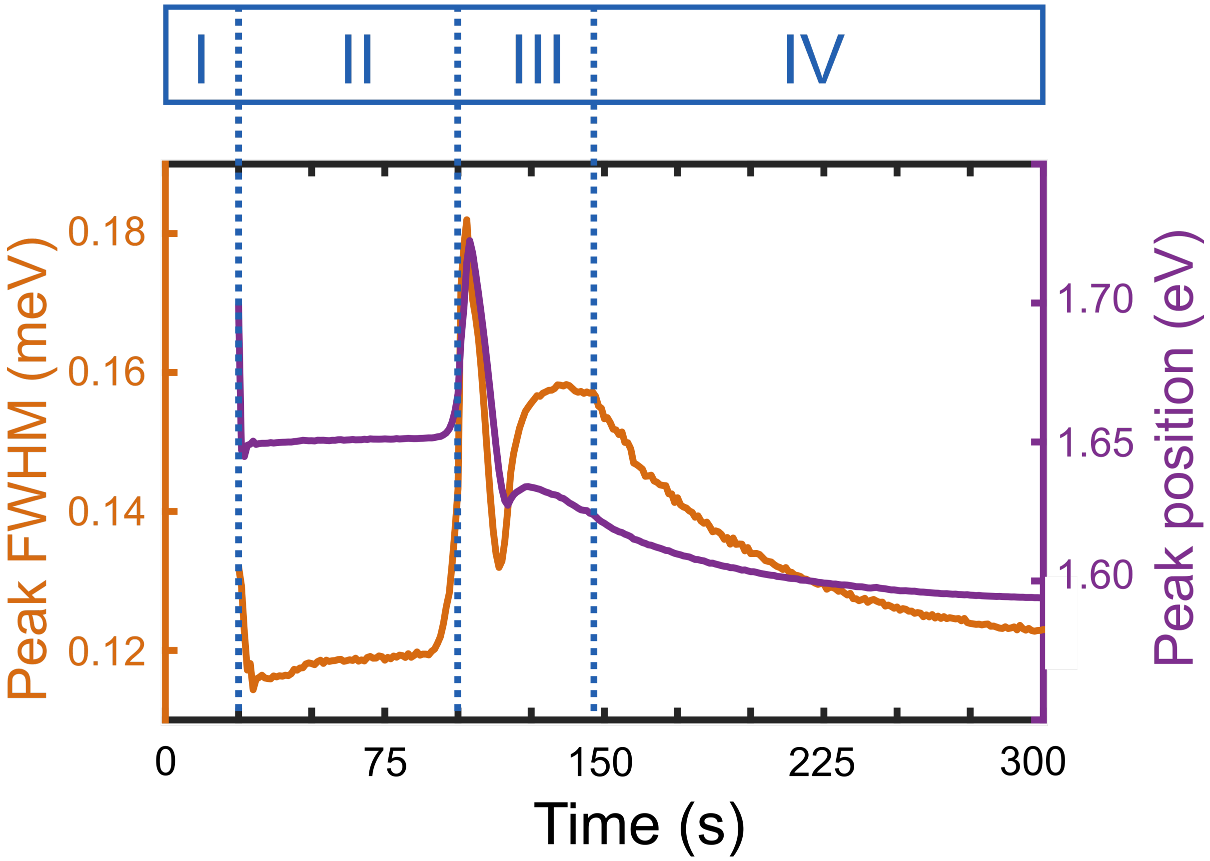

Figure 6.10: Temporal evolution of PL peak parameters during crystallization experiment

6.3 Physicochemical processes occuring during crystallization

While there are several reports on phase transformations and identification [135, 157–159], detailed insights into the phenomena occurring at critical synthesis and phase transition stages are desirable. Importantly, the kinetic processes occurring during nucleation and dissolution-recrystallization have not been revealed in detail so far, and are the focus of the present study (Figure 6.11).

Within the context of crystallization of colloidal systems from solutions, the crystallization processes are known to proceed by fluctuating solvodynamics resulting in initial low-amplitude, long-wavelength density fluctuations [160, 161] through a large volume, followed by the actual crystallization event. These fluctuations may be reflected in our diffraction data right before the emergence of the weak Bragg reflections from the supersaturated phase when the scattering signal shows an intermediate transition from colloidal halos at q = 0.5 Å^{-1}, 1.8 Å^{-1} and 3.0 Å^{-1} to a

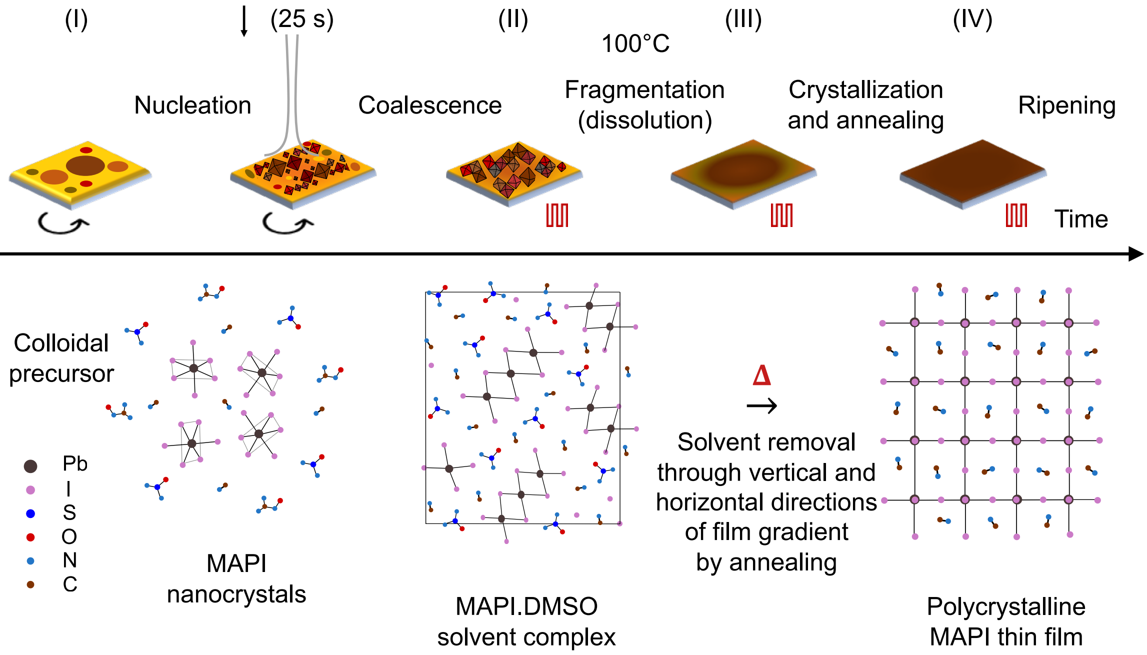

Figure 6.11: Phase I: The thin film consists of colloidal precursor of photoinactive solid precursors (PbI2 and CH_3NH_3I) and liquid solvents $(CH_3)_2N\text{-}HCO$ and $(CH_3)_2SO$. Nucleation of $MAPbI_3$ nanocrystals and conversion to phase II where the nanoparticles trimerize into thermodynamically stable orthorhombic solvent-complex of $Pb_3I_8.2(CH_3)_2SO.2CH_3NH_3$ with remainders of stable perovskite phase formed during nucleation. Phase III: Thermal decomposition of solvent-complex leading to removal of plumboiodide coordinated solvent molecules at 100°C from the thin film and the eventual dissolution-recrystallization of $CH_3NH_3PbI_3$ from the film thickness. Phase IV: Perovskite crystallization complete and thermal ripening process of the thin film.

broad background signal at the moment the antisolvent is dropped to initiate the crystallization process. Chemically, by virtue of the high miscibility of chlorobenzene with DMSO and DMF [40] and its poor solubility with the perovskite solid precursors, a phase separation process occurs as excess solvent molecules are displaced from the sample by the antisolvent stream, ensuing a marked increase in the concentration of the solute species within the system creating the conditions for a phase transition process to transpire. This phase transformation process which marks the phase boundary between the fluid colloidal precursor to the gel intermediate state can proceed by one of two routes, namely LaMer nucleation [162–164] or kinetically arrested spinodal decomposition [165]. Both processes signify pathways of segregation and evolution of a new phase [166] from a melt, where nucleation driven phase transitions have an associated activation energy for the creation of metastable nuclei, which coalesce to form the solvent-complex intermediate. A kinetically arrested spinodal decomposition process leads to the spontaneous formation of the said intermediate without the creation of metastable nuclei due to fluctuations in the energetics of the precursor. The impact of varying the antisolvent drop time during spin-coating strongly affects the material conversion pathways and resulting morphologies. Previous studies have extensively studied the impact of drop times and formulated and explained the concept of antisolvent drop time windows in separate studies [151, 158, 167].

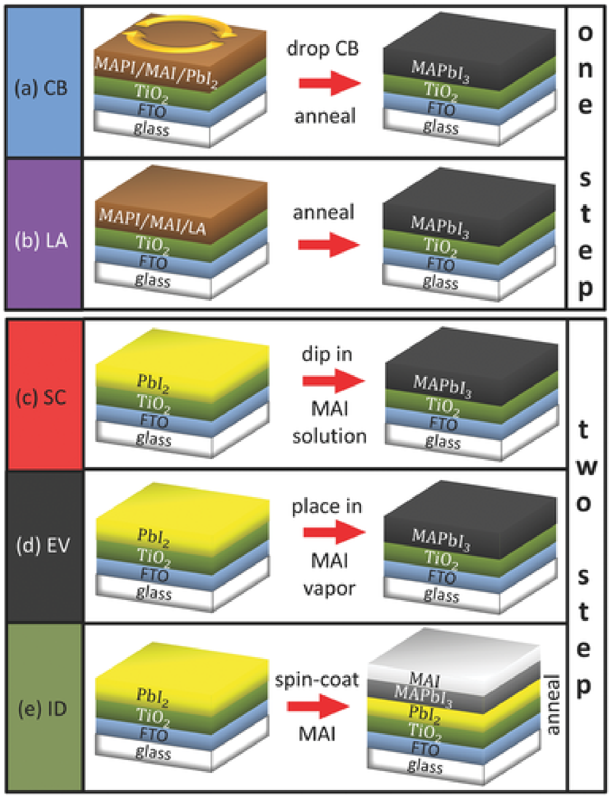

Figure 6.12: Schematic pathways of conversion of precursors by one step and two step transformation methods. In one step methods, organic and inorganic precursors are combined and deposited onto a substrate with further treatment. In two step methods, an inorganic film is converted to perovskite by reaction with organic precursor externally. Reprinted from [62] with permission from John Wiley and Sons.

In the absence of an antisolvent, materials crystallizing out of a fluid precursor nucleate and crystallize in a broad time window, whereas the application of an orthogonal solvent is a physical route to temporally regulate supersaturation and initiate growth during material crystallization/formation. Accordingly, there are distinct differences in precursor chemistry and methods of physicochemical conversion between a one-step [40] and two-step [157, 168] method which are typically discussed in literature. The one-step method combines the organic (CH_3NH_3I) and inorganic precursors (PbI_2) in a solvent system (4:1v:v DMF:DMSO) to afford a single colloidal precursor. This precursor is spin coated into a thin film, followed by an application of an antisolvent and subsequent thermal annealing to result in a $CH_3NH_3PbI_3$ film. The two-step method proceeds via the separated treatment of the inorganic (PbI_2) precursor solution processed into a thin film with suitable organic solvents (GBL, DMF, DMSO), immersed into an organic precursor (CH_3NH_3I/isopropanol) to convert to $CH_3NH_3PbI_3$ via a thermal annealing driven interdiffusion method. The removal of the bulk solvent molecules is expected to lead to a drastic reduction in the excluded free volume available for the solute molecules and cause a pinned gel-like structure [135, 165] with decreased diffusion abilities. The stochastic nature [160, 169] of nucleation of the perovskite precursor colloid [18, 106], where a broad distribution of nuclei sizes are expected at supersaturation, is reflected in the evolution of the PL FWHM. Whereas antisolvent driven nucleation is expected to lead to a homogenous nucleation event, experiments suggest that the actual nature of nucleation depends on the time window employed for antisolvent dispensing [151]. In our experiments, for the employed experimental conditions, an event resulting in a broad distribution of nanoparticles is marked, as witnessed by the broad photoluminescence signal. Such a signal implies a broad distribution in the density of states of luminescing species, which corroborate a distribution in the nuclei sizes formed during nucleation.

It is to be noted that this is the first observation of the pre-nucleation density fluctuations, as depicted in Figure 6.13 and nucleation as depicted in Figure 6.3 within crystallizing perovskite systems by combined diffraction and photoluminescence data. The nuclei are notably isostructural with the perovskite ($MAPbI_3$) phase but owing to the large destabilizing surface and interfacial energies associated, the diffraction data of the nucleated phase is only briefly observed Figure 6.3b before converting to the solvent-complex phase as depicted in Figure 6.3c. The nucleating species likely have high surface charge, and cluster-aggregation of individual monomers (${PbI_6}^{4-}$) to the trimerized orthogonal solvent-complex (${Pb_3I_8}^{2-}$)

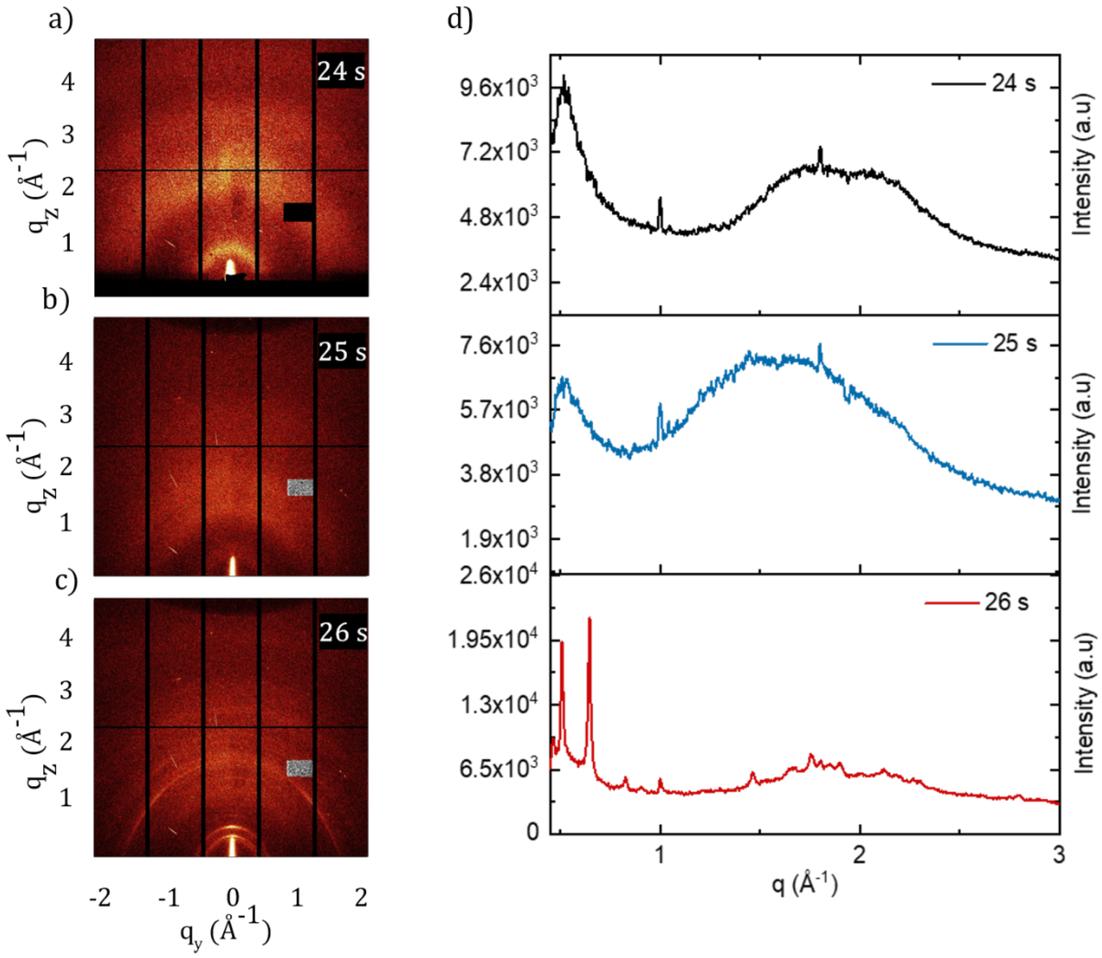

Figure 6.13: 2D GIWAXS data showing crystallization events of (a) the precursor colloid prior to drop of antisolvent, (b) solvodynamic, long-wavelength fluctuations in precursor resulting in changes in colloidal background intensity, (c) resulting in the direct formation of $MAPbI_3 \cdot DMSO$ solvent complex (d) radially integrated 2D GIWAXS data of events involved during $MAPbI_3$ crystallization by spinodal decomposition

proceeds by means of increased entropy [170] (and reduced free energy) on release of solvating molecules during the post-nucleation, early-growth stages. The DMSO molecules coordinate the trimerized aggregates, while the organic methylammonium ($CH_3NH_3^+$) are known to characteristically direct the self-assembly [171,172] of the structures resulting in the denser solvent-complex. The PL intensity is found to be influenced by two major factors: the nucleation density (total amount of perovskite material responding to the photo excitation) and the extent of radiative recombination (depending on crystal quality and defect density [151, 173]). The data supports the reduction in the polydispersity soon after the instance of nucleation by the growth in average particle size, as reflected within the narrowed shape of the PL peak and its red shift from 730 nm to 750 nm. The PL intensity during antisolvent-induced nucleation increases ($t = 25 - 27$ s), in agreement with previous reports [151] and is ascribed to an increasing number of nanocrystallites [148, 151]. Subsequently, the intensity is quenched (30x) due to cluster coalescence; also reflected within the PL red-shift. The coalesced clusters have reduced emission [174] as compared to the nucleated nanoparticles because with size increase, structures have a higher probability for non-radiative recombinations at defect sites and grain boundaries. A combination of increased crystallite size and thermal quenching lead to an increase in the extent of non-radiative recombination and a resultant reduction in the luminescence intensity from the remaining stable $MAPbI_3$ crystals formed during nucleation [148, 173]. The thermodynamic stability of the DMSO-complexated phase requires sample annealing to drive the removal of the DMSO molecules. The reduced free solvent content within the film is associated with the limited diffusion ability of the media, until the energy barrier is overcome by heating the sample. Throughout the annealing process, the nature of the diffraction and photoluminescence signals remain largely unchanged, until 100°C is reached and the disintegration process of the solvent complex is initiated, marking a subsequent second order phase transition. During thermal disassociation of the $MAPbI_3 \cdot DMSO$ solvent complex, the diffraction intensities from the solvent-complex diminish as the diffraction intensity of the perovskite phase gains in intensity (Figure 6.6). While the diffraction data reveals the two coexistent phases as they evolve, marking the second order of the phase transition, the PL data yields mechanistic insights underlying the transition. The disassociation of the solvent-complex leads to removal of DMSO by evaporation, leaving behind fragmented building blocks of the crystallizing $MAPbI_3$ phase. This process is deemed responsible for the increased polydispersity of the molecular species, reflected in the broadened and markedly blue shifted PL signal during phase III. Owing to the increased surface energies of the disassociated particles, the fragments thermally diffuse to form longer chains to reduce the total free energy of the system. This process of concatenation of plumboiodide fragments and their assembly within crystalline cubic perovskite lattice are reflected by shifts in the PL signal. The PL signal after its previous broadening and blue shift, undergoes rapid narrowing and red shifts as solvent molecules are rapidly removed from the thin film leaving

$MAPbI_3$ crystals behind. It has been found that owing to differential solvent evaporation rates from the film-air interface and the deeper entrenched solvent moieties, the film develops a vertical gradient of solvent distribution resulting in a crystallizing front leading from the film-air interface into the film-substrate interface, creating a crust of crystallized perovskite at the surface [175]. The processes occurring during annealing and drying can be distinguished into distinct drying stages, with considerations of heat and mass-transfer phenomena [176]. After the initiation of the annealing step in phase II, the temperature of the substrate increases linearly over time and by a heat-transfer process, the temperature of the thin film increases. In contrast, during phase III, the temperature is kept constant and the thermal disintegration of the solvent-complex allows significant evaporation of the solvent to the air interface. The solvent removal falls within the “fast” regime [177] and is strongly affected by the coupled heat and mass transfer between the drying film interface and air. The process of solvent removal proceeds by diffusion and evaporation and therefore includes advective mass transfer through the bulk. The removal of the solvent molecules underneath the film-air interface is responsible for the secondary processes beyond 120 s, where both the PL and the diffraction peaks show fluctuations in intensity due to subsequent redissolution and crystallization within different depths and interfaces. Phase IV of the process of crystallization is marked by the full conversion of the solvent complex into the $MAPbI_3$ structure, with all structural and optoelectronic signatures of the complex disappearing, signifying the completion of the crystallization process.

6.4 Summary

Methylammonium lead iodide thin films are processed by spin coating. In the first phase, a colloidal mixture of the solvent and solute molecules is observed in the diffraction data. The colloidal state does not show any photoluminescence. On drop of the antisolvent, perovskite nanoparticles are formed which are observed through a diffraction pattern with Bragg rings concordant with the structure of $MAPbI_3$. Moreover, photoluminescence displays a broad peak centred at 730 nm signifying the distribution of size of the formed $MAPbI_3$ nanoparticles. The formed nanoparticles are unstable owing to associated interfacial and surface energies. This leads to a cluster coalescence of the formed nanoparticles into a trimerized solvent-complex phase in the second phase. Photoluminescence data face a red shift and peak width narrowing due to the process of coalescence and size homogenization. The solvent-complex has an orthorhombic structure evidenced through diffraction and no photoluminescence. It is found stable to thermal annealing until a temperature of 100°C. At 100°C, the third phase of the process is reached wherein the solvent-complex begins to disassociate leading to the formation of smaller fragments that cause the emergence of a second photoluminescence signal between 650 nm and 740 nm. Diffraction data show the emergence of a growing $MAPbI_3$ signal and a weakening solvent-complex signal. Fluctuations in the diffraction and photoluminescence data arise due to dissolution-recrystallization processes which lead to disorder in the film. At the end of the experiment, in the fourth phase, the transformation of the solvent complex to perovskite is completed and the crystalline perovskite thin film undergoes a riperning process.

7 Conclusion and outlook

The behavior of colloidal perovskite precursors and thin films is investigated. The perovskite materials consists of organic and inorganic components dispersed in organic, polar solvents like DMF, DMSO in fluid precursor state. Systematic studies regarding how compositional engineering by partial/ complete replacement of chemical groups affects the key material properties in precursors is investigated. Further, the impact of changing concentration of the said precursors on the dispersion properties is under focus. Moreover, the impact of changing composition on the optical and morphological properties in thin films is demonstrated. In addition, the out of equilibrium processes occurring during the fabrication of thin films from complex colloidal precursors is investigated with the aid of a multimodal analytical cell via spin coating.

Perovskite based materials feature highly versatile crystallographic and electronic structure and therefore, provide a high level of functionality. While this versatility is the basis of continuously increasing number of optoelectronic applications, it is also accompanied by a massive complexity of the material. The structural and optoelectronic properties of mixed halide perovskites colloidal precursor dispersions are investigated in order to improve the understanding of the chemical and physical nature of perovskite sols. The study is of relevance since in many cases the formation of thin perovskite films is based on solution-processing using precursors, being prepared under representative conditions as those utilized within the present study. Prevalent protocols utilize chemical tailoring of precursors, which are demonstrated to possess polydisperse structural species of varying chemical compositions. The study probes the growth of structural species in dispersions and identifies the emergence of different structural complexes and their evolution from nanocrystals to growing complex aggregates. With increasing concentration, we observe four stages of growing structures, which affect the thin film morphology: (I) nanoparticles, (II) increasing size of nanoparticles, (III) formation of large aggregates/ complex clusters and (IV) fragmentation of large aggregates. The study suggests that mixed halide perovskites colloidal dispersions bear precursors of their individual parent compounds. Thin films based on colloidal precursors grow at the expense of the very structural entities present within these dispersions. Structural inhomogeneities have been linked to variations in photovoltaic performances and bear direct relevance in the case of functional devices. The origin of structural and possibly chemical heterogeneities within thin films may very well be correlated to the structures prevalent within the dynamic fluid phase and underlines the need for a better understanding of the non-trivial perovskite precursors.

Intermixing of precursors in the gives rise to alloyed structures which are formulated into thin films. The alloyed materials display distinct structural and optical characteristics. Spin coated thin films showcase the emergence of hierarchical mesoscale and microstructures. Such behavior is attributed to the self-organization of the complex nanoscale colloidal precursors as a response to instabilities. These instabilities are caused by the evolution of tensile and compressive stress gradients during film drying and annealing. The topological and crystallographic structures are shown to be tunable by facile chemical engineering of perovskite alloys, and give rise to anisotropy of crystalline lattice planes. Such physicochemical behaviour markedly presents an intrinsic technological opportunity to engineer the morphology and topology of hybrid perovskite thin films.

The combination of in situ photoluminescence and X-ray diffraction is used to follow in real time the colloidal processing of perovskite thin films during spin coating. Multimodal experimental observation of the structure and optoelectronic properties of the luminescent, metastable nuclei of $CH_3NH_3PbI_3$ nanoparticles during processing are observed. These nucleated building-blocks are tracked in real-time as they are transformed into the orthogonal solvent-complex $Pb_3I_8.2(CH_3)_2SO.2CH_3NH_3$. During annealing, the solvent-complex disintegrates, and a solvent gradient is established through the thin film leading to a redissolution-recrystallization and rearrangement process throughout the film thickness. The final phase of $CH_3NH_3PbI_3$ is stabilized in the cubic symmetry and exhibits the expected structural and optoelectronic characteristics.

Based on the work, it would be interesting to observe the growth processes occuring for solid solutions of hybrid perovskites to observe the sequential nucleation and growth processes of different chemical species involved. It is expected that while I-rich precursors would lead to the formation of solvent complexes, Br-bearing precursors are expected to crystallize straight from nanoparticles into crystalline thin films. This would help explain the emergence of crystalline preferred orientations in thin films *in situ*. Tuning the morphology by the utilization of antisolvents within different drop time windows would alter the structure-property relationship of crystallizing perovskites. Analyzing these properties for mixed halide and mixed perovskite precursors would present insight onto the role of the cationic species in thin films. The evolution of structural and optoelectronic properties and their correlation to temperature would help establish a deeper understanding of processes of temperature and light-induced phase segregation, which is a key phenomena in mixed perovskites. Further, the mapping of hierarchical structures by experiments such as nanodiffraction would help visualize domains of locally segregated perovskite structures of mixed perovskite compositions. This would help develop an accurate understanding of decomposition processes of hybrid perovskites and provide diagnostic tools for the stabilization of structures.

Bibliography

[1] IEA, “Key world energy statistics: https://www.iea.org/reports/key-world-energy-statistics-2020,” 2020.

[2] NREL, “Best research-cell efficiency chart: https://www.nrel.gov/pv/cell-efficiency.html,” 2021.

[3] D. Weber, “$CH_3NH_3PbX_3$, ein Pb(II)-System mit kubischer Perowskitstruktur / $CH_3NH_3PbX_3$, a Pb(II)-System with Cubic Perovskite Structure,” *Zeitschrift für Naturforschung B*, vol. 33, no. 12, pp. 1443–1445, 1978.

[4] D. B. Mitzi, C. A. Feild, W. T. A. Harrison, and A. M. Guloy, “Conducting tin halides with a layered organic-based perovskite structure,” *Nature*, vol. 369, no. 6480, pp. 467–469, 1994.

[5] J. M. Frost, K. T. Butler, and A. Walsh, “Molecular ferroelectric contributions to anomalous hysteresis in hybrid perovskite solar cells,” *APL Materials*, vol. 2, no. 8, p. 081506, 2014.

[6] S. Sil, H. Luitel, J. Dhar, M. Chakrabarti, P. P. Ray, B. Bandyopadhyay, and D. Sanyal, “Defect induced room temperature ferromagnetism in methylammonium lead iodide perovskite,” *Physics Letters A*, vol. 384, no. 14, p. 126278, 2020.

[7] Y.-J. Kim, T.-V. Dang, H.-J. Choi, B.-J. Park, J.-H. Eom, H.-A. Song, D. Seol, Y. Kim, S.-H. Shin, J. Nah, and S.-G. Yoon, “Piezoelectric properties of $CH_3NH_3PbI_3$ perovskite thin films and their applications in piezoelectric generators,” *J. Mater. Chem. A*, vol. 4, pp. 756–763, 2016.

[8] E. Sedov, I. Sedova, S. Arakelian, G. Eramo, and A. Kavokin, “Hybrid optical fiber for light-induced superconductivity,” *Scientific Reports*, vol. 10, May 2020.

[9] C. C. Stoumpos, C. D. Malliakas, and M. G. Kanatzidis, "Semiconducting tin and lead iodide perovskites with organic cations: Phase transitions, high mobilities, and near-infrared photoluminescent properties," *Inorganic Chemistry*, vol. 52, no. 15, pp. 9019–9038, 2013.

[10] A. Kojima, K. Teshima, Y. Shirai, and T. Miyasaka, "Organometal halide perovskites as visible-light sensitizers for photovoltaic cells," *Journal of the American Chemical Society*, vol. 131, no. 17, pp. 6050–6051, 2009.

[11] J. Jeong, M. Kim, J. Seo, H. Lu, P. Ahlawat, A. Mishra, Y. Yang, M. A. Hope, F. T. Eickemeyer, M. Kim, Y. J. Yoon, I. W. Choi, B. P. Darwich, S. J. Choi, Y. Jo, J. H. Lee, B. Walker, S. M. Zakeeruddin, L. Emsley, U. Rothlisberger, A. Hagfeldt, D. S. Kim, M. Grätzel, and J. Y. Kim, "Pseudo-halide anion engineering for α-FAPbI$_3$ perovskite solar cells," *Nature*, vol. 592, pp. 381–385, Apr. 2021.

[12] J. Gong, S. B. Darling, and F. You, "Perovskite photovoltaics: life-cycle assessment of energy and environmental impacts," *Energy Environ. Sci.*, vol. 8, pp. 1953–1968, 2015.

[13] A. Binek, M. L. Petrus, N. Huber, H. Bristow, Y. Hu, T. Bein, and P. Docampo, "Recycling perovskite solar cells to avoid lead waste," *ACS Applied Materials & Interfaces*, vol. 8, no. 20, pp. 12881–12886, 2016.

[14] A. Priyadarshi, L. J. Haur, P. Murray, D. Fu, S. Kulkarni, G. Xing, T. C. Sum, N. Mathews, and S. G. Mhaisalkar, "A large area (70 cm^2) monolithic perovskite solar module with a high efficiency and stability," *Energy Environ. Sci.*, vol. 9, pp. 3687–3692, 2016.

[15] Z. Song, C. L. McElvany, A. B. Phillips, I. Celik, P. W. Krantz, S. C. Watthage, G. K. Liyanage, D. Apul, and M. J. Heben, "A technoeconomic analysis of perovskite solar module manufacturing with low-cost materials and techniques," *Energy & Environmental Science*, vol. 10, no. 6, pp. 1297–1305, 2017.

[16] F. Di Giacomo, A. Fakharuddin, R. Jose, and T. M. Brown, "Progress, challenges and perspectives in flexible perovskite solar cells," *Energy Environ. Sci.*, vol. 9, pp. 3007–3035, 2016.

[17] E. M. Tennyson, T. A. S. Doherty, and S. D. Stranks, “Heterogeneity at multiple length scales in halide perovskite semiconductors,” *Nature Reviews Materials*, vol. 44, no. 7762, p. 1251, 2019.

[18] S. Pratap, E. Keller, and P. Müller-Buschbaum, “Emergence of lead halide perovskite colloidal dispersions through aggregation and fragmentation: insights from the nanoscale to the mesoscale,” *Nanoscale*, vol. 11, no. 8, pp. 3495–3499, 2019.

[19] S. Pratap, N. Tamura, C. Stan, Z. Yuan, H. Goudey, A. MacDowell, T.-B. Song, N. Barchi, P. Müller-Buschbaum, C. Sutter-Fella, and J. Slack, “Probing the in situ dynamics of structure–property evolution in hybrid perovskite thin films spincoated from complex fluids by a custom-designed beamline-compatible multimodal measurement chamber,” *Acta Crystallographica Section A Foundations and Advances*, vol. 75, no. a1, pp. a155–a156, 2019.

[20] S. Pratap, J. Schlipf, L. Bießmann, and P. Müller-Buschbaum, “Hierarchical structures from nanocrystalline colloidal precursors within hybrid perovskite thin films: Implications for photovoltaics,” *ACS Applied Nano Materials*, vol. 3, no. 12, pp. 11701–11708, 2020.

[21] D. B. Mitzi, S. Wang, C. A. Feild, C. A. Chess, and A. M. Guloy, “Conducting layered organic-inorganic halides containing 110-oriented perovskite sheets,” *Science*, vol. 267, pp. 1473–1476, Mar. 1995.

[22] K. Liang, D. B. Mitzi, and M. T. Prikas, “Synthesis and characterization of organic-inorganic perovskite thin films prepared using a versatile two-step dipping technique,” *Chemistry of Materials*, vol. 10, pp. 403–411, Jan. 1998.

[23] K. D. Karlin, ed., *Progress in Inorganic Chemistry.* John Wiley & Sons, Inc., Jan. 1999.

[24] M. Grätzel, “The light and shade of perovskite solar cells,” *Nature Materials*, vol. 13, no. 9, pp. 838–842, 2014.

[25] V. M. Goldschmidt, “Die gesetze der krystallochemie,” *Die Naturwissenschaften*, vol. 14, pp. 477–485, May 1926.

[26] I. E. Castelli, J. M. García-Lastra, K. S. Thygesen, and K. W. Jacobsen, "Bandgap calculations and trends of organometal halide perovskites," *APL Materials*, vol. 2, no. 8, p. 081514, 2014.

[27] J. Even, L. Pedesseau, J.-M. Jancu, and C. Katan, "Importance of spin–orbit coupling in hybrid organic/inorganic perovskites for photovoltaic applications," *The Journal of Physical Chemistry Letters*, vol. 4, no. 17, pp. 2999–3005, 2013.

[28] N. N. Lal, Y. Dkhissi, W. Li, Q. Hou, Y.-B. Cheng, and U. Bach, "Perovskite tandem solar cells," *Advanced Energy Materials*, vol. 7, no. 18, p. 1602761, 2017.

[29] M. M. Lee, J. Teuscher, T. Miyasaka, T. N. Murakami, and H. J. Snaith, "Efficient hybrid solar cells based on meso-superstructured organometal halide perovskites," *Science (New York, N.Y.)*, vol. 338, no. 6107, pp. 643–647, 2012.

[30] F. Brivio, A. B. Walker, and A. Walsh, "Structural and electronic properties of hybrid perovskites for high-efficiency thin-film photovoltaics from first-principles," *APL Materials*, vol. 1, no. 4, p. 042111, 2013.

[31] W.-J. Yin, T. Shi, and Y. Yan, "Unique properties of halide perovskites as possible origins of the superior solar cell performance," *Advanced Materials*, vol. 26, pp. 4653–4658, May 2014.

[32] G. Giorgi, J.-I. Fujisawa, H. Segawa, and K. Yamashita, "Small photocarrier effective masses featuring ambipolar transport in methylammonium lead iodide perovskite: A density functional analysis," *The Journal of Physical Chemistry Letters*, vol. 4, pp. 4213–4216, Nov. 2013.

[33] S. de Wolf, J. Holovsky, S.-J. Moon, P. Löper, B. Niesen, M. Ledinsky, F.-J. Haug, J.-H. Yum, and C. Ballif, "Organometallic halide perovskites: Sharp optical absorption edge and its relation to photovoltaic performance," *The Journal of Physical Chemistry Letters*, vol. 5, no. 6, pp. 1035–1039, 2014.

[34] W.-J. Yin, T. Shi, and Y. Yan, "Unusual defect physics in $CH_3NH_3PbI_3$ perovskite solar cell absorber," *Applied Physics Letters*, vol. 104, no. 6, p. 063903, 2014.

[35] J. Berry, T. Buonassisi, D. A. Egger, G. Hodes, L. Kronik, Y.-L. Loo, I. Lubomirsky, S. R. Marder, Y. Mastai, J. S. Miller, D. B. Mitzi, Y. Paz, A. M. Rappe, I. Riess, B. Rybtchinski, O. Stafsudd, V. Stevanovic, M. F. Toney, D. Zitoun, A. Kahn, D. Ginley, and D. Cahen, "Hybrid organic-inorganic perovskites (HOIPs): Opportunities and challenges," *Advanced Materials*, vol. 27, pp. 5102–5112, July 2015.

[36] S. D. Stranks, G. E. Eperon, G. Grancini, C. Menelaou, M. J. P. Alcocer, T. Leijtens, L. M. Herz, A. Petrozza, and H. J. Snaith, "Electron-hole diffusion lengths exceeding 1 micrometer in an organometal trihalide perovskite absorber," *Science*, vol. 342, pp. 341–344, Oct. 2013.

[37] Q. Dong, Y. Fang, Y. Shao, P. Mulligan, J. Qiu, L. Cao, and J. Huang, "Electron-hole diffusion lengths $> 175\ \mu$m in solution-grown $CH_3NH_3PbI_3$ single crystals," *Science*, vol. 347, pp. 967–970, Jan. 2015.

[38] W. Gao, X. Gao, T. A. Abtew, Y.-Y. Sun, S. Zhang, and P. Zhang, "Quasiparticle band gap of organic-inorganic hybrid perovskites: Crystal structure, spin-orbit coupling, and self-energy effects," *Physical Review B*, vol. 93, no. 8, 2016.

[39] B. Li, M. Li, C. Fei, G. Cao, and J. Tian, "Colloidal engineering for monolayer $CH_3NH_3PbI_3$ films toward high performance perovskite solar cells," *Journal of Materials Chemistry A*, vol. 5, no. 46, pp. 24168–24177, 2017.

[40] N. J. Jeon, J. H. Noh, Y. C. Kim, W. S. Yang, S. Ryu, and S. I. Seok, "Solvent engineering for high-performance inorganic-organic hybrid perovskite solar cells," *Nature Materials*, vol. 13, no. 9, pp. 897–903, 2014.

[41] K. Yan, M. Long, T. Zhang, Z. Wei, H. Chen, S. Yang, and J. Xu, "Hybrid halide perovskite solar cell precursors: Colloidal chemistry and coordination engineering behind device processing for high efficiency," *Journal of the American Chemical Society*, vol. 137, no. 13, pp. 4460–4468, 2015.

[42] J. Burschka, N. Pellet, S.-J. Moon, R. Humphry-Baker, P. Gao, M. K. Nazeeruddin, and M. Grätzel, "Sequential deposition as a route to high-performance perovskite-sensitized solar cells," *Nature*, vol. 499, pp. 316–319, July 2013.

[43] J. Qiu, Y. Qiu, K. Yan, M. Zhong, C. Mu, H. Yan, and S. Yang, "All-solid-state hybrid solar cells based on a new organometal halide perovskite sensitizer and one-dimensional TiO_2 nanowire arrays," *Nanoscale*, vol. 5, pp. 3245–3248, 2013.

[44] J. M. Ball, M. M. Lee, A. Hey, and H. J. Snaith, "Low-temperature processed meso-superstructured to thin-film perovskite solar cells," *Energy & Environmental Science*, vol. 6, no. 6, p. 1739, 2013.

[45] J. J. de Yoreo, P. U. P. A. Gilbert, N. A. J. M. Sommerdijk, R. L. Penn, S. Whitelam, D. Joester, H. Zhang, J. D. Rimer, A. Navrotsky, J. F. Banfield, A. F. Wallace, F. M. Michel, F. C. Meldrum, H. Cölfen, and P. M. Dove, "Crystallization by particle attachment in synthetic, biogenic, and geologic environments," *Science (New York, N.Y.)*, vol. 349, no. 6247, p. aaa6760, 2015.

[46] N. Pellet, J. Teuscher, J. Maier, and M. Grätzel, "Transforming hybrid organic inorganic perovskites by rapid halide exchange," *Chemistry of Materials*, vol. 27, no. 6, pp. 2181–2188, 2015.

[47] M. Saliba, T. Matsui, J.-Y. Seo, K. Domanski, J.-P. Correa-Baena, M. K. Nazeeruddin, S. M. Zakeeruddin, W. Tress, A. Abate, A. Hagfeldt, and M. Grätzel, "Cesium-containing triple cation perovskite solar cells: improved stability, reproducibility and high efficiency," *Energy & Environmental Science*, vol. 9, no. 6, pp. 1989–1997, 2016.

[48] D. Bi, W. Tress, M. I. Dar, P. Gao, J. Luo, C. Renevier, K. Schenk, A. Abate, F. Giordano, J.-P. Correa Baena, J.-D. Decoppet, S. M. Zakeeruddin, M. K. Nazeeruddin, M. Grätzel, and A. Hagfeldt, "Efficient luminescent solar cells based on tailored mixed-cation perovskites," *Science Advances*, vol. 2, no. 1, p. e1501170, 2016.

[49] H. Zhu, Y. Fu, F. Meng, X. Wu, Z. Gong, Q. Ding, M. V. Gustafsson, M. T. Trinh, S. Jin, and X.-Y. Zhu, "Lead halide perovskite nanowire lasers with low lasing thresholds and high quality factors," *Nature Materials*, vol. 14, no. 6, pp. 636–642, 2015.

[50] B. J. Foley, J. Girard, B. A. Sorenson, A. Z. Chen, J. Scott Niezgoda, M. R. Alpert, A. F. Harper, D.-M. Smilgies, P. Clancy, W. A. Saidi, and J. J. Choi, "Controlling nucleation, growth, and orientation of metal halide perovskite thin films with rationally selected additives," *Journal of Materials Chemistry A*, vol. 5, no. 1, pp. 113–123, 2017.

[51] Y. Zhou, O. S. Game, S. Pang, and N. P. Padture, "Microstructures of organometal trihalide perovskites for solar cells: Their evolution from solutions and characterization," *The Journal of Physical Chemistry Letters*, vol. 6, no. 23, pp. 4827–4839, 2015.

[52] W. Zhang, M. Saliba, D. T. Moore, S. K. Pathak, M. T. Hörantner, T. Stergiopoulos, S. D. Stranks, G. E. Eperon, J. A. Alexander-Webber, A. Abate, A. Sadhanala, S. Yao, Y. Chen, R. H. Friend, L. A. Estroff, U. Wiesner, and H. J. Snaith, "Ultrasmooth organic-inorganic perovskite thin-film formation and crystallization for efficient planar heterojunction solar cells," *Nature Communications*, vol. 6, no. 1, p. 6142, 2015.

[53] Y. C. Zheng, S. Yang, X. Chen, Y. Chen, Y. Hou, and H. G. Yang, "Thermal-induced volmer–weber growth behavior for planar heterojunction perovskites solar cells," *Chemistry of Materials*, vol. 27, pp. 5116–5121, July 2015.

[54] J. A. Venables, G. D. T. Spiller, and M. Hanbucken, "Nucleation and growth of thin films," *Reports on Progress in Physics*, vol. 47, pp. 399–459, apr 1984.

[55] Agilent technologies, "The basics of UV-Vis spectrophotometry: https://thornseshold.cup.uni-muenchen.de/site/assets/files/1068/agilent_uv-vis_basics-primer_en.pdf."

[56] P. M. Carvalho, M. R. Felício, N. C. Santos, S. Gonçalves, and M. M. Domingues, "Application of light scattering techniques to nanoparticle characterization and development," *Frontiers in Chemistry*, vol. 6, June 2018.

[57] J. Schlipf and P. Müller-Buschbaum, "Structure of organometal halide perovskite films as determined with grazing-incidence x-ray scattering methods," *Advanced Energy Materials*, vol. 7, no. 16, p. 1700131, 2017.

[58] Z. Jiang, “Gixsgui : a matlab toolbox for grazing-incidence x-ray scattering data visualization and reduction, and indexing of buried three-dimensional periodic nanostructured films,” *Journal of Applied Crystallography*, vol. 48, no. 3, pp. 917–926, 2015.

[59] L. C. Schmidt, A. Pertegás, S. González-Carrero, O. Malinkiewicz, S. Agouram, G. Mínguez Espallargas, H. J. Bolink, R. E. Galian, and J. Pérez-Prieto, “Nontemplate synthesis of $CH_3NH_3PbBr_3$ perovskite nanoparticles,” *Journal of the American Chemical Society*, vol. 136, no. 3, pp. 850–853, 2014.

[60] Q. A. Akkerman, G. Rainò, M. V. Kovalenko, and L. Manna, “Genesis, challenges and opportunities for colloidal lead halide perovskite nanocrystals,” *Nature Materials*, vol. 17, no. 5, p. 394, 2018.

[61] Y. Zhao, H. Tan, H. Yuan, Z. Yang, J. Z. Fan, J. Kim, O. Voznyy, X. Gong, L. N. Quan, C. S. Tan, J. Hofkens, D. Yu, Q. Zhao, and E. H. Sargent, “Perovskite seeding growth of formamidinium-lead-iodide-based perovskites for efficient and stable solar cells,” *Nature Communications*, vol. 9, no. 1, p. 1607, 2018.

[62] L. Oesinghaus, J. Schlipf, N. Giesbrecht, L. Song, Y. Hu, T. Bein, P. Docampo, and P. Müller-Buschbaum, “Toward tailored film morphologies: The origin of crystal orientation in hybrid perovskite thin films,” *Advanced Materials Interfaces*, vol. 3, no. 19, p. 1600403, 2016.

[63] D. Vlassopoulos and M. Cloitre, “Bridging the gap between hard and soft colloids,” *Soft Matter*, vol. 8, no. 15, p. 4010, 2012.

[64] N. T. K. Thanh, N. Maclean, and S. Mahiddine, “Mechanisms of nucleation and growth of nanoparticles in solution,” *Chemical Reviews*, vol. 114, no. 15, pp. 7610–7630, 2014.

[65] E. Keller, “High efficiency perovskite solar cells,” *Technische Universität München*, vol. Bachelor thesis, 2018.

[66] K. G. Stamplecoskie, J. S. Manser, and P. V. Kamat, “Dual nature of the excited state in organic–inorganic lead halide perovskites,” *Energy & Environmental Science*, vol. 8, no. 1, pp. 208–215, 2015.

[67] F. Ginot, I. Theurkauff, F. Detcheverry, C. Ybert, and C. Cottin-Bizonne, “Aggregation-fragmentation and individual dynamics of active clusters,” *Nature Communications*, vol. 9, no. 1, p. 696, 2018.

[68] A. Zöttl and H. Stark, “Emergent behavior in active colloids,” *Journal of Physics: Condensed Matter*, vol. 28, no. 25, p. 253001, 2016.

[69] V. N. Manoharan, “Colloids. colloidal matter: Packing, geometry, and entropy,” *Science (New York, N.Y.)*, vol. 349, no. 6251, p. 1253751, 2015.

[70] J. Wang, L. Zhao, M. Wang, and S. Lin, “Molecular insights into early nuclei and interfacial mismatch during vapor deposition of hybrid perovskites on titanium dioxide substrate,” *Crystal Growth & Design*, vol. 17, no. 12, pp. 6201–6211, 2017.

[71] A. Sharenko, C. Mackeen, L. Jewell, F. Bridges, and M. F. Toney, “Evolution of iodoplumbate complexes in methylammonium lead iodide perovskite precursor solutions,” *Chemistry of Materials*, vol. 29, no. 3, pp. 1315–1320, 2017.

[72] R. Ganapathy, M. R. Buckley, S. J. Gerbode, and I. Cohen, “Direct measurements of island growth and step-edge barriers in colloidal epitaxy,” *Science (New York, N.Y.)*, vol. 327, no. 5964, pp. 445–448, 2010.

[73] A. Malins, S. R. Williams, J. Eggers, H. Tanaka, and C. P. Royall, “Geometric frustration in small colloidal clusters,” *Journal of physics. Condensed matter : an Institute of Physics journal*, vol. 21, no. 42, p. 425103, 2009.

[74] Y. M. Harshe and M. Lattuada, “Breakage rate of colloidal aggregates in shear flow through stokesian dynamics,” *Langmuir : the ACS journal of surfaces and colloids*, vol. 28, no. 1, pp. 283–292, 2012.

[75] L. K. Reb, M. Böhmer, B. Predeschly, S. Grott, C. L. Weindl, G. I. Ivandekic, R. Guo, C. Dreißigacker, R. Gernhäuser, A. Meyer, and P. Müller-Buschbaum, “Perovskite and organic solar cells on a rocket flight,” *Joule*, vol. 4, no. 9, pp. 1880–1892, 2020.

[76] J. Jean and P. R. Brown, *Emerging Photovoltaic Technologies.* 2053-2563, IOP Publishing, 2020.

[77] T. W. Kim, S. Uchida, T. Matsushita, L. Cojocaru, R. Jono, K. Kimura, D. Matsubara, M. Shirai, K. Ito, H. Matsumoto, T. Kondo, and H. Segawa, "Self-organized superlattice and phase coexistence inside thin film organometal halide perovskite," *Advanced Materials*, vol. 30, no. 8, 2018.

[78] J. M. Frost, K. T. Butler, F. Brivio, C. H. Hendon, M. van Schilfgaarde, and A. Walsh, "Atomistic origins of high-performance in hybrid halide perovskite solar cells," *Nano Letters*, vol. 14, no. 5, pp. 2584–2590, 2014.

[79] W.-J. Yin, T. Shi, and Y. Yan, "Unique properties of halide perovskites as possible origins of the superior solar cell performance," *Advanced Materials*, vol. 26, no. 27, pp. 4653–4658, 2014.

[80] D. Shi, V. Adinolfi, R. Comin, M. Yuan, E. Alarousu, A. Buin, Y. Chen, S. Hoogland, A. Rothenberger, K. Katsiev, Y. Losovyj, X. Zhang, P. A. Dowben, O. F. Mohammed, E. H. Sargent, and O. M. Bakr, "Solar cells. low trap-state density and long carrier diffusion in organolead trihalide perovskite single crystals," *Science (New York, N.Y.)*, vol. 347, no. 6221, pp. 519–522, 2015.

[81] L. M. Pazos-Outón, M. Szumilo, R. Lamboll, J. M. Richter, M. Crespo-Quesada, M. Abdi-Jalebi, H. J. Beeson, M. Vrućinić, M. Alsari, H. J. Snaith, B. Ehrler, R. H. Friend, and F. Deschler, "Photon recycling in lead iodide perovskite solar cells," *Science (New York, N.Y.)*, vol. 351, no. 6280, pp. 1430–1433, 2016.

[82] J. S. Manser, J. A. Christians, and P. V. Kamat, "Intriguing optoelectronic properties of metal halide perovskites," *Chemical Reviews*, vol. 116, no. 21, pp. 12956–13008, 2016.

[83] V. Adinolfi, W. Peng, G. Walters, O. M. Bakr, and E. H. Sargent, "The electrical and optical properties of organometal halide perovskites relevant to optoelectronic performance," *Advanced Materials*, vol. 30, no. 1, 2018.

[84] J. M. Frost and A. Walsh, "What is moving in hybrid halide perovskite solar cells?," *Accounts of Chemical Research*, vol. 49, no. 3, pp. 528–535, 2016.

[85] H. Liu, C.-J. Liang, H.-M. Zhang, M.-J. Sun, J.-J. Liang, X.-W. Zhang, C. Ji, Z.-B. Guo, Y.-J. Xu, and Z.-Q. He, "Effects of surface morphology on the ionic capacitance and performance of perovskite solar cells," *Japanese Journal of Applied Physics*, vol. 56, no. 9, p. 090305, 2017.

[86] W. Tress, N. Marinova, T. Moehl, S. M. Zakeeruddin, M. K. Nazeeruddin, and M. Grätzel, "Understanding the rate-dependent J–V hysteresis, slow time component, and aging in $CH_3NH_3PbI_3$ perovskite solar cells: the role of a compensated electric field," *Energy & Environmental Science*, vol. 8, no. 3, pp. 995–1004, 2015.

[87] D. W. deQuilettes, W. Zhang, V. M. Burlakov, D. J. Graham, T. Leijtens, A. Osherov, V. Bulović, H. J. Snaith, D. S. Ginger, and S. D. Stranks, "Photo-induced halide redistribution in organic-inorganic perovskite films," *Nature Communications*, vol. 7, p. 11683, 2016.

[88] E. T. Hoke, D. J. Slotcavage, E. R. Dohner, A. R. Bowring, H. I. Karunadasa, and M. D. McGehee, "Reversible photo-induced trap formation in mixed-halide hybrid perovskites for photovoltaics," *Chemical science*, vol. 6, no. 1, pp. 613–617, 2015.

[89] Y. Yuan and J. Huang, "Ion migration in organometal trihalide perovskite and its impact on photovoltaic efficiency and stability," *Accounts of Chemical Research*, vol. 49, no. 2, pp. 286–293, 2016.

[90] D. Niesner, M. Wilhelm, I. Levchuk, A. Osvet, S. Shrestha, M. Batentschuk, C. Brabec, and T. Fauster, "Giant Rashba Splitting in $CH_3NH_3PbBr_3$ Organic-Inorganic Perovskite," *Physical Review Letters*, vol. 117, no. 12, p. 126401, 2016.

[91] H. J. Snaith, A. Abate, J. M. Ball, G. E. Eperon, T. Leijtens, N. K. Noel, S. D. Stranks, J. T.-W. Wang, K. Wojciechowski, and W. Zhang, "Anomalous hysteresis in perovskite solar cells," *The Journal of Physical Chemistry Letters*, vol. 5, no. 9, pp. 1511–1515, 2014.

[92] Z. Li, M. Yang, J.-S. Park, S.-H. Wei, J. J. Berry, and K. Zhu, "Stabilizing perovskite structures by tuning tolerance factor: Formation of formamidinium and cesium lead iodide solid-state alloys," *Chemistry of Materials*, vol. 28, no. 1, pp. 284–292, 2016.

[93] T. Jesper Jacobsson, J.-P. Correa-Baena, M. Pazoki, M. Saliba, K. Schenk, M. Grätzel, and A. Hagfeldt, "Exploration of the compositional space for mixed lead halogen perovskites for high efficiency solar cells," *Energy & Environmental Science*, vol. 9, no. 5, pp. 1706–1724, 2016.

[94] T. Baikie, Y. Fang, J. M. Kadro, M. Schreyer, F. Wei, S. G. Mhaisalkar, M. Graetzel, and T. J. White, "Synthesis and crystal chemistry of the hybrid perovskite $CH_3NH_3PbI_3$ for solid-state sensitised solar cell applications," *Journal of Materials Chemistry A*, vol. 1, no. 18, p. 5628, 2013.

[95] P. S. Whitfield, N. Herron, W. E. Guise, K. Page, Y. Q. Cheng, I. Milas, and M. K. Crawford, "Structures, phase transitions and tricritical behavior of the hybrid perovskite methyl ammonium lead iodide," *Scientific Reports*, vol. 6, p. 35685, 2016.

[96] L. Vegard, "Die konstitution der mischkristalle und die raumfllung der atome," *Zeitschrift fr Physik*, vol. 5, no. 1, pp. 17–26, 1921.

[97] V. D'Innocenzo, A. R. Srimath Kandada, M. de Bastiani, M. Gandini, and A. Petrozza, "Tuning the light emission properties by band gap engineering in hybrid lead halide perovskite," *Journal of the American Chemical Society*, vol. 136, no. 51, pp. 17730–17733, 2014.

[98] P. Kim, M. Abkarian, and H. A. Stone, "Hierarchical folding of elastic membranes under biaxial compressive stress," *Nature Materials*, vol. 10, no. 12, pp. 952–957, 2011.

[99] P. M. Reis, "Thin films: Folded in hierarchy," *Nature Materials*, vol. 10, no. 12, pp. 907–909, 2011.

[100] S. Y. Leblebici, L. Leppert, Y. Li, S. E. Reyes-Lillo, S. Wickenburg, E. Wong, J. Lee, M. Melli, D. Ziegler, D. K. Angell, D. F. Ogletree, P. D. Ashby, F. M. Toma, J. B. Neaton, I. D. Sharp, and A. Weber-Bargioni, "Facet-dependent photovoltaic efficiency variations in single grains of hybrid halide perovskite," *Nature Energy*, vol. 1, no. 8, p. 16093, 2016.

[101] J.-H. Im, H.-S. Kim, and N.-G. Park, "Morphology-photovoltaic property correlation in perovskite solar cells: One-step versus two-step deposition of $CH_3NH_3PbI_3$," *APL Materials*, vol. 2, no. 8, p. 081510, 2014.

[102] Y. Kutes, Y. Zhou, J. L. Bosse, J. Steffes, N. P. Padture, and B. D. Huey, "Mapping the Photoresponse of $CH_3NH_3PbI_3$ Hybrid Perovskite Thin Films at the Nanoscale," *Nano Letters*, vol. 16, no. 6, pp. 3434–3441, 2016.

[103] D. Moerman, G. E. Eperon, J. T. Precht, and D. S. Ginger, "Correlating photoluminescence heterogeneity with local electronic properties in methylammonium lead tribromide perovskite thin films," *Chemistry of Materials*, vol. 29, no. 13, pp. 5484–5492, 2017.

[104] Y. Li, L. Ji, R. Liu, C. Zhang, C. H. Mak, X. Zou, H.-H. Shen, S.-Y. Leu, and H.-Y. Hsu, "A review on morphology engineering for highly efficient and stable hybrid perovskite solar cells," *Journal of Materials Chemistry A*, vol. 6, no. 27, pp. 12842–12875, 2018.

[105] D. P. McMeekin, Z. Wang, W. Rehman, F. Pulvirenti, J. B. Patel, N. K. Noel, M. B. Johnston, S. R. Marder, L. M. Herz, and H. J. Snaith, "Crystallization kinetics and morphology control of formamidinium-cesium mixed-cation lead mixed-halide perovskite via tunability of the colloidal precursor solution," *Advanced Materials*, vol. 29, no. 29, 2017.

[106] N. S. Dutta, N. K. Noel, and C. B. Arnold, "Crystalline nature of colloids in methylammonium lead halide perovskite precursor inks revealed by cryo-electron microscopy," *The Journal of Physical Chemistry Letters*, pp. 5980–5986, 2020.

[107] L. Goehring, R. Conroy, A. Akhter, W. J. Clegg, and A. F. Routh, "Evolution of mud-crack patterns during repeated drying cycles," *Soft Matter*, vol. 6, no. 15, p. 3562, 2010.

[108] I. M. Hermes, S. A. Bretschneider, V. W. Bergmann, D. Li, A. Klasen, J. Mars, W. Tremel, F. Laquai, H.-J. Butt, M. Mezger, R. Berger, B. J. Rodriguez, and S. A. L. Weber, “Ferroelastic fingerprints in methylammonium lead iodide perovskite,” *The Journal of Physical Chemistry C*, vol. 120, no. 10, pp. 5724–5731, 2016.

[109] M. U. Rothmann, W. Li, Y. Zhu, U. Bach, L. Spiccia, J. Etheridge, and Y.-B. Cheng, “Direct observation of intrinsic twin domains in tetragonal $CH_3NH_3PbI_3$,” *Nature Communications*, vol. 8, p. 14547, 2017.

[110] A. Hexemer and P. Müller-Buschbaum, “Advanced grazing-incidence techniques for modern soft-matter materials analysis,” *IUCrJ*, vol. 2, no. Pt 1, pp. 106–125, 2015.

[111] A. Wang, J. Huang, and Y. Yan, “Hierarchical molecular self-assemblies: construction and advantages,” *Soft Matter*, vol. 10, no. 19, pp. 3362–3373, 2014.

[112] J. S. Bangsund, T. R. Fielitz, T. J. Steiner, K. Shi, J. R. van Sambeek, C. P. Clark, and R. J. Holmes, “Formation of aligned periodic patterns during the crystallization of organic semiconductor thin films,” *Nature Materials*, vol. 18, no. 7, pp. 725–731, 2019.

[113] R. Mukherjee and A. Sharma, “Instability, self-organization and pattern formation in thin soft films,” *Soft Matter*, vol. 11, no. 45, pp. 8717–8740, 2015.

[114] A. C. Ferreira, A. Létoublon, S. Paofai, S. Raymond, C. Ecolivet, B. Rufflé, S. Cordier, C. Katan, M. I. Saidaminov, A. A. Zhumekenov, O. M. Bakr, J. Even, and P. Bourges, “Elastic softness of hybrid lead halide perovskites,” *Physical Review Letters*, vol. 121, no. 8, p. 085502, 2018.

[115] M. A. Boles, M. Engel, and D. V. Talapin, “Self-assembly of colloidal nanocrystals: From intricate structures to functional materials,” *Chemical Reviews*, vol. 116, no. 18, pp. 11220–11289, 2016.

[116] J.-W. Lee, H.-S. Kim, and N.-G. Park, “Lewis acid-base adduct approach for high efficiency perovskite solar cells,” *Accounts of Chemical Research*, vol. 49, no. 2, pp. 311–319, 2016.

[117] J. R. Trantum, M. L. Baglia, Z. E. Eagleton, R. L. Mernaugh, and F. R. Haselton, “Biosensor design based on marangoni flow in an evaporating drop,” *Lab on a chip*, vol. 14, no. 2, pp. 315–324, 2014.

[118] L. Pauchard and C. Allain, “Stable and unstable surface evolution during the drying of a polymer solution drop,” *Physical review. E, Statistical, nonlinear, and soft matter physics*, vol. 68, no. 5 Pt 1, p. 052801, 2003.

[119] H. Ishihara, S. Sarang, Y.-C. Chen, O. Lin, P. Phummirat, L. Thung, J. Hernandez, S. Ghosh, and V. Tung, “Nature inspiring processing route toward high throughput production of perovskite photovoltaics,” *Journal of Materials Chemistry A*, vol. 4, no. 18, pp. 6989–6997, 2016.

[120] K. A. Bush, N. Rolston, A. Gold-Parker, S. Manzoor, J. Hausele, Z. J. Yu, J. A. Raiford, R. Cheacharoen, Z. C. Holman, M. F. Toney, R. H. Dauskardt, and M. D. McGehee, “Controlling thin-film stress and wrinkling during perovskite film formation,” *ACS Energy Letters*, vol. 3, no. 6, pp. 1225–1232, 2018.

[121] G. H. Gilmer, H. Huang, T. D. de La Rubia, J. Dalla Torre, and F. Baumann, “Lattice monte carlo models of thin film deposition,” *Thin Solid Films*, vol. 365, no. 2, pp. 189–200, 2000.

[122] R. Brighenti, A. Spagnoli, A. Carpinteri, and F. Artoni, “Defect tolerance in soft materials,” *Procedia Structural Integrity*, vol. 2, 2016.

[123] A. Arango-Restrepo, D. Barragán, and J. M. Rubi, “Self-assembling outside equilibrium: emergence of structures mediated by dissipation,” *Physical Chemistry Chemical Physics*, vol. 21, no. 32, pp. 17475–17493, 2019.

[124] A. van der Drift, “Evolutionary selection, a principle governing growth orientation in vapour-deposited layers,” *Philips Res. Repts*, vol. 22, pp. 267–288.

[125] A. Z. Chen, M. Shiu, J. H. Ma, M. R. Alpert, D. Zhang, B. J. Foley, D.-M. Smilgies, S.-H. Lee, and J. J. Choi, “Origin of vertical orientation in two-dimensional metal halide perovskites and its effect on photovoltaic performance,” *Nature Communications*, vol. 9, no. 1, p. 1336.

[126] S. D. Stranks, R. L. Z. Hoye, D. Di, R. H. Friend, and F. Deschler, "The physics of light emission in halide perovskite devices," *Advanced Materials*, vol. 31, no. 47, p. e1803336, 2019.

[127] W. A. Dunlap-Shohl, Y. Zhou, N. P. Padture, and D. B. Mitzi, "Synthetic approaches for halide perovskite thin films," *Chemical Reviews*, vol. 119, no. 5, pp. 3193–3295, 2019.

[128] X. Zhou, Y. Zhang, W. Kong, M. Hu, L. Zhang, C. Liu, X. Li, C. Pan, G. Yu, C. Cheng, and B. Xu, "Crystallization manipulation and morphology evolution for highly efficient perovskite solar cell fabrication via hydration water induced intermediate phase formation under heat assisted spin-coating," *Journal of Materials Chemistry A*, vol. 6, no. 7, pp. 3012–3021, 2018.

[129] P.-W. Liang, C.-Y. Liao, C.-C. Chueh, F. Zuo, S. T. Williams, X.-K. Xin, J. Lin, and A. K.-Y. Jen, "Additive enhanced crystallization of solution-processed perovskite for highly efficient planar-heterojunction solar cells," *Advanced Materials*, vol. 26, no. 22, pp. 3748–3754, 2014.

[130] W. S. Yang, J. H. Noh, N. J. Jeon, Y. C. Kim, S. Ryu, J. Seo, and S. I. Seok, "Solar cells. high-performance photovoltaic perovskite layers fabricated through intramolecular exchange," *Science (New York, N.Y.)*, vol. 348, no. 6240, pp. 1234–1237, 2015.

[131] G. E. Eperon, S. D. Stranks, C. Menelaou, M. B. Johnston, L. M. Herz, and H. J. Snaith, "Formamidinium lead trihalide: a broadly tunable perovskite for efficient planar heterojunction solar cells," *Energy & Environmental Science*, vol. 7, no. 3, pp. 982–988, 2014.

[132] C. M. Sutter-Fella, "The value of watching how materials grow: A multimodal case study on halide perovskites," *Advanced Energy Materials*, p. 2003534, 2021.

[133] K. Binder and P. Fratzl, "Spinodal decomposition," in *Phase transformations in materials* (G. Kostorz, ed.), pp. 409–480, Weinheim and New York and Chichester: Wiley-VCH, 2010.

[134] J. Schlipf, L. Bießmann, L. Oesinghaus, E. Berger, E. Metwalli, J. A. Lercher, L. Porcar, and P. Müller-Buschbaum, "In situ monitoring the uptake of moisture into hybrid perovskite thin films," *The Journal of Physical Chemistry Letters*, vol. 9, no. 8, pp. 2015–2021, 2018.

[135] K. Wang, M.-C. Tang, H. X. Dang, R. Munir, D. Barrit, M. de Bastiani, E. Aydin, D.-M. Smilgies, S. de Wolf, and A. Amassian, "Kinetic stabilization of the sol-gel state in perovskites enables facile processing of high-efficiency solar cells," *Advanced Materials*, vol. 31, no. 32, p. e1808357, 2019.

[136] Q. Hu, L. Zhao, J. Wu, K. Gao, D. Luo, Y. Jiang, Z. Zhang, C. Zhu, E. Schaible, A. Hexemer, C. Wang, Y. Liu, W. Zhang, M. Grätzel, F. Liu, T. P. Russell, R. Zhu, and Q. Gong, "In situ dynamic observations of perovskite crystallisation and microstructure evolution intermediated from ${PbI_6}^{4-}$ cage nanoparticles," *Nature Communications*, vol. 8, p. 15688.

[137] M. Qin, K. Tse, T.-K. Lau, Y. Li, C.-J. Su, G. Yang, J. Chen, J. Zhu, U.-S. Jeng, G. Li, H. Chen, and X. Lu, "Manipulating the mixed-perovskite crystallization pathway unveiled by in situ giwaxs," *Advanced Materials*, vol. 31, no. 25, p. e1901284, 2019.

[138] J. Cao, X. Jing, J. Yan, C. Hu, R. Chen, J. Yin, J. Li, and N. Zheng, "Identifying the molecular structures of intermediates for optimizing the fabrication of high-quality perovskite films," *Journal of the American Chemical Society*, vol. 138, no. 31, pp. 9919–9926, 2016.

[139] Y. Guo, K. Shoyama, W. Sato, Y. Matsuo, K. Inoue, K. Harano, C. Liu, H. Tanaka, and E. Nakamura, "Chemical pathways connecting lead(ii) iodide and perovskite via polymeric plumbate(ii) fiber," *Journal of the American Chemical Society*, vol. 137, no. 50, pp. 15907–15914, 2015.

[140] Y. Rong, Z. Tang, Y. Zhao, X. Zhong, S. Venkatesan, H. Graham, M. Patton, Y. Jing, A. M. Guloy, and Y. Yao, "Solvent engineering towards controlled grain growth in perovskite planar heterojunction solar cells," *Nanoscale*, vol. 7, no. 24, pp. 10595–10599, 2015.

[141] H. X. Dang, K. Wang, M. Ghasemi, M.-C. Tang, M. de Bastiani, E. Aydin, E. Dauzon, D. Barrit, J. Peng, D.-M. Smilgies, S. de Wolf, and A. Amassian, “Multi-cation synergy suppresses phase segregation in mixed-halide perovskites,” *Joule*, vol. 3, no. 7, pp. 1746–1764, 2019.

[142] J. C. Hamill, J. Schwartz, and Y.-L. Loo, “Influence of solvent coordination on hybrid organic–inorganic perovskite formation,” *ACS Energy Letters*, vol. 3, no. 1, pp. 92–97, 2018.

[143] H. Zhang, M. K. Nazeeruddin, and W. C. H. Choy, “Perovskite photovoltaics: The significant role of ligands in film formation, passivation, and stability,” *Advanced Materials*, vol. 31, no. 8, p. e1805702, 2019.

[144] T. H. Gfroerer, *Photoluminescence in Analysis of Surfaces and Interfaces.* Encyclopedia of Analytical Chemistry, American Cancer Society, 2006.

[145] T. Unold and L. Gütay, “Photoluminescence analysis of thin-film solar cells,” in *Advanced characterization techniques for thin film solar cells* (D. Abou-Ras, T. Kirchartz, and J. Rau, eds.), pp. 275–297, Weinheim: Wiley-VCH, 2016 Wiley-VCH Verlag Weinheim.

[146] E. S. Parrott, J. B. Patel, A.-A. Haghighirad, H. J. Snaith, M. B. Johnston, and L. M. Herz, “Growth modes and quantum confinement in ultrathin vapour-deposited $\mathrm{MAPbI_3}$ films,” *Nanoscale*, vol. 11, no. 30, pp. 14276–14284, 2019.

[147] W. Nie, H. Tsai, R. Asadpour, J.-C. Blancon, A. J. Neukirch, G. Gupta, J. J. Crochet, M. Chhowalla, S. Tretiak, M. A. Alam, H.-L. Wang, and A. D. Mohite, “Solar cells. high-efficiency solution-processed perovskite solar cells with millimeter-scale grains,” *Science (New York, N.Y.)*, vol. 347, no. 6221, pp. 522–525, 2015.

[148] L. Wagner, L. E. Mundt, G. Mathiazhagan, M. Mundus, M. C. Schubert, S. Mastroianni, U. Würfel, A. Hinsch, and S. W. Glunz, “Distinguishing crystallization stages and their influence on quantum efficiency during perovskite solar cell formation in real-time,” *Scientific Reports*, vol. 7, no. 1, p. 14899, 2017.

[149] M. Shirayama, H. Kadowaki, T. Miyadera, T. Sugita, M. Tamakoshi, M. Kato, T. Fujiseki, D. Murata, S. Hara, T. N. Murakami, S. Fujimoto, M. Chikamatsu, and H. Fujiwara, "Optical Transitions in Hybrid Perovskite Solar Cells: Ellipsometry, Density Functional Theory, and Quantum Efficiency Analyses for $CH_3NH_3PbI_3$," *Physical Review Applied*, vol. 5, no. 1, p. 014012, 2016.

[150] H. Fujiwara, M. Kato, M. Tamakoshi, T. Miyadera, and M. Chikamatsu, "Optical characteristics and operational principles of hybrid perovskite solar cells," *physica status solidi (a)*, vol. 215, no. 12, p. 1700730, 2018.

[151] T.-B. Song, Z. Yuan, F. Babbe, D. P. Nenon, E. Aydin, S. de Wolf, and C. M. Sutter-Fella, "Dynamics of antisolvent processed hybrid metal halide perovskites studied by in situ photoluminescence and its influence on optoelectronic properties," *ACS Applied Energy Materials*, vol. 3, no. 3, pp. 2386–2393, 2020.

[152] P. Meakin, "Models for colloidal aggregation," *Annual Review of Physical Chemistry*, vol. 39, no. 1, pp. 237–267, 1988.

[153] C. Schaefer, J. J. Michels, and P. van der Schoot, "Dynamic surface enrichment in drying thin-film binary polymer solutions," *Macromolecules*, vol. 50, no. 15, pp. 5914–5919, 2017.

[154] M. Tsige and G. S. Grest, "Solvent evaporation and interdiffusion in polymer films," *Journal of Physics: Condensed Matter*, vol. 17, no. 49, pp. S4119–S4132, 2005.

[155] M. P. Howard, W. F. Reinhart, T. Sanyal, M. S. Shell, A. Nikoubashman, and A. Z. Panagiotopoulos, "Evaporation-induced assembly of colloidal crystals," *The Journal of Chemical Physics*, vol. 149, no. 9, p. 094901, 2018.

[156] J. Li, A. Dobrovolsky, A. Merdasa, E. L. Unger, and I. G. Scheblykin, "Luminescent Intermediates and Humidity-Dependent Room-Temperature Conversion of the $MAPbI_3$ Perovskite Precursor," *ACS Omega*, vol. 3, no. 10, pp. 14494–14502, 2018.

[157] M. Chauhan, Y. Zhong, K. Schötz, B. Tripathi, A. Köhler, S. Huettner, and F. Panzer, "Investigating two-step $MAPbI_3$ thin film formation during spin coating by simultaneous in situ absorption and photoluminescence spectroscopy," *Journal of Materials Chemistry A*, vol. 8, no. 10, pp. 5086–5094, 2020.

[158] K. Bruening and C. J. Tassone, "Antisolvent processing of lead halide perovskite thin films studied by in situ x-ray diffraction," *Journal of Materials Chemistry A*, vol. 6, no. 39, pp. 18865–18870, 2018.

[159] L. E. Mundt and L. T. Schelhas, "Structural evolution during perovskite crystal formation and degradation: In situ and operando x–ray diffraction studies," *Advanced Energy Materials*, vol. 10, no. 26, p. 1903074, 2020.

[160] J. F. Lutsko, "A dynamical theory of nucleation for colloids and macromolecules," *The Journal of Chemical Physics*, vol. 136, no. 3, p. 034509, 2012.

[161] J. F. Lutsko and J. Lam, "Long-wavelength density fluctuations as nucleation precursors," *Physical Review E*, vol. 101, no. 5-1, p. 052122, 2020.

[162] V. K. LaMer and R. H. Dinegar, "Theory, production and mechanism of formation of monodispersed hydrosols," *Journal of the American Chemical Society*, vol. 72, no. 11, pp. 4847–4854, 1950.

[163] H. Hu, M. Singh, X. Wan, J. Tang, C.-W. Chu, and G. Li, "Nucleation and crystal growth control for scalable solution-processed organic–inorganic hybrid perovskite solar cells," *Journal of Materials Chemistry A*, vol. 8, no. 4, pp. 1578–1603, 2020.

[164] C. Liu, Y.-B. Cheng, and Z. Ge, "Understanding of perovskite crystal growth and film formation in scalable deposition processes," *Chemical Society reviews*, vol. 49, no. 6, pp. 1653–1687, 2020.

[165] T. Gibaud and P. Schurtenberger, "A closer look at arrested spinodal decomposition in protein solutions," *Journal of Physics: Condensed Matter*, vol. 21, no. 32, p. 322201, 2009.

[166] J. W. P. Schmelzer, A. S. Abyzov, and J. Möller, "Nucleation versus spinodal decomposition in phase formation processes in multicomponent solutions," *The Journal of Chemical Physics*, vol. 121, no. 14, pp. 6900–6917, 2004.

[167] P. Zhao, B. J. Kim, X. Ren, D. G. Lee, G. J. Bang, J. B. Jeon, W. B. Kim, and H. S. Jung, "Antisolvent with an ultrawide processing window for the one-step fabrication of efficient and large-area perovskite solar cells," *Advanced materials (Deerfield Beach, Fla.)*, vol. 30, no. 49, p. e1802763, 2018.

[168] Z. Xiao, C. Bi, Y. Shao, Q. Dong, Q. Wang, Y. Yuan, C. Wang, Y. Gao, and J. Huang, "Efficient, high yield perovskite photovoltaic devices grown by interdiffusion of solution-processed precursor stacking layers," *Energy & Environmental Science*, vol. 7, no. 8, pp. 2619–2623, 2014.

[169] J. F. Lutsko, "How crystals form: A theory of nucleation pathways," *Science Advances*, vol. 5, no. 4, p. eaav7399, 2019.

[170] W. J. E. M. Habraken, J. Tao, L. J. Brylka, H. Friedrich, L. Bertinetti, A. S. Schenk, A. Verch, V. Dmitrovic, P. H. H. Bomans, P. M. Frederik, J. Laven, P. van der Schoot, B. Aichmayer, G. de With, J. J. DeYoreo, and N. A. J. M. Sommerdijk, "Ion-association complexes unite classical and non-classical theories for the biomimetic nucleation of calcium phosphate," *Nature Communications*, vol. 4, no. 1, p. 1507, 2013.

[171] E. V. Shevchenko, D. V. Talapin, C. B. Murray, and S. O'Brien, "Structural characterization of self-assembled multifunctional binary nanoparticle superlattices," *Journal of the American Chemical Society*, vol. 128, no. 11, pp. 3620–3637, 2006.

[172] Raul F. Lobo, Stacey I. Zones, and Mark E. Davis, "Structure-direction in zeolite synthesis," *Journal of Inclusion Phenomena and Molecular Recognition in Chemistry*, vol. 21, no. 1, pp. 47–78, 1995.

[173] K. Suchan, J. Just, P. Becker, E. L. Unger, and T. Unold, "Optical in situ monitoring during the synthesis of halide perovskite solar cells reveals formation kinetics and evolution of optoelectronic properties," *Journal of Materials Chemistry A*, vol. 8, no. 20, pp. 10439–10449, 2020.

[174] A. van Dijken, J. Makkinje, and A. Meijerink, “The influence of particle size on the luminescence quantum efficiency of nanocrystalline zno particles,” *Journal of Luminescence*, vol. 92, no. 4, pp. 323–328, 2001.

[175] A. Z. Chen, M. Shiu, X. Deng, M. Mahmoud, D. Zhang, B. J. Foley, S.-H. Lee, G. Giri, and J. J. Choi, “Understanding the formation of vertical orientation in two-dimensional metal halide perovskite thin films,” *Chemistry of Materials*, vol. 31, no. 4, pp. 1336–1343, 2019.

[176] S. P. Velaga, D. Nikjoo, and P. R. Vuddanda, “Experimental studies and modeling of the drying kinetics of multicomponent polymer films,” *AAPS PharmSciTech*, vol. 19, no. 1, pp. 425–435, 2018.

[177] B. Guerrier, C. Bouchard, C. Allain, and C. Bénard, “Drying kinetics of polymer films,” *AIChE Journal*, vol. 44, no. 4, pp. 791–798, 1998.

List of publications

Publications related to the dissertation

- S. Pratap, F. Babbe, N. S. Barchi, Z. Yuan, T. Luong, Z. Haber, T.-B. Song, J. L. Slack, C. V. Stan, N. Tamura, C. M. Sutter-Fella, P. Müller-Buschbaum, ”Out-of-equilibrium processes in crystallization of organic-inorganic perovskites during spin coating”, *Nature Communications* accepted, (2021)
- S. Pratap, J. Schlipf, L. Bießmann, P. Müller-Buschbaum, ”Hierarchical Structures from Nanocrystalline Colloidal Precursors within Hybrid Perovskite Thin Films: Implications for Photovoltaics”, *ACS Applied Nano Materials* **3**, 12, 11701-11708 (2020)
- S. Pratap, N. Tamura, C. Stan, Z. Yuan, H. Goudey, A. MacDowell, T.-B. Song, N. Barchi, P. Müller-Buschbaum, C. Sutter-Fella, J. Slack, ”Probing the in situ dynamics of structure–property evolution in hybrid perovskite thin films spincoated from complex fluids by a custom-designed beamline-compatible multimodal measurement chamber”, *Acta Crystallographica Section A* A**75**, a155-a156 (2019)
- S. Pratap, E. Keller, P. Müller-Buschbaum, ”Emergence of lead halide perovskite colloidal dispersions through aggregation and fragmentation: insights from the nanoscale to the mesoscale”, *Nanoscale* **11**, 3495–3499 (2019)
- S. Pratap, N. Tamura, C. Stan, Z. Yuan, H. Goudey, A. MacDowell, T.-B. Song, N. Barchi, P. Müller-Buschbaum, C. Sutter-Fella, J. Slack, ”Pocket spin-coater : A synchrotron beamline compatible chamber for observing the in-situ evolution of processing-structure-property functionality in solution-processed thin films” in preparation

Further publications

- J. Schlipf, Y. Hu, S. Pratap, L. Bießmann, N. Hohn, L. Porcar, T. Bein, P. Docampo, P. Müller-Buschbaum ”Shedding light on the moisture stability of 3D/2D hybrid perovskite heterojunction thin films”, *ACS Applied Energy Materials* **2**, 2, 1011-1018 (2019)

Scientific reports

- S. Pratap, J. Schlipf, K. John, V. Korstgens, P. Weiser, A. Holleitner, A. Davydok, C. Krywka, P. Muller-Buschbaum, ”An insight into atmospheric degradation processes by mapping local nanoheterogeneities within hybrid polycrystalline perovskite films”, *Lehrstuhl für Funktionelle Materialien, Annual Report*, 2017.
- S. Pratap, E. Keller, P. Müller-Buschbaum, ”Emergence of lead halide perovskite colloidal dispersions through aggregation and fragmentation: insights from the nanoscale to the mesoscale through spectroscopic signatures”, *Lehrstuhl für Funktionelle Materialien, Annual Report*, 2018.
- S. Pratap, N. Tamura, C. Stan, Z. Yuan, H. Goudey, A. MacDowell, T.-B. Song, N. Barchi, P. Müller-Buschbaum, C. Sutter-Fella, J. Slack, ”Probing the in situ dynamics of structure–property evolution in hybrid perovskite thin films spincoated from complex fluids by a custom-designed beamline-compatible multimodal measurement chamber”, *Lehrstuhl für Funktionelle Materialien, Annual Report*, 2019.

Scientific talks

- S. Pratap, F. Babbe, N. S. Barchi, Z. Yuan, T. Luong, Z. Haber, T.-B. Song, J. L. Slack, C. V. Stan, N. Tamura, C. M. Sutter-Fella, P. Müller-Buschbaum
  Out-of-equilibrium processes during phase transitions: An in situ crystallization study of hybrid perovskites during spin coating
  DPG-Frühjahrstagung, Online mini-symposium, 23 Mar 2021

- S. Pratap
  Colloidal hybrid perovskites
  Seminar talk at the chair of functional materials, Physics Department, TU Munich, 16 Dec 2020

- S. Pratap, J. L. Slack
  A multimodal environment for understanding chemical processing and transformations at the microdiffraction beamline
  ALS Photon Science Group Meeting, Berkeley, 21 Feb 2019

- S. Pratap
  An introduction to the material class of hybrid perovskites for optoelectronic functionality
  Material Science Symposium, UC Berkeley, 21 Mar 2019

- S. Pratap
  In-situ structure-property evolution of hybrid perovskite thin films during spin-coating: A Swiss-knife point of view
  Seminar talk at the chair of functional materials, Physics Department, TU Munich, 26 Mar 2019

- S. Pratap, J. Schlipf, K. John, V. Korstgens, F. Fischer, S. Vema, A. Holleitner, A. Davydok, ¨ C. Krywka, P. Muller-Buschbaum
  On the colloidal behaviour of hybrid perovskite precursor dispersion and tracking structural heterogeneties arising from mixed perovskites: insights into the nano and macroscale
  DPG-Fruhjahrstagung, Regensburg, 31 Mar – 5 Apr 2019

- S. Pratap, J. Schlipf, L. Bießmann, P. Muller-Buschbaum
  On the Chemical Origins of Crystalline Preferred Orientations in Hybrid Perovskite Thin Films — Microstructures Revisited
  MRS Spring Meeting, Phoenix, 22 – 26 Apr 2019

- S. Pratap, N. Tamura, C. Stan, Z. Yuan, H. Gowdey, A. MacDowell, T. Song, N. Barchi, P. Muller-Buschbaum, C. Sutter-Fella, J. Slack
  Probing the in-situ dynamics of structure-property evolution in hybrid perovskite thin films spincoated from complex fluids by a custom designed, beamline compatible multimodal measurement chamber
  American Crystallography Association Annual Meeting, Covington, 20 – 24 Jul 2019

- S. Pratap, N. Tamura, C. Stan, Z. Yuan, H. Gowdey, A. MacDowell, T. Song, N. Barchi, P. Muller-Buschbaum, C. Sutter-Fella, J. Slack
  Probing the in-situ dynamics of structure-property evolution in hybrid perovskite solid solutions from complex fluids
  Molecular Foundry User Meeting, Berkeley Lab, 21 – 22 Aug 2019

- S. Pratap
  The fascinating world of soft materials - exploring hybrid perovskites
  Ginsberg Group Symposium, UC Berkeley, 23 Sep 2019

- S. Pratap
  Understanding the crystallization of solution processed alloys of hybrid perovskites by multimodal characterization
  Neville Smith prize talk at ALS User Meeting, ALS Berkeley Lab, 1 – 3 Oct 2019

- S. Pratap, N. Tamura, C. Stan, Z. Yuan, H. Gowdey, A. MacDowell, T. Song, N. Barchi, P. Muller-Buschbaum, C. Sutter-Fella, J. Slack
  Understanding the crystallization of solution processed alloys of hybrid perovskites by multimodal characterization
  ALS User Meeting, ALS Berkeley Lab, 1 – 3 Oct 2019

- W. Chen, S. Grott, S. Pratap
  Small angle X-ray and neutron scattering
  Polymer Physics Summer School Obertauern, Austria, 12 – 15 Jun 2018

- S. Pratap, J. Schlipf, P. Muller-Buschbaum
  On the chemical origins of crystalline preferred orientations in hybrid perovskite thin films
  DPG-Fruhjahrstagung, Dresden, 19 – 24 Mar 2017

- S. Pratap, J. Schlipf, P. Muller-Buschbaum
  Microstructural evolution during thin film growth
  3rd Internal Biennial Science Meeting of the MLZ, Grainau, 19 – 27 Jun 2017

- S. Pratap, J. Schlipf, P. Muller-Buschbaum
  Perovskite: The new crystalline sheriff in the photovoltaic county
  7th Colloquium of the Munich School of Engineering, Garching, 13 Jul 2017

- S. Pratap
  Lessons learnt from nanofocussed x-ray beamtime : An experimental saga
  Seminar talk at the chair of functional materials, Physics Department, TU Munich, 19 Jul 2017

- S. Pratap, J. Schlipf, P. Muller-Buschbaum
  On the chemical origins of crystalline preferred orientations in hybrid perovskite thin films
  NIM Summer Retreat, Schloss Hirschberg, Beilngries, 31 Jul – 2 Aug 2017

Conference poster presentations

- S. Pratap
  Hierarchical Structures in Hybrid Perovskite Thin Films: Implications for Photovoltaics
  MLZ User Meeting 2020, 08 – 09 December 2020

- S. Pratap, N. Tamura, C. Stan, Z. Yuan, H. Gowdey, A. MacDowell, T. Song, N. Barchi, P. Müller-Buschbaum, C. Sutter-Fella, J. Slack
  Probing the in-situ dynamics of structure-property evolution in hybrid perovskite thin films spincoated from complex fluids by a custom designed, beamline compatible multimodal measurement chamber
  40th International Conference on Vacuum Ultraviolet and X-ray Physics, San Francisco, 1 – 5 Jul 2019

- S. Pratap, P. Muller-Buschbaum
  Complex morphologies and pattern formation in perovskite thin films
  NIM Summer Retreat, Spitzingsee, 13 – 15 Aug 2018

- S. Pratap, P. Muller-Buschbaum
  Microstructural evolution during thin film growth
  NIM Conference: The Future of Nanoscience, Tutzing, 4 – 6 Sep 2018

- S. Pratap, J. Schlipf, K. John, V. Korstgens, F. Fischer, S. Vema, A. Davydok, C. Krywka, ¨ P. Muller-Buschbaum
  An insight into atmospheric degradation processes by mapping local nanoheterogeneities within hybrid polycrystalline perovskite films
  4th German SNI Conference, Garching, 17 – 19 Sep 2018

- S. Pratap, E. Keller, P. Muller-Buschbaum
  On the colloidal behaviour of hybrid perovskite precursor solutions: insights into the nano and mesoscale
  20th CeNS Workshop: Celebrating Nanoscience, Venice, 24 – 28 Sep 2018

- S. Pratap, J. Schlipf, P. Muller-Buschbaum
  On the chemical origins of crystalline preferred orientations in hybrid lead halide perovskite thin films
  ALS Annual User Meeting, Lawrence Berkeley National Laboratory, California, 2 – 4 Oct 2018 .

- S. Pratap, J. Schlipf, P. Muller-Buschbaum
  On the chemical origins of crystalline preferred orientations in hybrid organometallic lead halide perovskite thin films
  Nanostructured Functional Materials for Sustainable Energy Provision, Literaruhaus, Munich, 26 – 28 Jul 2017.

- S. Pratap, J. Schlipf, P. Muller-Buschbaum
  On the chemical origins of crystalline preferred orientations in hybrid organometallic lead halide perovskite thin films
  6th SolTech Conference: Solar Technologies go Hybrid, Munich, 4 – 5 Oct 2017.

- S. Pratap, J. Schlipf, P. Muller-Buschbaum
  On the colloidal behavior of hybrid inorganic-organic lead halide perovskite precursor solutions and its impact on thin film microstructure
  Kolloid-Tagung "Multiresponsive systems", Garching, 9 – 11 Oct 2017.

Acknowledgments

I would like to thank Peter Müller-Buschbaum for giving me the opportunity to pursue this project. I appreciate the guidance and supervision along every step of the PhD and for his reassurance in my capabilities and for the many opportunities to pursue projects of my choice.

My time at E13 was made memorable thanks to all the people who helped create an enjoyable work environment, and with whom I shared over four years of companionship. My thanks go to Lucas Kreuzer, Tobi Widmann, Sebastian Grott-the worst(s) with whom I started my PhD and who have been constant pillars of joyous support. I can't keep track of the number of jokes we all made at each other, and all the times you all helped me every time I was in trouble, and I can't believe we haven't played a single game of GoT in all these years. The best office-mates Juju Heger, Xinyu Jiang and Shanshan Yin for the loving atmosphere in our office and for being so supportive and adjusting with our use of the office space during corona times. To the girl gang Christina Geiger, Anna-Lena Oechsle, Kerstin Wienhold, Franziska Löhrer, Julija Reitenbach for the support, solidarity, and fun and for making birthdays and events extra special with their thoughtful gifts. I would like to thank Nuri Hohn, Nitin Saxena, Johannes Schlipf, Lorenz Bießmann together with whom I attended many conferences, conference dinners and who recounted many stories of the chair which strengthened my sense of belonging to the group. Gilly Möhl, Simon Schaper, Wei Chen, Christian Weindl, Lennart Reb, Manuel Scheel, Renjun Guo, Nian Li, Marc Gensch, Lukas Spanier, Dominik Schwaiger, Wei Cao, Dan Yang and Roy Schaffrina for brightening up the chair with their presence. Special thanks go to Volker Körstgens for being a patient advisor to many strange queries and for his support and company during beamtimes in Hamburg. Moreover, Christine Papadakis was always a welcoming and helpful advisor on many topics, especially in Polymer Physics. The Polymer Music Band- Jenny Lebert, Chia-Hsin Ko, Juju Heger, Nitin Saxena, Johannes Schlipf, Lucas Kreuzer, Christina Geiger, Wei Chen, Gilly Möhl for the awesome rehearsals, practices and concerts. The open air concert from atop the mountains will always be remembered.

I would like to thank my students Felix Fischer, Wolfgang Männer, Elizabeth Keller and Sundeep Vema for working together on projects and together with whom I learned about varying coding environments like CodeBlocks and Anaconda.

Moreover, thanks are extended to the Soft Matter group- Bart-Jan Niebuur, Florian Jung, Chia-Hsin Ko, Jia-Jhen Kang for their friendly presence, great presentations and for support in DLS measurements.

Marion Waletzki and Carola Kappauf were always kind and supportive with all kinds of administrative dealing.

I'd like to thank the NIM student board, Anna Katharina Hatz, Magnus Bauer, Lukas Schnitzler, Tobias Petzak, and to the older NIM colleagues Hongi Hu, Andrej Kamenac for their company in great meetings, conferences, summer retreats. Moreover, thanks go to Peter Sonntag, Chris Hohmann and Silke Mayerl-Kink for maintaining the NIM environment.

Special thanks go to Nobumichi Tamura and Carolin Sutter-Fella for acting as my advisors during my fellowship year at the ALS and beyond. Finn Babbe, Nicola Barchi, Harvey Yuan, Tina Luong, Zach Haber, TB Song for making the in situ beamtimes with the spin coater so thrilling and fun. Thanks also go to Yali and Tobi Kistler, Andrew Shum, Asritha Nallapaneni, Ane Etxebarria, Aleks Kiessling, Fabrice Roncoroni, Viki Bera for their company and support in Berkeley. I cannot express enough gratitude to Jonathan Slack, Monica, Zohe and Michelle for all their support, love and care. Jonathan especially for going above and beyond to make the spin coater project a reality and being ever so prompt in support for all my ideas, plans, applications and recommendations.

I'd like to thank Priyanka Das Rajkakati, Apoorva Srivastava, Tania Das, Sudarshan Shinde, Devika Kandpal, Abhishek Singh, Abheek Mehta for their friendship and for always cheering me up when I was feeling down. My most special thanks are reserved for my family, to my Dad, Mom and Shashwat for being my strongest pillars of love and support and to Akshath Sharma for bearing with me through the hardest of times and for always having my back.